

# Anisotropic Azimuthal Power and Temperature distribution on FuelRod: Impact on Hydride Distribution

---

## Fuel Cycle

Dr. Arthur Motta

Pennsylvania State University

In collaboration with:

Idaho National Laboratory

JC de la Garza, Federal POC  
Brady Hanson, Technical POC

## **Final Report – October 2014**

### **Anisotropic Azimuthal Power and Temperature distribution on FuelRod: Impact on Hydride Distribution**

DOE-NEUP 11-2987

#### **Principal Investigator**

Arthur Motta  
*The Pennsylvania State University*

#### **Collaborators**

Kostadin Ivanov  
*The Pennsylvania State University*

Maria Avramova  
*The Pennsylvania State University*

Jason Hales  
*Idaho national Laboratory*

#### **Duration**

September 2011 – September 2014

#### **Total Funding Level**

\$ 631,500

#### **TPOC**

Brady Hanson

## Abstract

The degradation of the zirconium cladding may limit nuclear fuel performance. In the high temperature environment of a reactor, the zirconium in the cladding corrodes, releasing hydrogen in the process. Some of this hydrogen is absorbed by the cladding in a highly inhomogeneous manner. The distribution of the absorbed hydrogen is extremely sensitive to temperature and stress concentration gradients. The absorbed hydrogen tends to concentrate near lower temperatures. This hydrogen absorption and hydride formation can cause cladding failure. This project set out to improve the hydrogen distribution prediction capabilities of the BISON fuel performance code. The project was split into two primary sections, first was the use of a high fidelity multi-physics coupling to accurately predict temperature gradients as a function of  $r$ ,  $\theta$ , and  $z$ , and the second was to use experimental data to create an analytical hydrogen precipitation model.

The Penn State version of thermal hydraulics code COBRA-TF (CTF) was successfully coupled to the DeCART neutronics code. This coupled system was verified by testing and validated by comparison to FRAPCON data. The hydrogen diffusion and precipitation experiments successfully calculated the heat of transport and precipitation rate constant values to be used within the hydrogen model in BISON. These values can only be determined experimentally. These values were successfully implemented in precipitation, diffusion and dissolution kernels that were implemented in the BISON code. The coupled output was fed into BISON models and the hydrogen and hydride distributions behaved as expected. Simulations were conducted in the radial, axial and azimuthal directions to showcase the full capabilities of the hydrogen model.

## Table of Contents

Abstract .....	2
A. Introduction .....	10
B. BISON Authentication .....	10
B.1. Standalone BISON and FRAPCON Comparison .....	10
B.2. BISON Modeling Capabilities .....	15
C. Multiphysics Coupling Summary .....	17
C.1. Coupling Strategy .....	17
C.2. CTF-DeCART Coupling .....	17
C.3. BISON Coupling .....	19
C.4. Benchmarking .....	21
C.4.1 4x4 Fuel Rod Sub-Assembly .....	21
C.4.2 DeCART-CTF 4x4 Sub-Assembly with Guide Tube .....	31
C.4.3 CTF-DeCART Comparison with Frapcon Integral Assessment Case .....	43
D. Hydrogen Background .....	46
D.1. Hydrogen Diffusion .....	47
D.2. Hydrogen as hydrides .....	49
D.3. Kinetics of precipitation .....	49
D.4. Hydrogen Model in Bison .....	51
D.5. Implementation of the model in the 3D fuel performance code BISON .....	53
E. Hydrogen Experiment .....	54
E.1. Measurement of the heat of transport $Q^*$ .....	54
E.1.1 Experimental design for measurement of $Q^*$ .....	57
E.1.2 Experimental procedure .....	60
E.1.3 Results of the heat of transport experiment .....	64
E.1.4 Conclusion of the results of the $Q^*$ measurement .....	66
E.2. Measurement of the rate of precipitation .....	68
E.2.1 Experimental technique .....	68
E.2.2 Experimental procedures .....	69
F. Combined Results .....	75
F.1. Results of 5-pellet rod simulation using BISON .....	75
F.1.1 Geometry and boundary conditions .....	75
F.1.2 Hydrogen distribution in hot 5 pellets rod .....	78
F.1.3 Hydrogen distribution in a cold 5 pellets rod .....	81
F.2. Full rod results with BISON .....	83
F.3. 4x4 Sub-Assembly with Water Rod Combined Results .....	86



	4
F.4. 4x4 with control rod (increased power) results (including BISON).....	90
F.5. Spalled Oxide.....	93
G. Conclusions .....	96
H. Publications .....	97
I. References .....	98

## List of Figures

Figure B.1: BISON versus Frapcon Average Fuel Temperature [2].....	14
Figure B.2: Total Average Cladding Temperature Over 4.2 Years As Calculated By Frapcon and BISON for the Oconee Benchmark Case 15309. [2] .....	14
Figure B.3: Rod Average Burnup Comparison Between Frapcon and BISON for OCONEE Rod 15309 [2] .....	15
Figure B.4 Temperature Distribution Before Contact (Left) and After Contact (Right). [2] ..	16
Figure B.5: ParaView Visualization of Rod 15309 Mesh Temperatures [2] .....	16
Figure B.6: ParaView Visualization of Example INL BISON Model with Chamfered Fuel Pellets [4] .....	17
Figure C.1: External Coupling Diagram Between CTF, DeCART, and BISON [6] .....	19
Figure C.2: Code Coupling Python Script Operating Procedure [6].....	20
Figure C.3: Rod and sub-channel nomenclature used in CTF's format [6] .....	22
Figure C.4: DeCART Noding Breakdown for 4x4 fuel pin sub-assembly [6] .....	22
Figure C.5: CTF Crossflow Diagram for 4x4 Sub-Assembly [6] .....	23
Figure C.6: CTF Gap Connection Diagram for 4x4 Sub-Assembly [6] .....	23
Figure C.7: Convergence of the fuel temperature at 0.0 MWd/kgU [6] .....	25
Figure C.8: Rod 7 convergence of the moderator temperature at 0.0 MWd/kgU [6] .....	26
Figure C.9: Rod 7 Convergence of the Moderator Density at 0.0 MWd/kgU [6] .....	26
Figure C.10: Rod 7 Converged Axial Power Distributions [6].....	27
Figure C.11: Rod 7 Average Fuel Temperatures [6].....	27
Figure C.12: Rod 7 Converged Moderator Temperature Profiles [6].....	28
Figure C.13: Rod 7 Converged Moderator Density Profiles [6] .....	28

Figure C.14: Comparison of CTF-DeCART vs DeCART Standalone Axial Power Distribution for Rod 7 at 0.0 MWd/kgU [6] .....	29
Figure C.15: Comparison of Coupled CTF-DeCART to the Standalone DeCART Axial Power Distribution for rod 7 at 10.0 MWd/kgU.[6].....	29
Figure C.16: Comparison of Coupled CTF-DeCART to the Standalone DeCART Axial Power Distribution for rod 7 at 20.0 MWd/kgU.[6].....	30
Figure C.17: Comparison of Coupled CTF-DeCART to the Standalone DeCART Axial Power Distribution for rod 7 at 27.5 MWd/kgU. [6].....	30
Figure C.18: ORNL AMPFuel Full 17x17 Assembly [6] .....	31
Figure C.19: 4x4 Sub-Assembly Selected from ORNL AMPFuel Full 17x17 Assembly Model [6]	32
Figure C.20: Radial Power Factors at BOC, MOC, and EOC for “Internal” Array [6].....	33
Figure C.21: Rod 2 Convergence of the Fuel Centerline Temperature at 0.0 MWd/kgU for “Internal” [6] .....	35
Figure C.22: Rod 2 Convergence of the Fuel Surface Temperature at 0.0 MWd/kgU for “Internal” [6] .....	35
Figure C.23: Rod 2 Convergence of the Moderator Temperature at 0.0 MWd/kgU for “Internal” [6] .....	36
Figure C.24: Rod 2 Convergence of the Moderator Density at 0.0 MWd/kgU for “Internal” [6] .....	36
Figure C.25: Rod 2 Axial Power Shapes as a Function of Burnup for “Internal” [6].....	37
Figure C.26: Rod 2 and Rod 16 Converged Fuel Centerline Temperature Distributions for “Internal” [6] .....	38
Figure C.27: Rod 2 and Rod 16 Converged Fuel Surface Temperature Distributions for “Internal” [6] .....	39
Figure C.28: Rod 2 and Rod 16 Converged Moderator Temperature Distributions for “Internal” [6] .....	40
Figure C.29: Rod 2 and Rod 16 Converged Moderator Density Distributions for “Internal” [6] .....	41
Figure C.30: Rod 2 Clad Outer Surface Temperature Distributions for “Internal” [6] .....	42
Figure C.31: Subchannel 7 and 19 Liquid Temperature Distributions for “Internal” [6] .....	42
Figure C.32: FRAPCON Axial Power shapes [6].....	43
Figure C.33: Rod 15309 Axial Power Shapes from the CTF-DeCART Coupling [6] .....	43
Figure C.34: CTF-DeCART vs Actual Axial Power Shape (0-295 days) [6].....	44

Figure C.35: CTF-DeCART vs Actual Axial Power Shape (295-600 days) [6].....	44
Figure C.36: CTF-DeCART vs Actual Axial Power Shape (600-850 days) [6].....	45
Figure C.37: CTF-DeCART vs Actual Axial Power Shape (850-1150 days) [6].....	45
Figure C.38: CTF-DeCART vs Actual Axial Power Shape (1150-1550 days) [6].....	46
Figure D.1 Radial hydrogen distribution and hydride rim (740-wppm H) [14] .....	48
Figure D.2 Hydrogen boundary condition schematic .....	50
Figure E.1 Measurement of $Q^*$ with respect to the temperature .....	56
Figure E.2: Heat of transport measured by Kammenzind.....	56
Figure E.3: 3-D View of the 304 Stainless Steel holders and the Zircaloy-4 plate sample ....	57
Figure E.4: Heaters, holders and sample in the heat of transport experiment.....	58
Figure E.5: Schematic of the temperature control for the diffusion experiment.....	59
Figure E.8: Design of the insulation of the experiment .....	60
Figure E.9: Thermocouples on the sample.....	60
Figure E.10: Temperature and hydrogen steady state profile under 650°-550° gradient.....	61
Figure E.11: Hydrogen profile before starting 660°C-560°C gradient experiment.....	62
Figure E.12: Kinetics of the concentration profile (one line per 10 hours) with a 650°-550°C gradient.....	62
Figure E.13: Difference with steady state (one line per 10 hours) with a 650°-550°C gradient	63
Figure E.14: Sample after 560°C-660°C experiment.....	64
Figure E.15: Temperature profile for diffusion experiment.....	65
Figure E.16: Result of the diffusion experiment.....	66
Figure E.17: Comparison of experimental results with Kammenzind's data [20].....	67
Figure E.18: Heat of transport $Q^*$ measured in the literature as a function of the temperature gradient.....	67
Figure E.19: Schematic representation of beamline 1-ID experimental set-up. ....	70
Figure E.20: Picture of the experimental set-up at beamline 1-ID.....	70
Figure E.21: Data Analysis procedure for X-Ray diffraction data collected at beamline 1-ID.	71

Figure E.22: Evolution of temperature and hydrides concentration during synchrotron experiment sample containing 541 wt ppm H.....	72
Figure E.23: Measured precipitation parameter $\alpha^2$ with respect to T, with different initial concentration (434, 541 and 603 wt. ppm).....	74
Figure F.1: Five pellet geometry for BISON simulation .....	77
Figure F.2: Axial temperature profile for the hot 5 pellets mesh at the outer edge of the cladding, after 4 years .....	78
Figure F.3: Radial temperature profile for the hot 5 pellets mesh at z=2.75 cm, after 4 years	79
Figure F.4: Evolution of the cladding temperature for the hot 5 pellets at z=3.0 cm and r=4.15mm and 4.2mm (in green, inner edge), and r=4.67mm and 4.72mm (blue, outer radius), between 0 years and 4 years .....	79
Figure F.5: Axial hydrogen profile for the hot 5 pellet mesh at the outer edge of the cladding, after 4 years .....	80
Figure F.6: Radial hydrogen profile for the hot 5 pellets mesh at z=2cm, after 4 years.....	80
Figure F.7: Axial temperature profile for the 5 pellets mesh at the coldest spot of the fuel at the outer edge of the cladding, after 4 years .....	81
Figure F.8: Radial temperature profile for the hot 5 pellets mesh at z=3cm, after 4 years.....	82
Figure F.9: Radial hydrogen profile for the cold 5 pellets mesh at z=, after 4 years.....	83
Figure F.10: Radial hydride profile for the cold 5 pellets mesh at z=, after 4 years.....	83
Figure F.11: Hydrogen profile in a 360-pellets fuel cladding after 1 hour, with an initial homogeneous concentration of 60 wt.ppm.....	84
Figure F.12: Hydrogen profile in a 360-pellets fuel cladding after 1 day, with an initial homogeneous concentration of 60 wt.ppm.....	85
Figure F.13: Evolution of the difference average concentration between high (z=3m) and low (z=1m) elevations. ....	85
Figure F.14: 4x4 Sub-Assembly with Guide Tube layout at 0 MWd/kgU Burnup .....	87
Figure F.15: Azimuthal Outer Cladding Temperature Distributions for CTF plane 38 at 0 MWd/kgU.....	87
Figure F.16: Rod 11 1.85 m height BISON output at 3.43E7 seconds Top Left: Cladding temperature distribution Top Right: Cladding Hydrogen Distribution Bottom left: Cladding Hydride Distribution Bottom Right: Fuel Temperature .....	88
Figure F.17: Rod 11 axial height 1.85-1.90 m end of simulation BISON Cladding Temperature Distribution.....	90

Figure F.18: 4x4 Sub-Assembly with Control Rod layout at 0 MWd/kgU Burnup .....	91
Figure F.19: Rod 11 1.85 m height BISON output with control rod in assembly at 11E6 seconds Top Left: Cladding temperature distribution Top Right: Cladding Hydrogen Distribution Bottom left: Cladding Hydride Distribution Bottom Right: Fuel Temperature .....	92
Figure F.20: Rod 11 axial height 1.85-1.90 m end of simulation BISON Cladding Temperature Distribution Control Rod Case .....	93
Figure F.21: Top Left (a): Hydrogen as hydride distribution after 2.5 years, top right (b): fuel pellet temperature distribution,.....	95
Figure F.22: Cladding temperature distribution for the spalled oxide event. ....	96

### List of Tables

Table B.1: FRAPCON Rod 15309 Parameters .....	11
Table B.2: Frapcon Power History data for rod 15309 .....	12
Table B.3: FRAPCON Rod 15309 Axial Power Shape History .....	13
Table B.4: BISON Default Parameters .....	13
Table C.1: Specifications for DeCART-CTF Coupled 4x4 Test Simulation.....	21
Table C.2: Input Parameters for CTF for 4x4 Sub-Assembly [6] .....	24
Table C.3: Input Parameters for DeCART for 4x4 Sub-Assembly [6] .....	24
Table C.4: Convergence Parameters for CTF-DeCART 4x4 Fuel Pin Sub-Assembly [6] .....	25
Table C.5: Convergence of CTF-DeCART Coupled Calculations at 0.0 MWd/kgU for “Internal” [6] .....	34
Table D.1: Hydrogen model constants .....	53
Table E.1 Summary of heat of transport of hydrogen in Zircaloy measurements .....	55
Table E.2: Temperature controller Specifications .....	58
Table E.3: PID values of the thermal controllers .....	59
Table E.4: Estimators of the difference between transient and steady state profile (650°C-550°C) .....	63
Table E.5: Temperature in the plate during the diffusion experiment .....	64
Table E.6: Overall hydrogen concentration in the APS samples .....	71
Table E.7 Summary of $\alpha^2$ measurements .....	74

Table F.1: Pellet geometry in the PWR simulations .....	76
Table F.2: Condition for five pellet DeCART-CTF coupling.....	76
Table F.3: Parameter input for 4x4 Sub-Assembly with Guide Tube and Varying Enrichments	86

## A. Introduction

The extreme environment in which nuclear fuel operates requires improved fuel analysis. The fuel simulation code BISON has been developed at Idaho National Laboratory (INL) to address this need. Of high importance in fuel performance is the degradation of the zirconium cladding. In the high temperature environment of a reactor, the zirconium in the cladding tends to corrode, and in the process hydrogen is released. Some of this hydrogen is absorbed by the cladding in a highly inhomogeneous manner. The distribution of the absorbed hydrogen is extremely sensitive to temperature concentrations. The absorbed hydrogen tends to concentrate near lower temperatures. This hydrogen absorption and hydride formation can cause cladding failure. This project is designed to improve the hydrogen distribution prediction capabilities of the BISON code. The project was split into two primary sections, first was the use of a high fidelity multi-physics coupling to accurately predict temperature gradients as a function of  $r$ ,  $\theta$ , and  $z$ , and the second was to use experimental data to create an analytical hydrogen precipitation model to be implemented in BISON.

In order to achieve this, multiple computer codes were employed, including a neutronics code, a thermal hydraulics code, a fuel performance code and associated modeling programs. The primary purpose of the project was to enhance the hydrogen modeling capabilities of the INL fuel performance code BISON. BISON is a three-dimensional finite element based fuel performance code that can model temperatures, fission product swelling, densification, thermal and irradiation creep, fracture, and fission gas production [1]. In order to achieve high accuracy temperature and power distributions for BISON input, the improved Penn State version of thermal hydraulics code Coolant Boiling in Rod Arrays – Two Fluid (COBRA-TF) – CTF was coupled to the neutronics code Deterministic Core Analysis based on Ray Tracing (DeCART). The associated programs CUBIT and TRELIS were used to generate the three dimensional models and meshes required as additional input for BISON. For viewing BISON output and generating graphics, PARAVIEW was employed.

## B. BISON Authentication

### B.1. Standalone BISON and FRAPCON Comparison

BISON is a relatively new fuel performance code, which is still under development at INL. A commercial version called PEREGRINE is being developed in parallel. Efforts at INL for validation and verification are underway to compare BISON to experimental data and other fuel performance codes. For this project, BISON results were compared to the NRC approved FRAPCON code to determine its accuracy. A full report of this comparison can be found in [2]. A single fuel rod was chosen from the FRAPCON Integral Assessment document to be modeled in BISON. The rod chosen was from the Oconee Nuclear Station in South Carolina (Oconee Benchmark case 15309) [3]. This nuclear station is a commercial PWR plant, and the rod used uranium oxide fuel covered with Zircaloy-4 cladding. This particular case was chosen because the rod was in the core for about 4.2 years, which ensured fuel pellet contact with the cladding [3].

Table B.1: FRAPCON Rod 15309 Parameters

<b>Input</b>	<b>Value</b>	<b>Units</b>
Fuel	UO <sub>2</sub>	
Enrichment	3.00	
Fuel Density	10.412	g/cm <sup>3</sup>
Percent Theoretical Density	95	Percent
Burnable Poison	None	
Cladding Type	Zircaloy-4	
Cladding Density	6.55	g/cm <sup>3</sup>
Coolant	H <sub>2</sub> O	
Fill Gas	Helium	
Fuel Pellet radius	4.66E-3	m
Clad Inner Radius	4.79E-3	m
Clad Outer Radius	5.45E-3	m
Clad Thickness	6.73E-4	m
Pin Pitch	1.4224E-2	m
Active Fuel Height	3.58	m
Core Pressure	15.17	MPa
Mass Flow Rate	0.3844	Kg/s
Inlet Temperature	290.7	°C
Pellet Height	1.74E-2	m
Number of Pellets	201	
Pellet Dish Height	3.56E-4	m
Pellet end dish shoulder width	1.27E-3	m
Fuel Surface Roughness	5.99E-7	m
Clad surface roughness	5.00E-7	m
Initial Fill gas pressure	3.31	MPa
Plenum to fuel ratio	0.076	
Fuel to dish volume ratio	0.9894	



Table B.2: Frapcon Power History data for rod 15309

<b>Time (days)</b>	<b>Linear Heat Rate (kW/m)</b>
0.1	19.03
65	19.03
125	25.92
185	24.61
210	23.95
235	22.31
295	21.65
325	25.92
350	24.93
360	24.28
370	22.64
500	21.65
510	20.01
535	21.98
540	19.69
560	21.65
600	20.01
615	13.45
850	17.72
890	16.73
905	15.42
920	17.72
1130	16.4
1150	14.76
1160	14.11
1205	14.44
1220	14.11
1240	14.44
1400	14.76
1445	14.93
1490	15.09
1510	15.26
1535	15.42
1550	11.81

Table B.3: FRAPCON Rod 15309 Axial Power Shape History

Axial Location (m)	Relative Power and Various Times				
	0-295 days	295-600 days	600-850 days	850-1150 days	1150-1550 days
0	0.2	0.2	0.2	0.2	0.45
0.3048	1	1.08	0.82	0.95	0.94
0.6096	1.2	1.18	1.02	1.05	1.02
0.9144	1.25	1.12	1.11	1.03	1.05
1.2192	1.25	1.04	1.13	1.03	1.07
1.524	1.22	0.97	1.08	1.08	1.1
1.8288	1.2	0.97	1.04	1.12	1.12
2.1336	1.16	1	1.05	1.12	1.11
2.4384	1.14	1.03	1.14	1.1	1.1
2.7432	1.06	1.05	1.19	1.05	1.06
3.048	0.78	1.1	1.13	1	1.02
3.3528	0.3	0.97	0.9	0.81	0.95
3.5814	0.15	0.2	0.2	0.4	0.5

Table B.4: BISON Default Parameters

Parameter	Value	Units
Energy per fission	3.20E-11	J/fission
Young's Modulus		
UO2	2.00E11	Pa
Zircaloy-4	7.50E10	Pa
Poisson's ratio:		
UO2	0.345	
Zircaloy-4	0.3	
Thermal Expansion Coefficient		
UO2	1.00E-5	K <sup>-1</sup>
Zircaloy-4	5.00E-6	K <sup>-1</sup>
UO2 Grain Radius	1.00E-5	m
Clad Thermal Conductivity	16	W/mK
Clad Specific Heat	330	kJ/kgK

Tables Table B.1-Table B.4 show the input used to create the BISON geometric mesh file and the problem specification input deck. After executing this input with the BISON code, the output was compared to the FRAPCON Data. Figure B.1 through Figure B.3 show the results of this comparison through average fuel temperature, average cladding temperature, and Rod average Burnup.

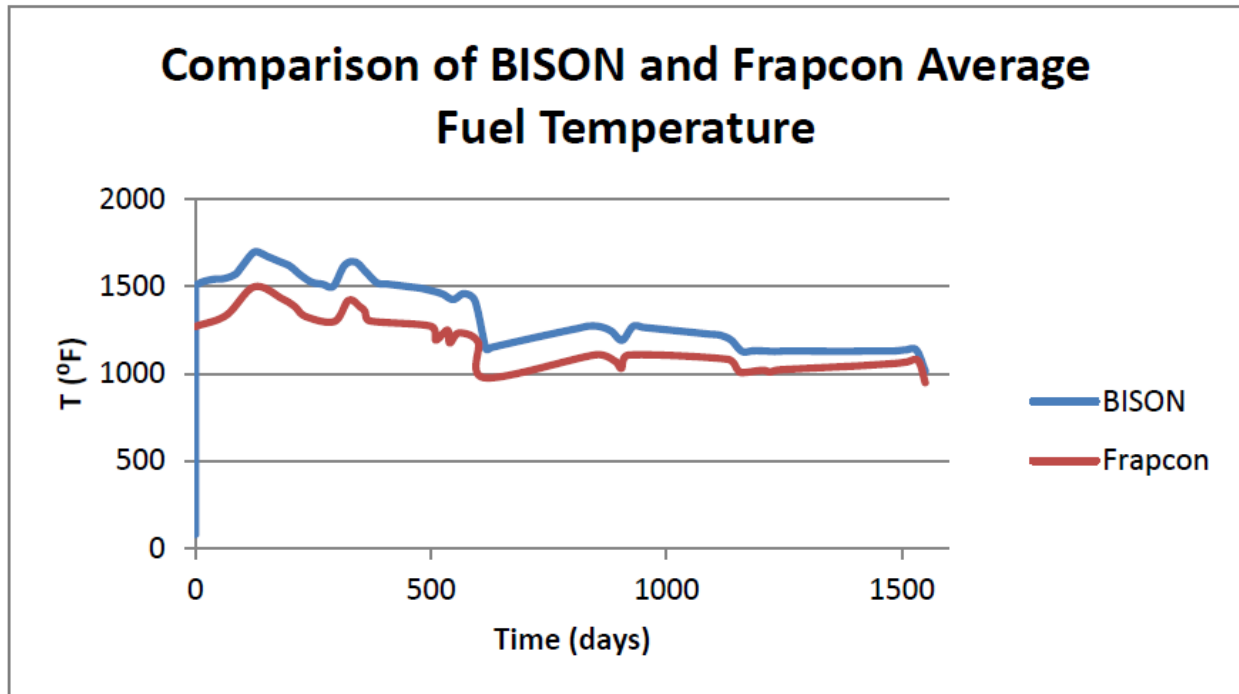


Figure B.1: BISON versus Frapcon Average Fuel Temperature [2]

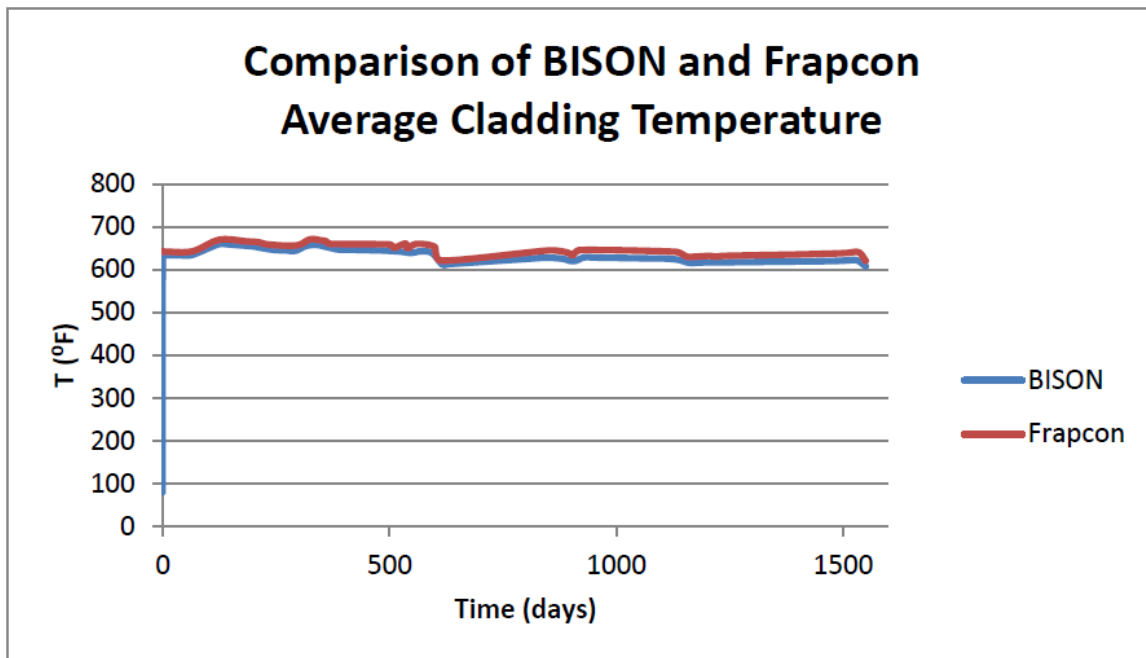


Figure B.2: Total Average Cladding Temperature Over 4.2 Years As Calculated By Frapcon and BISON for the Oconee Benchmark Case 15309. [2]

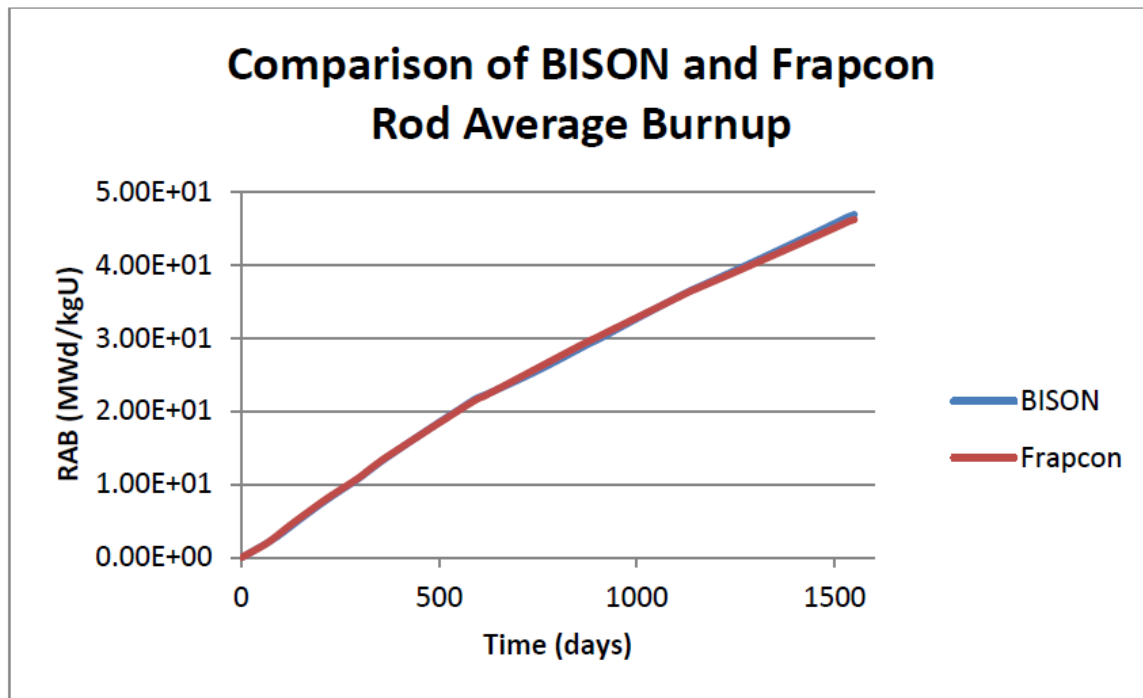


Figure B.3: Rod Average Burnup Comparison Between Frapcon and BISON for OCONEE Rod 15309 [2]

As can be seen in Figure B.1 through Figure B.3, there is reasonable agreement between the two codes. BISON predicts higher average fuel temperatures throughout the life of the rod, however, it predicts slightly lower average cladding temperatures. Overall BISON seems the more conservative of the two codes.

## B.2. BISON Modeling Capabilities

At the beginning of the project, additional figures were created to visualize the temperature gradients seen at inter-pellet gap locations in a BISON fuel rod simulation. Figure B.4 gives an example of the visualization capabilities that can be achieved via the high resolution BISON output. Using a visualization tool, such as Paraview, multiple variables can be viewed in real time as the model progresses through the power history. It is helpful to watch the evolution of the fuel and clad temperatures during the power history and as contact occurs between the fuel pellet and inner clad surface. Figure B.5 shows a section of the mesh temperatures calculated within BISON of the inter-pellet region of rod 15309. Figure B.5: ParaView Visualization of Rod 15309 Mesh Temperatures [2] shows that the temperature is slightly lower in the region near the inter-pellet gap.

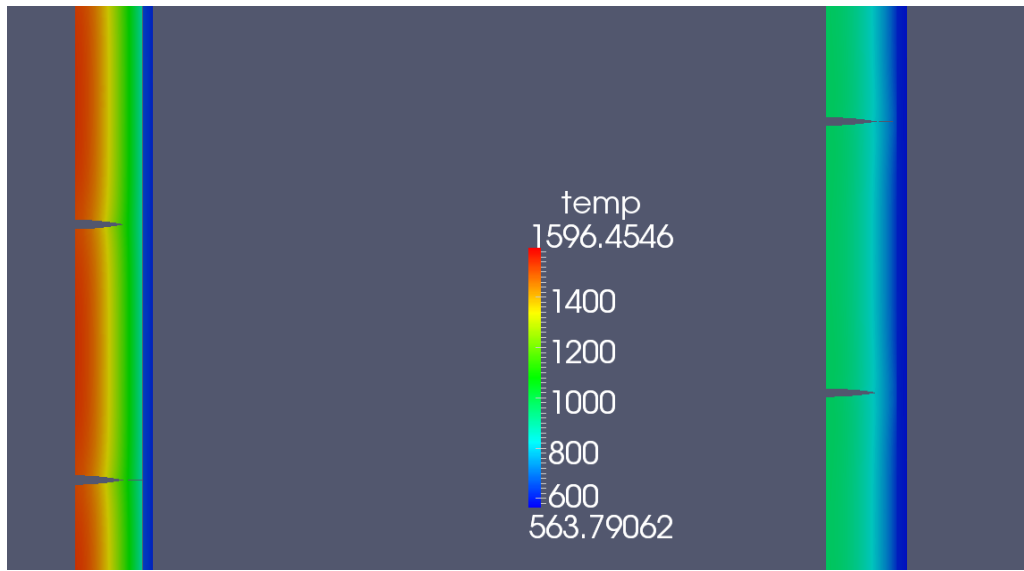


Figure B.4 Temperature Distribution Before Contact (Left) and After Contact (Right). [2]

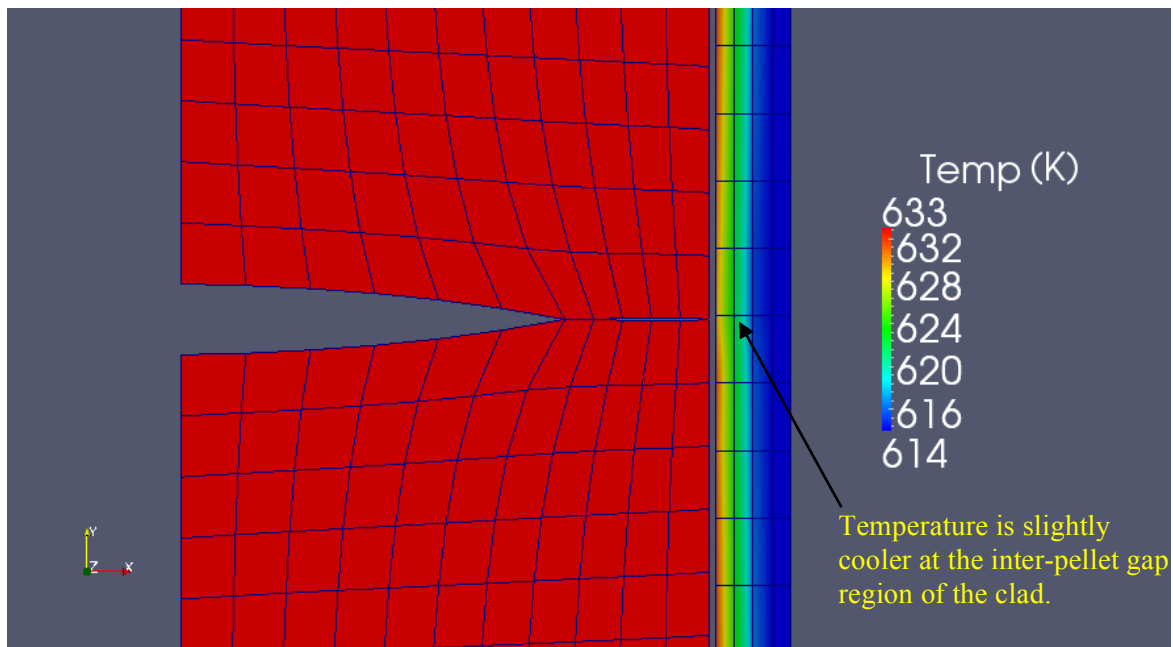


Figure B.5: ParaView Visualization of Rod 15309 Mesh Temperatures [2]

An INL example model of a chamfered  $\text{UO}_2$  fuel pellet with a fine mesh was run to examine the capabilities of the code to create accurate temperature distributions. The output is shown in Figure B.6 [4]. Fuel pellets with chamfered geometry will cause a different inter-pellet gap, which may lead to a much cooler region of clad near the area. Hydrogen redistributes and concentrates in the cooler regions of the fuel rod clad. This cooler region of clad in Figure B.6 may have a higher risk of failure at lower stresses, temperatures and pressures. BISON has the capability to calculate these small regions of lower

temperature, which is important for the success of this project's objective: prediction of hydrogen distribution and hydride modeling.

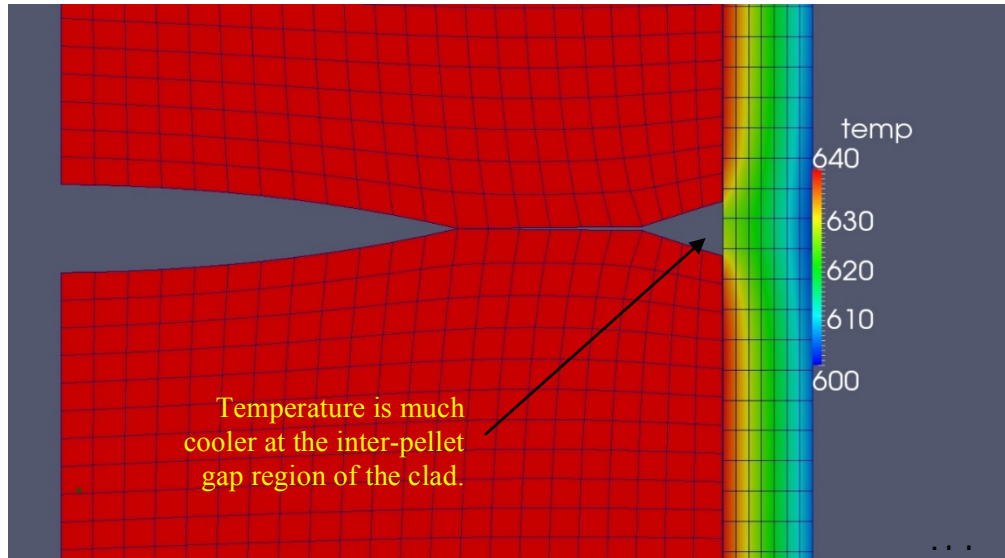


Figure B.6: ParaView Visualization of Example INL BISON Model with Chamfered Fuel Pellets [4]

## C. Multiphysics Coupling Summary

### C.1. Coupling Strategy

To obtain the hydrogen distribution accurately, it was necessary to calculate the three-dimensional temperature distribution in the cladding with a very fine resolution. To obtain such a distribution, it was decided to create a high fidelity multi-physics coupling. The coupling employed was a combination of DeCART and COBRA-TF (CTF). DeCART (Deterministic Core Analysis based on Ray Tracing) is a whole core neutron transport code for pressurized water reactors (PWRs) and boiling water reactors (BWRs). DeCART solves the neutron transport equation using the Method of Characteristics approach with discrete ray tracing [5]. Due to the computational expense of this technique, the code uses the Method of Characteristics for the two-dimensional planar ( $r$ ,  $\theta$ ) directions and a one-dimensional diffusion solution for the axial solution. CTF (Coolant Boiling in Rod Arrays-Two Fluid) is the Penn State maintained multi-dimensional subchannel thermal hydraulics code.

### C.2. CTF-DeCART Coupling

The codes were externally coupled using an independent Python script that executes the DeCART and CTF codes with predefined user input. The script runs the codes one after the other in series while passing information between the codes until convergence of specified parameters is met. This portion of the project was executed by Ian Davis for his nuclear engineering Masters of Science thesis and a detailed report can be found in [6].

The script passes local power information from the DeCART output to the CTF input. This information includes relative axial power distribution, relative radial power distribution, and radial power factor (the

total relative power of one rod compared to the average power of the array). The coupling between DeCART and CTF is one to one, however, it should be noted that CTF has no means of azimuthally splitting cells. The azimuthal dependence of fluid temperature is based on the selection of subchannels attached to the rod.

For this coupling, input files were first created for both DeCART and CTF based on fuel specifications and general parameters to describe the geometry and provide nominal starting values. The coupling begins by running DeCART and the first iteration uses nominal values for fuel, clad, and moderator temperatures and densities. Power densities are stored by DeCART at each mesh cell and burnup step. This output is converted into the CTF input in the form of relative axial power distribution, relative radial power distribution, and radial power factor. This information is weighted based on the associated volume in each cell. This allows the normalized power distribution to be calculated for the CTF input. The power density from DeCART is stored as  $P''_{i,j,k}$  where  $i$  is rod number,  $j$  is the flat source plane number, and  $k$  is the axial cell number. The power in each cell can be calculated by multiplying each power density by its associated cell volume:

$$P_{i,k,j} = P''_{i,k,j} V_{i,k,j} \quad \text{C-1}$$

The total power (TP) can then be found by summing the cell powers over each planar cell, axial cell and rod. Dividing this by the total volume of the fuel rods gives the average rod power density for the core ( $\bar{P}'''_{rod}$ ). The radial power factor can then be determined.

$$RPF_i = \frac{P_i}{V_i} \frac{1}{\bar{P}'''_{rod}} = \frac{P_i I}{TP} \quad \text{C-2}$$

CTF also needs the axial power distribution for each fuel rod. This requires the average power density per flat source plane:

$$\bar{P}'''_{i,plane} = \frac{P_i}{JV_{i,j}} \quad \text{C-3}$$

Where  $V_{i,j}$  is the total volume of a flat source plane (it is assumed the volumes of each flat source plane are identical). Each normalized relative axial power can then be determined as:

$$RPF_{i,j}^{axial} = \frac{P_{i,j}}{V_{i,j}} \frac{1}{\bar{P}'''_{i,plane}} = \frac{P_{i,j} J}{P_i} \quad \text{C-4}$$

The relative radial power is calculated in a similar manner. Once these three sets of variables are calculated, the information is fed into a CTF input deck and the CTF code is run.

CTF then is executed using this power distribution and passed cladding inner and outer temperatures, fuel pellet surface temperature, fuel pellet centerline temperature, bulk temperatures, and bulk densities from the CTF output to a new DeCART input. The moderator, fuel surface and fuel centerline temperatures are only with respect to the radial and axial directions and thus are averaged about the azimuthal direction. Additionally, only one fuel temperature is supplied to DeCART at every axial fuel node. The fuel surface

temperatures and centerline temperatures are combined as shown to define fuel temperature (Doppler) feedback temperature:

$$T_{i,j}^{fuel} = (0.7)T_{i,j}^{surface} + (0.3)T_{i,j}^{cl} \quad C-5$$

This process continues in an iterative fashion until a predetermined convergence criteria is met. The convergence was based on the difference in code calculated temperatures between each iteration. The temperature convergence criteria for these calculations are shown below.

$$Maximum \left( \frac{T_{i+1} - T_i}{T_i} \right) \leq 10^{-3} \quad C-6$$

Additionally the following convergence acceleration technique was used:

$$T_{fuel,i}^{weighted} = (1 - \omega)T_{fuel,i-1} + \omega T_{fuel,i}^{actual} \quad C-7$$

Where  $\omega$  is generally 0.5 for PWRs. This code coupling is capable of running simulations for multiple depletion steps, thus it is able to simulate the entire lifecycle of a fuel load. DeCART tracks isotopic concentrations and reports those concentrations to the next depletion step [6].

### C.3. BISON Coupling

Bison is a finite element based code, and thus the coupling between BISON-CTF and BISON-DeCART cannot be one to one. Additionally, BISON is only capable of modeling one pin at a time. Thus, the information from the DeCART-CTF coupling was stored as output files that were then fed into the BISON code. CTF passes the outer clad surface temperature to BISON where DeCART passes local power information. See Figure C.1 for a project overview. Figure C.2 shows the operating procedure of the Python script that is used to run this code coupling.

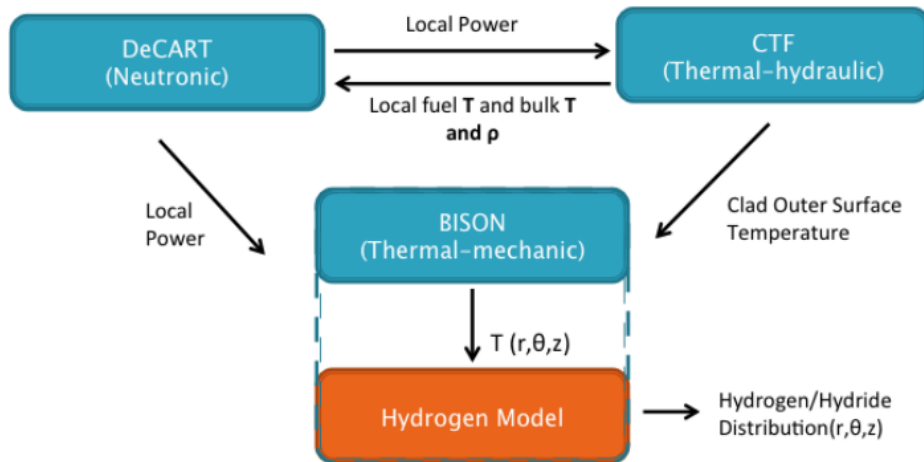


Figure C.1: External Coupling Diagram Between CTF, DeCART, and BISON [6]



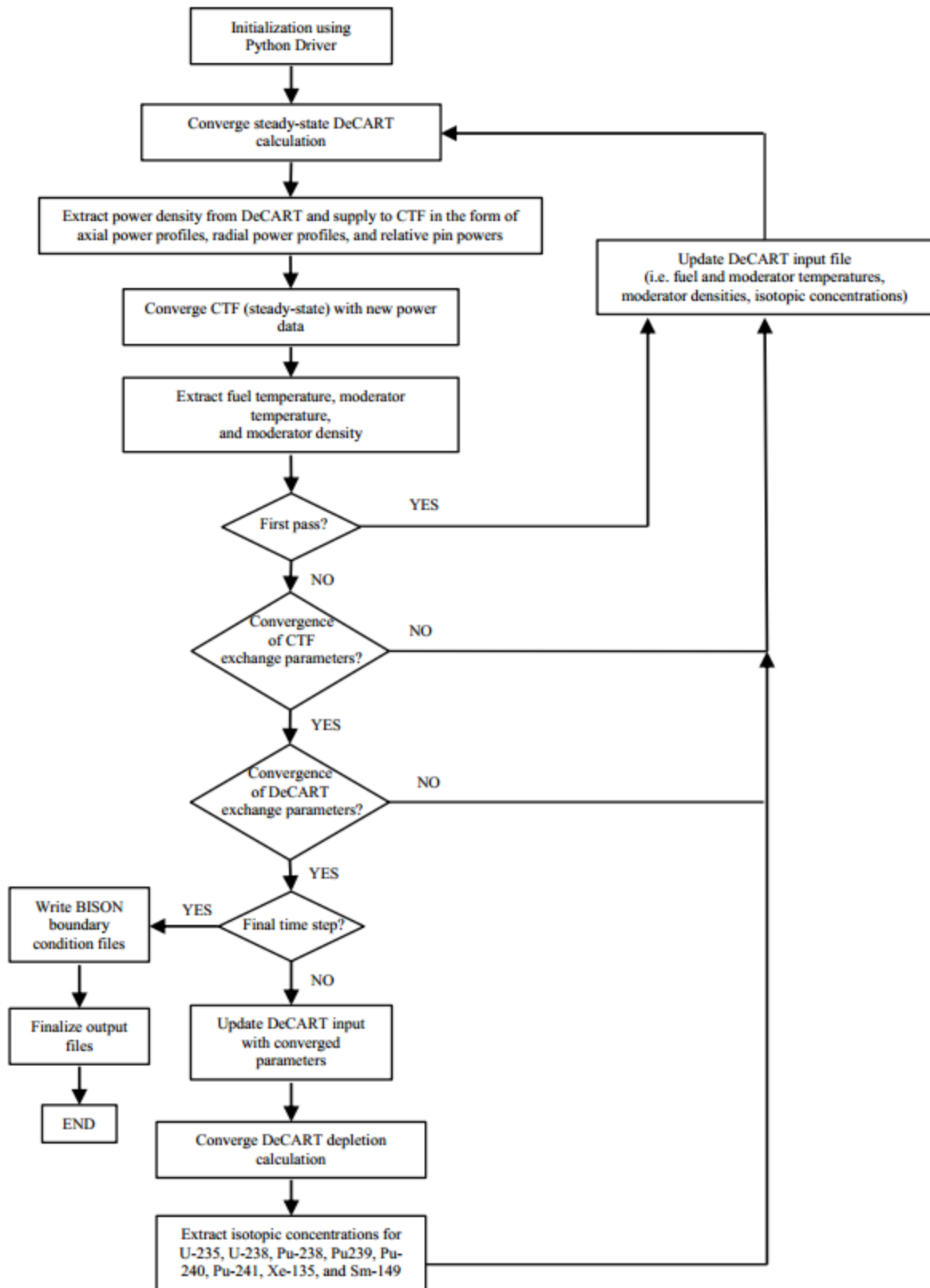


Figure C.2: Code Coupling Python Script Operating Procedure [6]

## C.4. Benchmarking

### C.4.1 4x4 Fuel Rod Sub-Assembly

To test the coupled DeCART-CTF code, a sub-assembly of 16 fuel pins was modeled. The modeling specifications came from two sources. Parameters were borrowed from an Advanced Multi-Physics Nuclear Fuel Performance Code (AMPFuel) study reported in [7], and additional input was borrowed from typical PWR inputs built for use in SIMULATE-3, as part of the university version of the Studsvik Scandpower Code System (CMS) [8]. Table C.1 shows the input parameters used for the primary DeCART and CTF input and Table C.2 and Table C.3 show the additional CTF and DeCART input and boundary conditions, respectively. Figure C.3 shows the layout of the sub-assembly fuel pins and the CTF subchannels. Figure C.4 shows the nodding breakdown of the fuel pins in DeCART. Each fuel pin (including fuel pellet and cladding) is broken into four azimuthal sections. Additionally, the fuel pellet is broken into three radial sections. Figure C.5 and Figure C.6 show the geometric parameters used as input for CTF. The prior shows the crossflow points between each subchannel and the latter diagrams the gap connections.

Table C.1: Specifications for DeCART-CTF Coupled 4x4 Test Simulation

Parameter	Value	Units
Reactor	PWR	
Layout	4 x 4	
Fuel	UO <sub>2</sub>	
Enrichment	3.45	
Fuel Density	10.4	g/cm <sup>3</sup>
Percent Theoretical Density	0.95	
Burnable Poison	None	
Cladding	Zircaloy-4	
Cladding Density	6.55	g/cm <sup>3</sup>
Coolant	H <sub>2</sub> O	
Fill Gas	Helium	
Fill Gas Density	0.0002	g/cm <sup>3</sup>
Fuel Pellet radius	4.095E-3	m
Cladding Inner Radius	4.18E-3	m
Cladding Outer Radius	4.75E-3	m
Cladding Thickness	5.70E-4	m
Pin Pitch	1.26E-2	m
Active Fuel Height	3.6576	m
Top Reflector Height	0.35512	m
Bottom Reflector Height	0.35512	m
Array Power	1.0808	MW
Average Linear Heat Rate	18.5	kW/m
Core Pressure	15.5	MPa
Mass Flow Rate	4.86	Kg/s
Beginning of Cycle boron loading	1000	Ppm
Inlet Temperature	287	°C

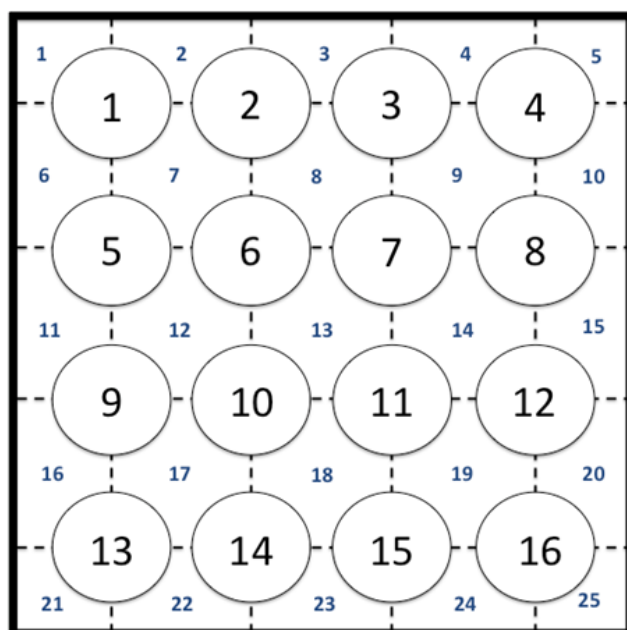


Figure C.3: Rod and sub-channel nomenclature used in CTF's format [6]

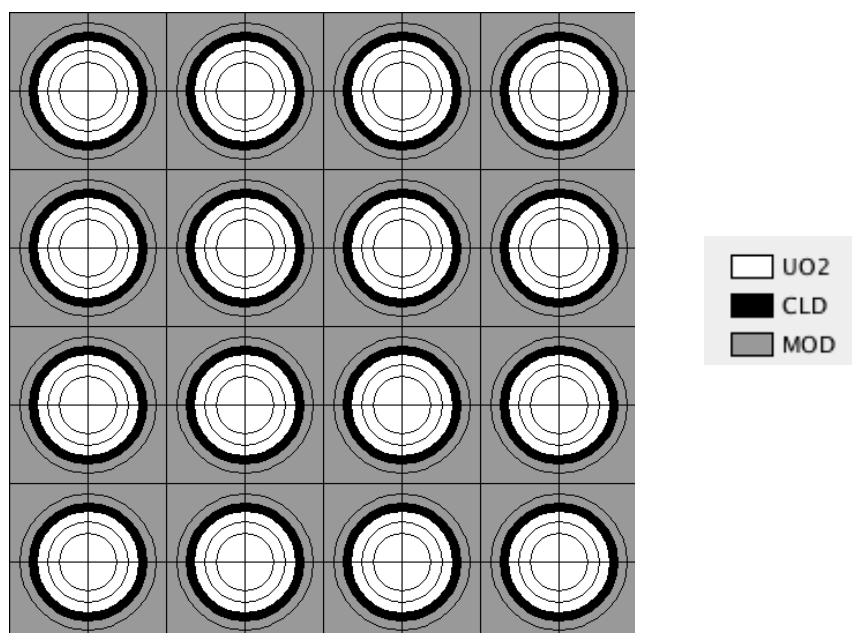


Figure C.4: DeCART Noding Breakdown for 4x4 fuel pin sub-assembly [6]

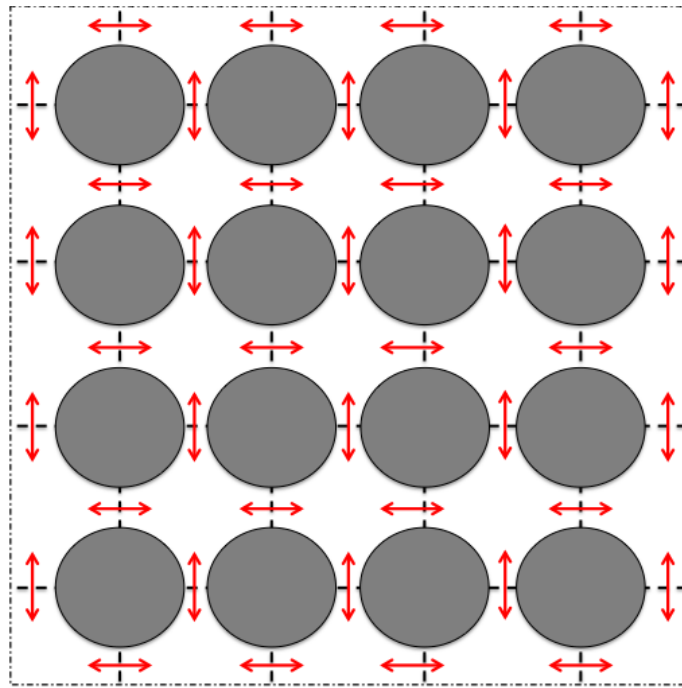


Figure C.5: CTF Crossflow Diagram for 4x4 Sub-Assembly [6]

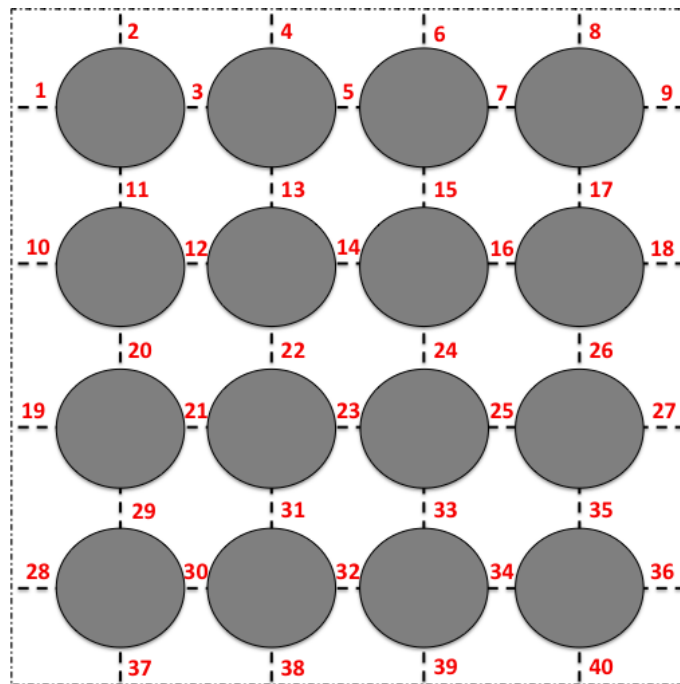


Figure C.6: CTF Gap Connection Diagram for 4x4 Sub-Assembly [6]

Table C.2: Input Parameters for CTF for 4x4 Sub-Assembly [6]

Parameter	Value	Units
Enthalpy of the Fluid		
Inlet	1233	kJ/kg
Outlet	1434	kJ/kg
Subchannel Flow Areas		
Center	8.77E-5	m <sup>2</sup>
Side	4.38E-5	m <sup>2</sup>
Corner	2.19E-5	m <sup>2</sup>
Wetted Perimeter		
Center	2.99E-2	m
Side	1.50E-2	m
Corner	7.48E-3	m
Gap Thickness		
Center	3.08E-3	m
Side/Corner	1.54E-3	m
Distance Between Channel Centers		
Center-to-Center	1.26E-2	m
Side-to-Side	1.26E-2	m
Side-to-Center	9.45E-3	m
Side-to-Corner	4.43E-3	M
Pressure Loss Coefficient of Spacer	0.9529	

Table C.3: Input Parameters for DeCART for 4x4 Sub-Assembly [6]

Parameter	Value	Units
Weight % in UO <sub>2</sub>		
U-235	3.00%	
U-238	85.14%	
O-16	11.86%	
Weight % in Zircaloy-4		
Natural Zr	98.298%	
Natural Sn	1.450%	
Natural Fe	0.145%	
Natural Cr	0.100%	
Natural Ni	0.007%	
Depletion Step Size	2.5	MWD/kgHM
Number of Azimuthal Divisions in Fuel Region	4	
Number of Radial Divisions in Fuel Region	3	
Number of Axial Divisions in Fuel Region	18	
Albedo Boundary Conditions		
Top/Bottom	Vacuum	
Sides	Reflective	

These parameters were input into the coupled CTF-DeCART code and run for approximately 1036 full power days or 40 MWd/kgU. The coupling convergence output between DeCART and CTF for the first burnup step (0.0 MWd/kgU) is shown in Table C.4.

Table C.4: Convergence Parameters for CTF-DeCART 4x4 Fuel Pin Sub-Assembly [6]

Iteration	Converged Parameter	Maximum Change Between Iterations	DeCART k-eff Output
1	--	--	1.188050
2	--	0.00798653	1.194568
3	Moderator Density	0.02980640	1.194437
4	Moderator Temperature	0.00937195	1.194527
5	--	0.00430280	1.194547
6	Fuel Surface Temperature	0.00180460	1.194547
7	Fuel Centerline Temperature	0.00075010	1.194550

In Table C.4, the maximum iteration change in each step was from the fuel centerline temperature. This parameter was the last to converge at each burnup step. As mentioned previously, the convergence criteria for the coupling specified that the maximum local change between iterations had to be less than  $1.0\text{E-}3$ . Another item of note in Table C.4 is the k-eff being greater than one. This would imply that the reactor is super critical, however, this is just for an isolated 4x4 section of the assembly. The primary cause for this is the lack of leakage due to the reflective boundary conditions i.e. the radial leakage is neglected leading to supercritical configuration.

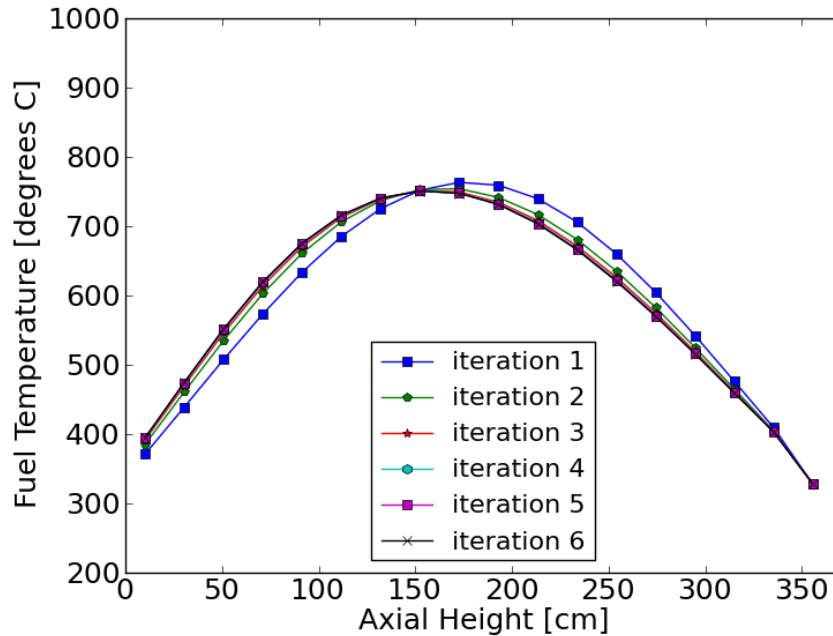


Figure C.7: Convergence of the fuel temperature at 0.0 MWd/kgU [6]

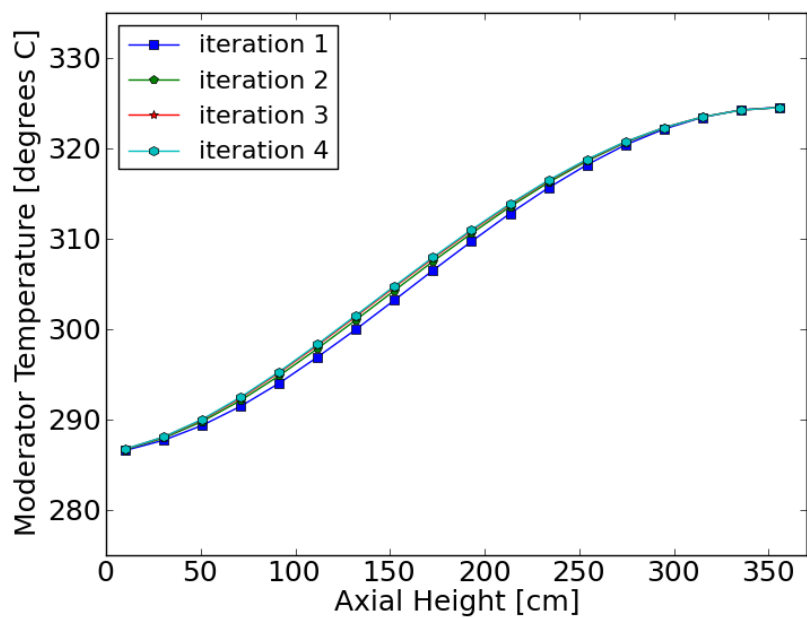


Figure C.8: Rod 7 convergence of the moderator temperature at 0.0 MWd/kgU [6]

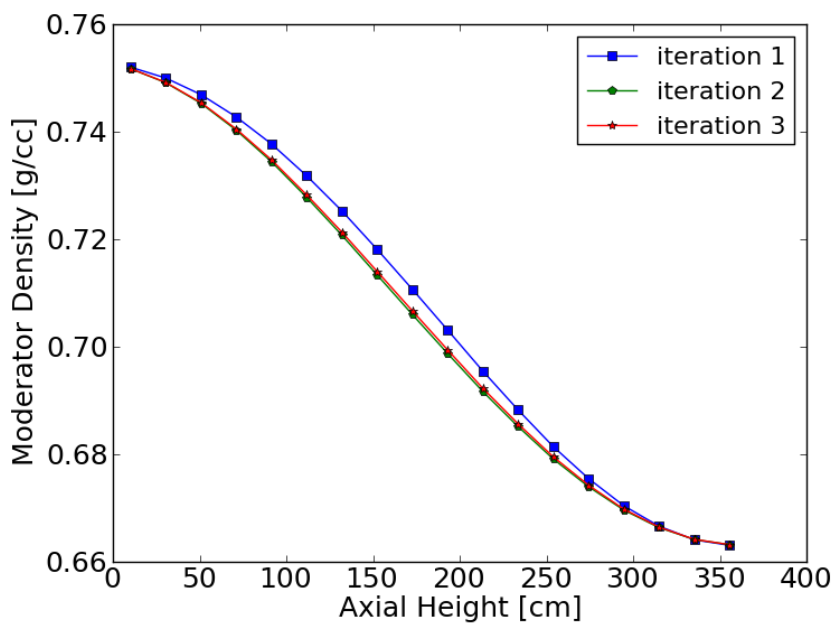


Figure C.9: Rod 7 Convergence of the Moderator Density at 0.0 MWd/kgU [6]

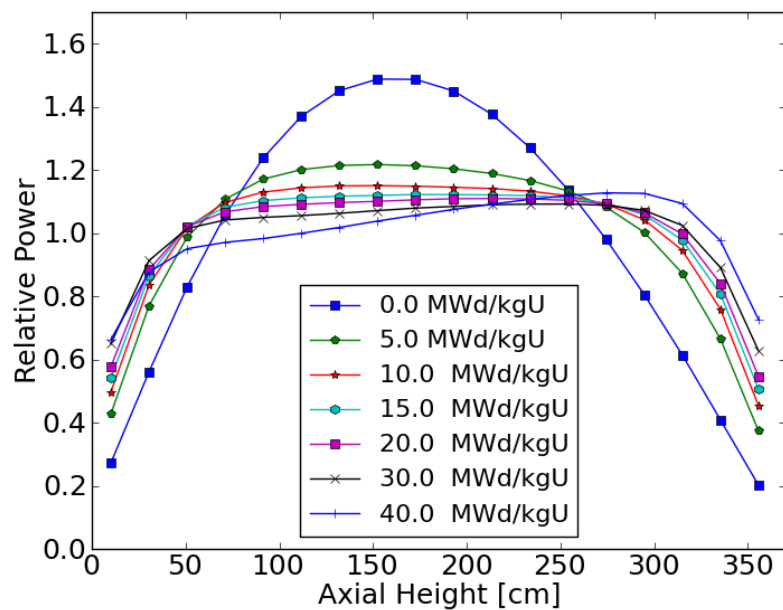


Figure C.10: Rod 7 Converged Axial Power Distributions [6]

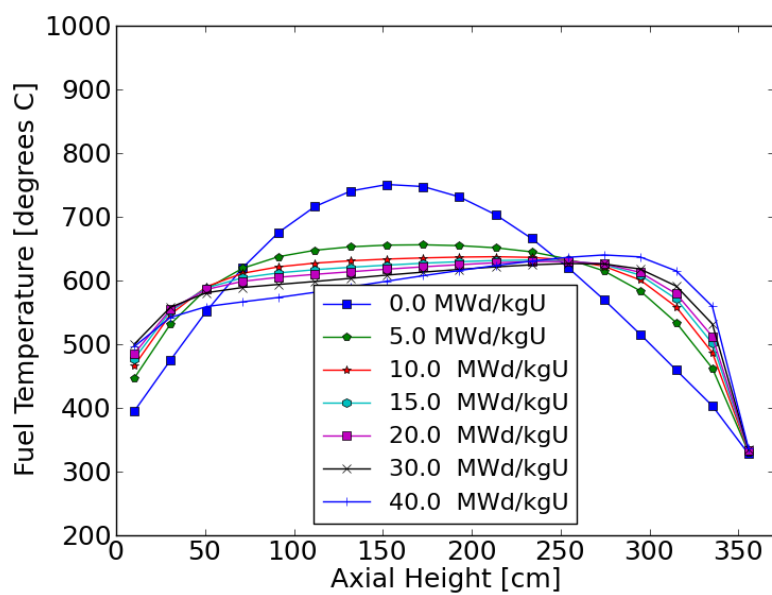


Figure C.11: Rod 7 Average Fuel Temperatures [6]



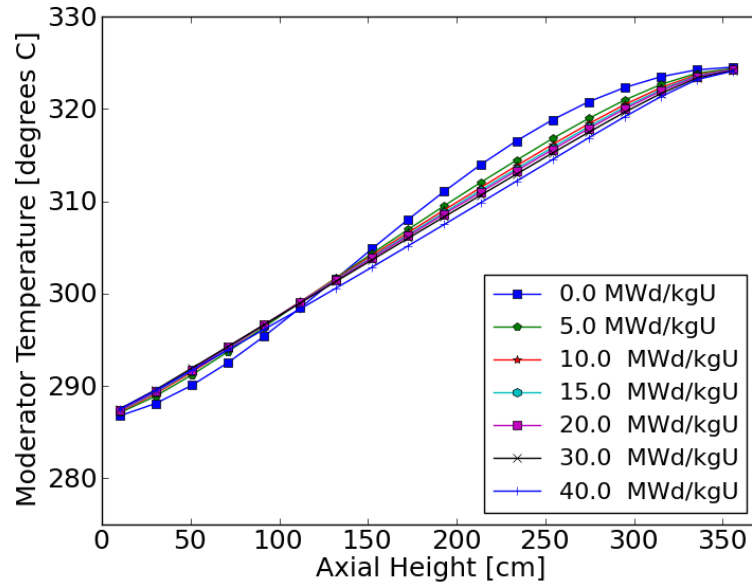


Figure C.12: Rod 7 Converged Moderator Temperature Profiles [6]

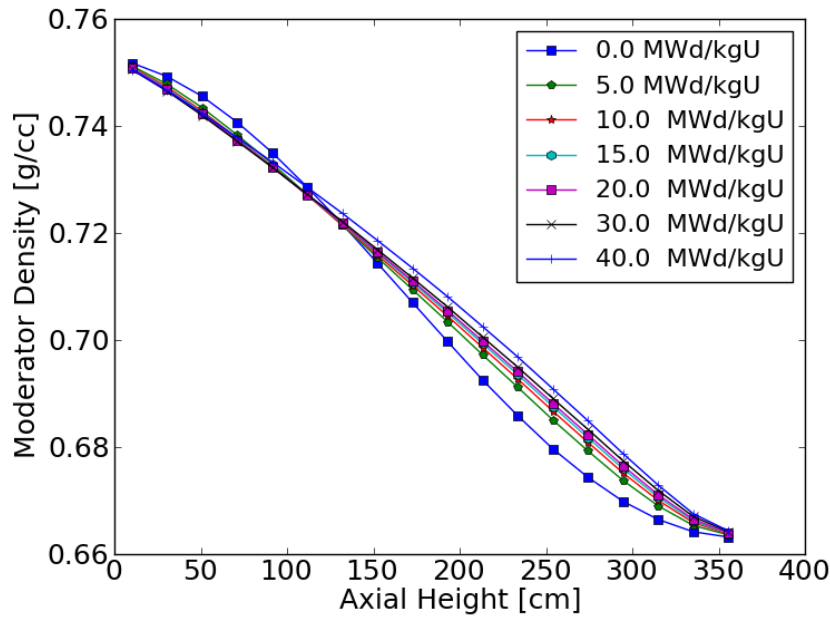


Figure C.13: Rod 7 Converged Moderator Density Profiles [6]

Without experimental data to check the correctness of the coupling for modeling 4x4 PWR sub-assembly sections with only fuel pins, a comparison was done between standalone DeCART calculations and coupled CTF-DeCART calculations. One of the primary goals of the CTF temperature and density feedback is to update the cross-sections during depletion. DeCART also offer an option to update the cross-sections at designated burnup values (i.e. every 2.5 MWd/kgU). The default cross-section update option occurs every 10 MWd/kgU in DeCART. This option was decreased to 2.5 MWd/kgU to observe

the effect on power distribution over time. The details of this comparison are seen in Figures Figure C.14 through Figure C.17.

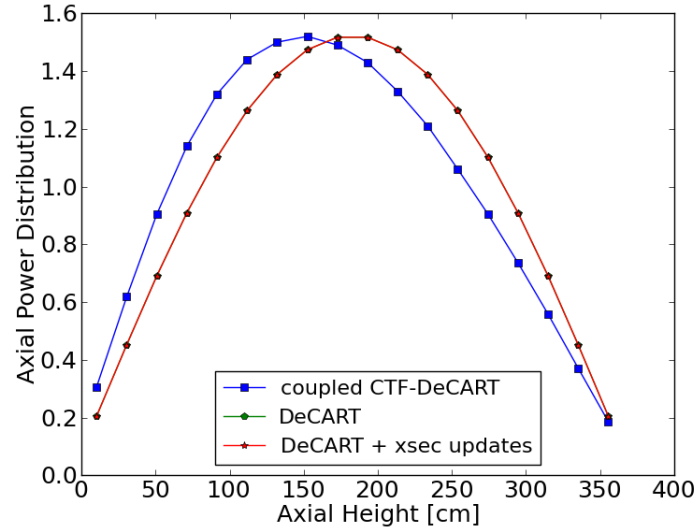


Figure C.14: Comparison of CTF-DeCART vs DeCART Standalone Axial Power Distribution for Rod 7 at 0.0 MWd/kgU [6]

Though it cannot be seen in Figure C.14, the axial power distribution calculated in a standalone DeCART calculation with extra cross-section updates directly overlaps the axial power distribution for the standalone DeCART calculation with default cross-section update. At BOC there is no added benefit for increasing the number of cross-section updates. Furthermore, without the temperature feedback to the cross-sections, the axial power distribution follows a perfect cosine shape.

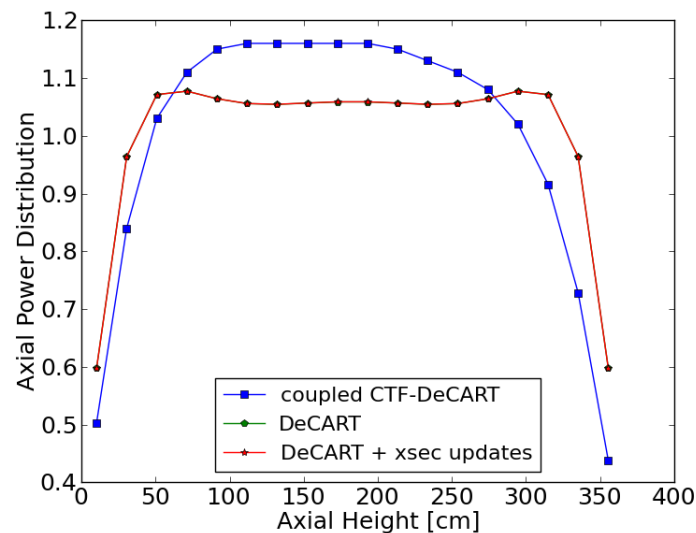


Figure C.15: Comparison of Coupled CTF-DeCART to the Standalone DeCART Axial Power Distribution for rod 7 at 10.0 MWd/kgU.[6]

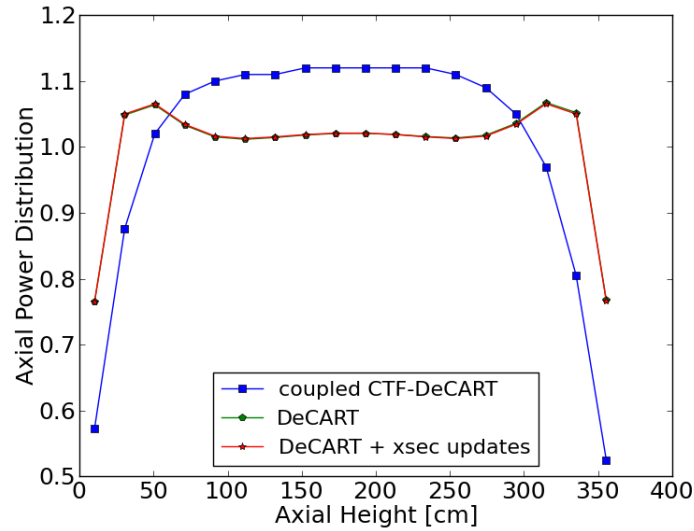


Figure C.16: Comparison of Coupled CTF-DeCART to the Standalone DeCART Axial Power Distribution for rod 7 at 20.0 MWd/kgU.[6]

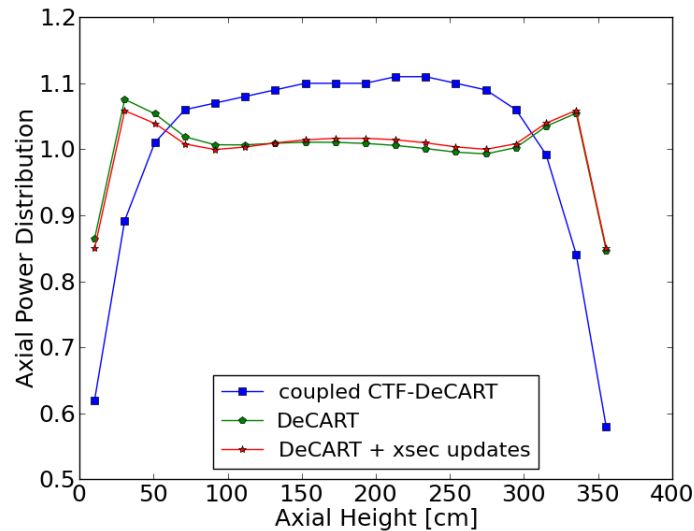


Figure C.17: Comparison of Coupled CTF-DeCART to the Standalone DeCART Axial Power Distribution for rod 7 at 27.5 MWd/kgU. [6]

Through the progression of Figure C.14 to Figure C.17, both the coupled and standalone axial power distribution flattens out. Though, the effect is much more severe in the standalone DeCART calculations. The added cross-section updates do not have an effect on the latter depletion steps either. The cross-sections are determined in DeCART based on the inputted temperatures for various material regions. Without any sort of temperature distribution feedback given in the standalone DeCART models, the cross-sections will not change. For this reason, there is no change in the axial power profiles for DeCART models with an increased number of cross-section updates.

Also, the axial offset anomaly described in Wagner's report is not seen in the standalone DeCART calculations. While the power suppression is observed in the center region of the fuel, the power shape in the bottom half of the core is the same as in the top half of the core for any burnup in the standalone DeCART calculations. In most cases, it is known that more reactivity exists in the lower region of the core, and this is reflected when DeCART is coupled with CTF, receiving temperature and density feedback for cross-section generations.

#### C.4.2 DeCART-CTF 4x4 Sub-Assembly with Guide Tube

To further test the coupled code, a single fuel rod from the previous sub-assembly was replaced with a control rod guide tube (water rod). This section of assembly is taken from the ORNL AMPFuel 17x17


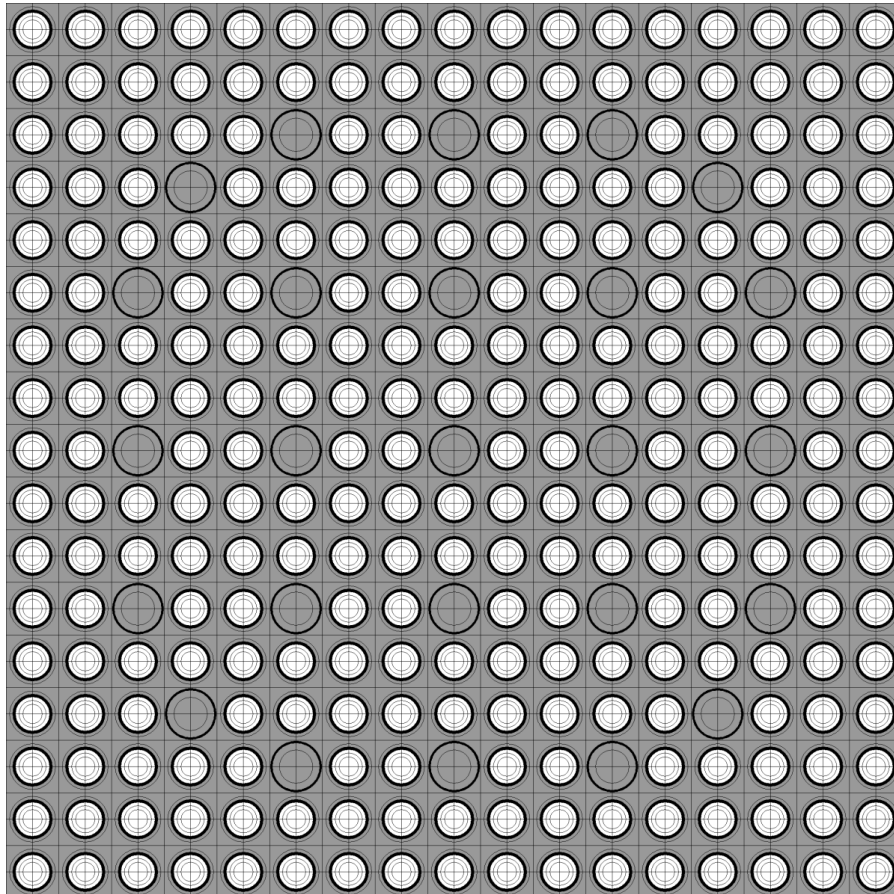
assembly model [7] as shown in 

Figure C.18. Figure C.19 Shows the 4x4 selection for the DeCART-CTF coupled calculation. All other dimensions, boundary conditions and parameters remained the same as in the original all fuel 4x4 sub-assembly. The guide tube is made of Zircaloy-4 and has an inner diameter of 0.5715 cm and an outer diameter of 0.612 cm.



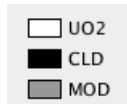


Figure C.18: ORNL AMPFuel Full 17x17 Assembly [6]

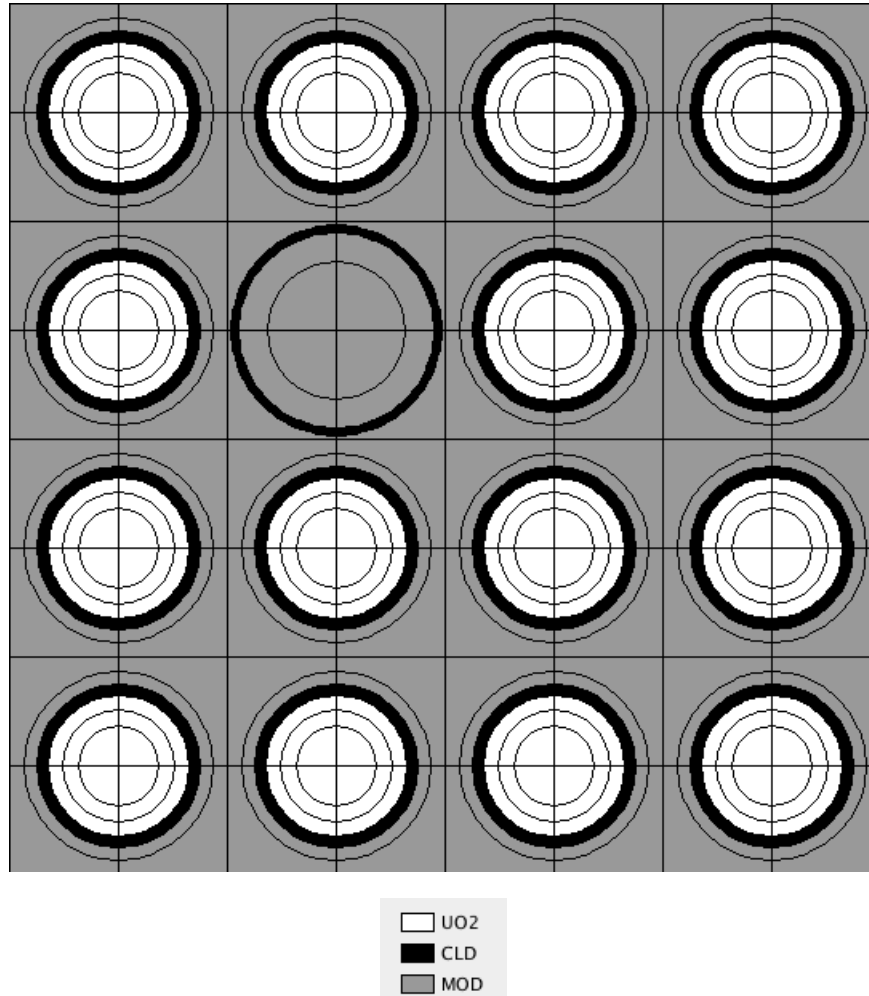
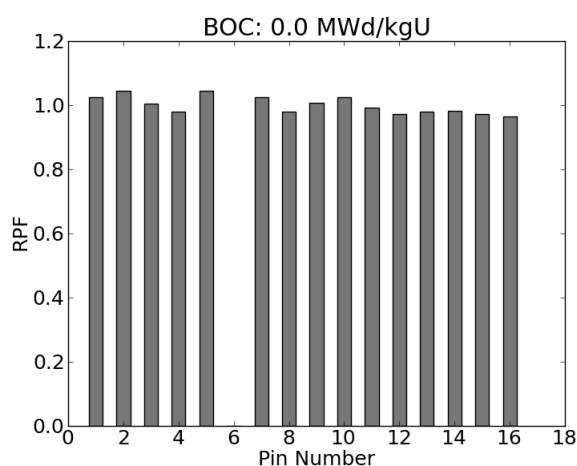
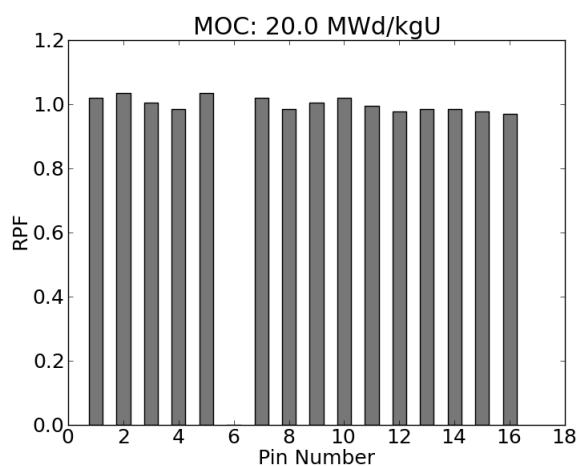


Figure C.19: 4x4 Sub-Assembly Selected from ORNL AMPFuel Full 17x17 Assembly Model [6]

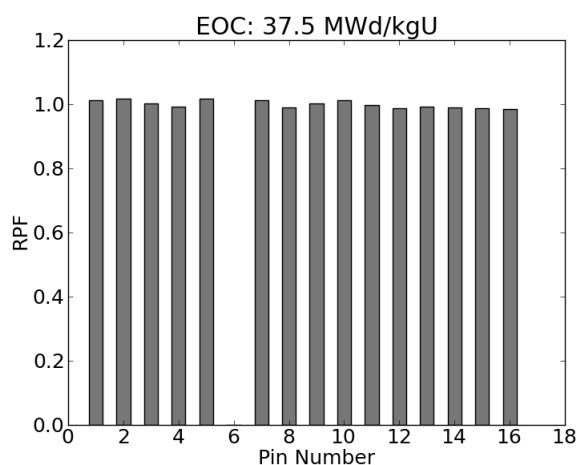
The tube in position six is a guide tube for a control rod. For this model, the total power was left as a 1.01325 MW. For this model, coupled CTF-DeCART calculations were carried out to 37.5 MWd/kgU. The coupled CTF-DeCART calculations were ran on 2 nodes with 1 processor per node; computational time for this simulation ended at 24 hours. The first set of results to show is the radial power factors from their respective converged iterations at certain depletion steps. Figure C.20 shows the radial power factors for all 16 pin locations in the form of bar graphs. The bar graph values are calculated in the coupling. Three time domains are represented: BOC, middle of cycle (MOC), and EOC. The 2-D plane view images to the right of the bar graphs show the axially integrated pin powers for the respective burnups calculated internally in DeCART.



1.0243	1.0447	1.0060	0.9804
1.0449		1.0248	0.9812
1.0064	1.0250	0.9926	0.9714
0.9810	0.9816	0.9716	0.9640



1.0203	1.0338	1.0058	0.9854
1.0339		1.0195	0.9843
1.0060	1.0196	0.9947	0.9778
0.9856	0.9844	0.9778	0.9712



1.0114	1.0181	1.0036	0.9925
1.0181		1.0114	0.9906
1.0035	1.0114	0.9972	0.9878
0.9923	0.9905	0.9878	0.9839

Figure C.20: Radial Power Factors at BOC, MOC, and EOC for “Internal” Array [6]

As expected, the pins with the highest relative power are those directly adjacent to the guide tube. Filled with coolant, the guide tube offers an area of increased moderation compared to cells with fuel rods. Therefore, it makes sense that fuel rods next to regions of increased moderation would experience higher

power output. At BOC, it is important to point out that pins 2 and 5 have slightly higher Radial Peaking Factors (RPFs) than pins 7 and 10, which are also adjacent to the guide tube. This occurs as a result of the reflective boundary conditions imposed in DeCART. With reflective boundary conditions, pin 2 experiences the effects of a guide tube in the cell directly adjacent to its northern border. Similarly, pin 5 experiences the effects of a guide tube directly adjacent to its western border. The next closest guide tube to pin 7's eastern border is three cells away; the next closest guide tube to pin 10's southern border is three cells away. Recalling the effects of axial offset during depletion, the same logic can be applied to the RPFs. Since pins 2, 5, 7, and 10 are adjacent to regions of increased moderation (i.e. higher reactivity), they deplete faster than the other rods in the array. This effect is seen in Figure C.20 as the RPFs become more uniform over the array with burnup. Referring now to the convergence of the "Internal" model, Figure C.5 shows the iteration data of the CTF-DeCART coupling at the BOC depletion step.

Table C.5: Convergence of CTF-DeCART Coupled Calculations at 0.0 MWd/kgU for "Internal" [6]

Iteration	Converged Parameter	Maximum Local Change b/w Iterations	k-eff from DeCART
1 (first pass)	--	--	1.176745
2	moderator temperature	0.023667	1.195705
3	moderator density	0.010705	1.195786
4	--	0.004671	1.195819
5	--	0.002205	1.195828
6	fuel surface temperature	0.001040	1.195831
7	fuel CL temperature	0.000433	1.195840

\*Maximum local change remains in the fuel centerline temperature for all iterations

The "Internal" case converged in 7 iterations for the BOC depletion step. In the final iteration the k-effective changed by a relative difference of 7.526E-06 and an absolute difference of 9 pcm. Again, in this coupled model the k-effective is above the 'critical' value of 1.0, causing the array to be supercritical. The reason is that the radial leakage is not modeled.

Convergence of the fuel temperature, moderator temperature, and moderator density followed similar patterns to the 4x4 sub-assembly with only fuel pins. As seen in Figure C.20, the largest radial power factor for the BOC depletion step occurs in Rod 2 and Rod 5. For Rod 2 the convergence of the fuel centerline temperature is shown in Figure C.21; fuel surface temperature in Figure C.22; moderator temperature in Figure C.23; moderator density in Figure C.24. All convergence plots depict results from the BOC depletion step (0.0 MWd/kgU).

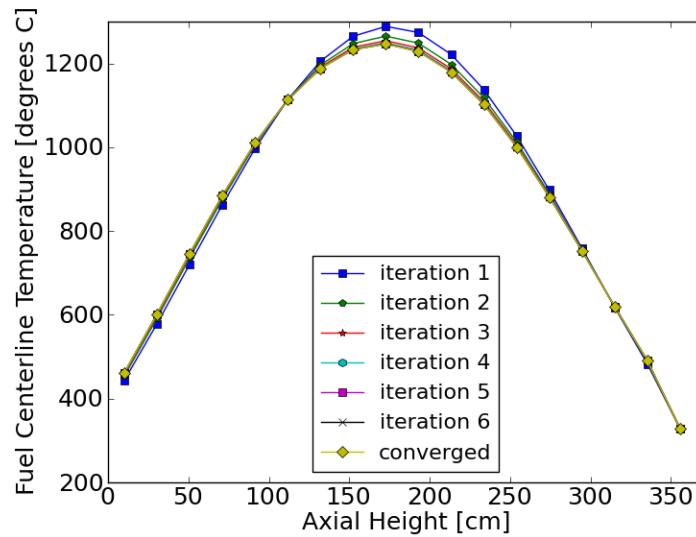


Figure C.21: Rod 2 Convergence of the Fuel Centerline Temperature at 0.0 MWd/kgU for “Internal” [6]

The convergence of the fuel temperatures in Figure C.21 do transition from a cosine shape to very slightly bottom-peaked. Note that again the convergence of the moderator temperature and density occurs much quicker. A possible reason for this is that CTF models the heat transfer in the coolant much better than in the fuel or clad regions.

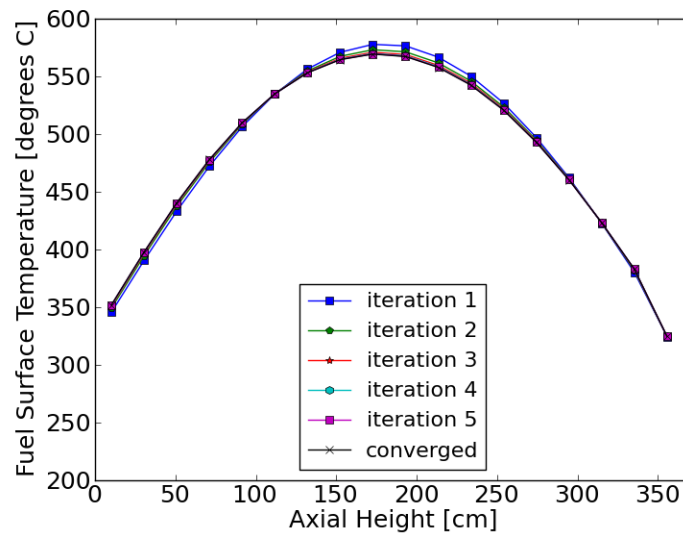


Figure C.22: Rod 2 Convergence of the Fuel Surface Temperature at 0.0 MWd/kgU for “Internal” [6]



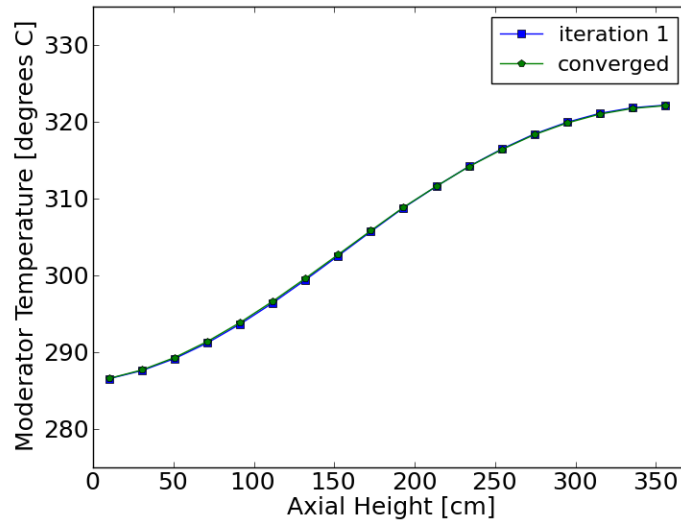


Figure C.23: Rod 2 Convergence of the Moderator Temperature at 0.0 MWd/kgU for “Internal” [6]

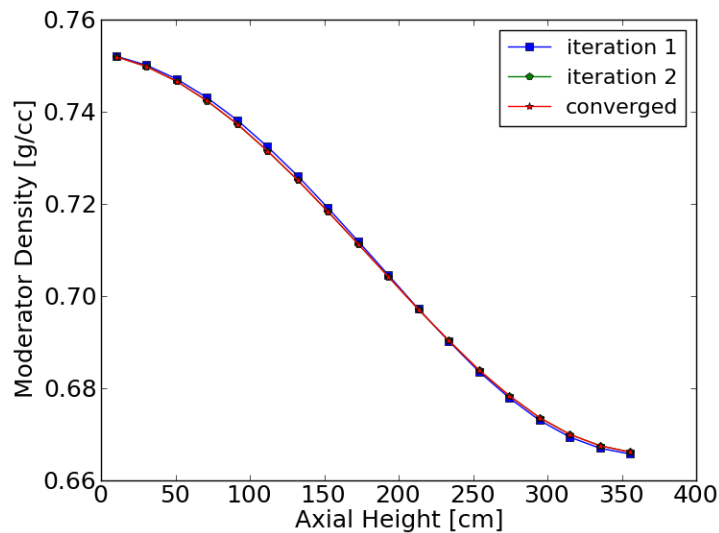


Figure C.24: Rod 2 Convergence of the Moderator Density at 0.0 MWd/kgU for “Internal” [6]

After convergence is reached for each depletion step, the axial power distributions are stored. Figure C.25 shows the axial power distributions for rod 2 and rod 16 as they evolve with time. Two plots are provided together to give a comparison between a rod adjacent to the guide tube, and the furthest fuel rod from the guide tube. Similarly, the converged values for the average fuel centerline temperature, fuel surface temperature, moderator temperature, and moderator density are store for further analysis. They are shown in Figure C.27, Figure C.28, and Figure C.29 respectively. Though the clad outer surface temperature is not used as an exchange parameter for coupled CTF-DeCART calculations, it is needed as a boundary condition for BISON. Therefore, clad temperature distributions are also stored for each converged depletion step, and are shown in Figure C.31 for Rod 2.

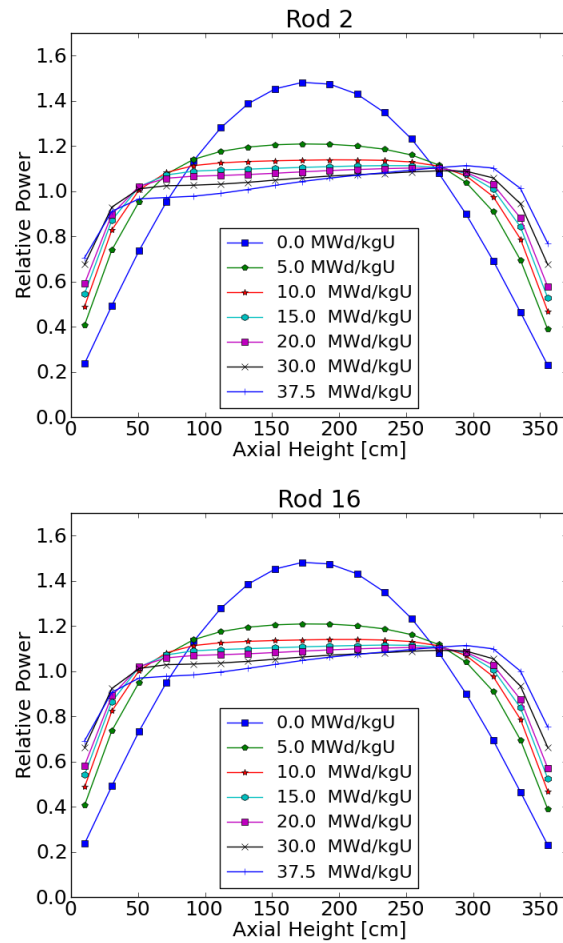


Figure C.25: Rod 2 Axial Power Shapes as a Function of Burnup for “Internal” [6]

Though Rods 2 and 7 share almost identical axial power shapes, the radial power factors between the two rods differs by about 8% at BOC. Also, it should be noted that the axial power shapes for later burnups in Figure C.25 match those from the 4x4 sub-assembly model with all fuel pins shown in the previous section.

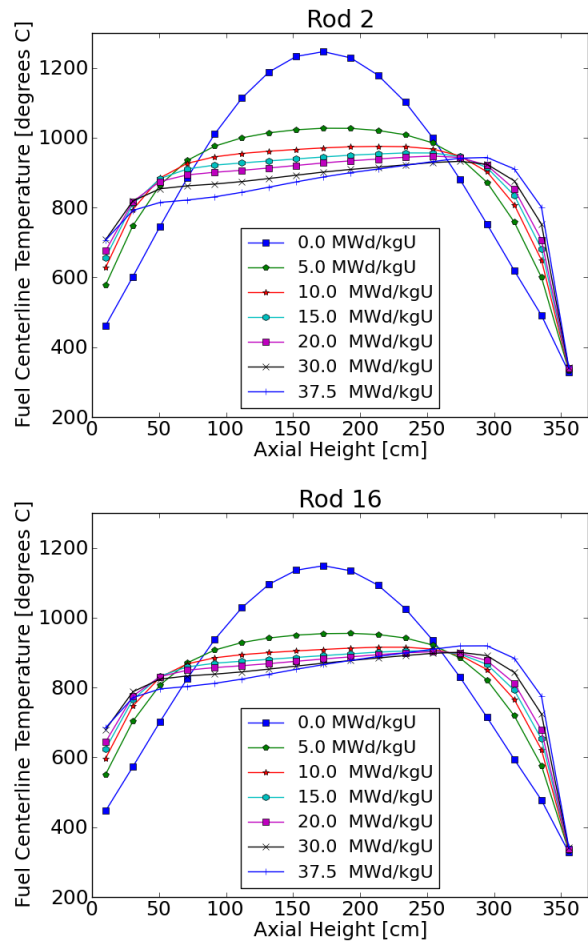


Figure C.26: Rod 2 and Rod 16 Converged Fuel Centerline Temperature Distributions for “Internal” [6]

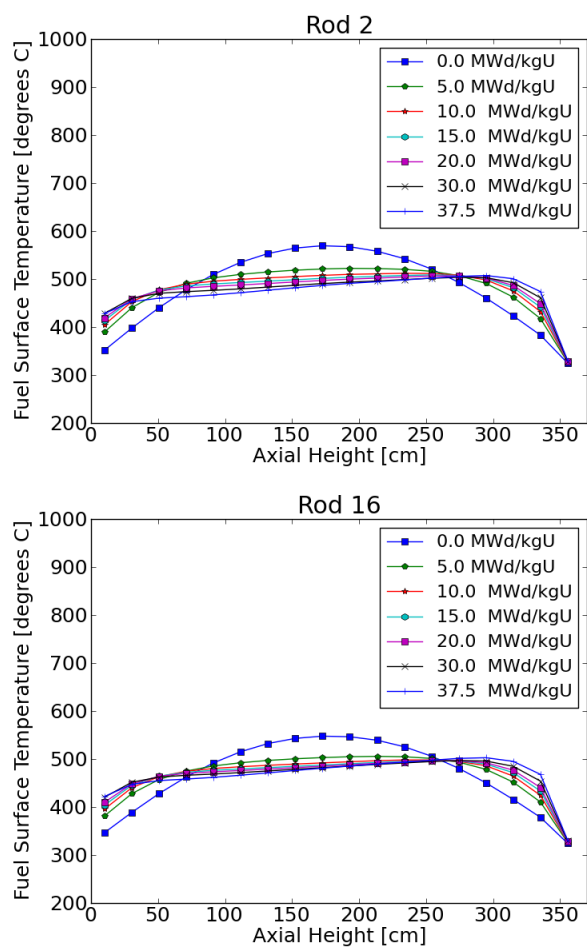


Figure C.27: Rod 2 and Rod 16 Converged Fuel Surface Temperature Distributions for “Internal” [6]

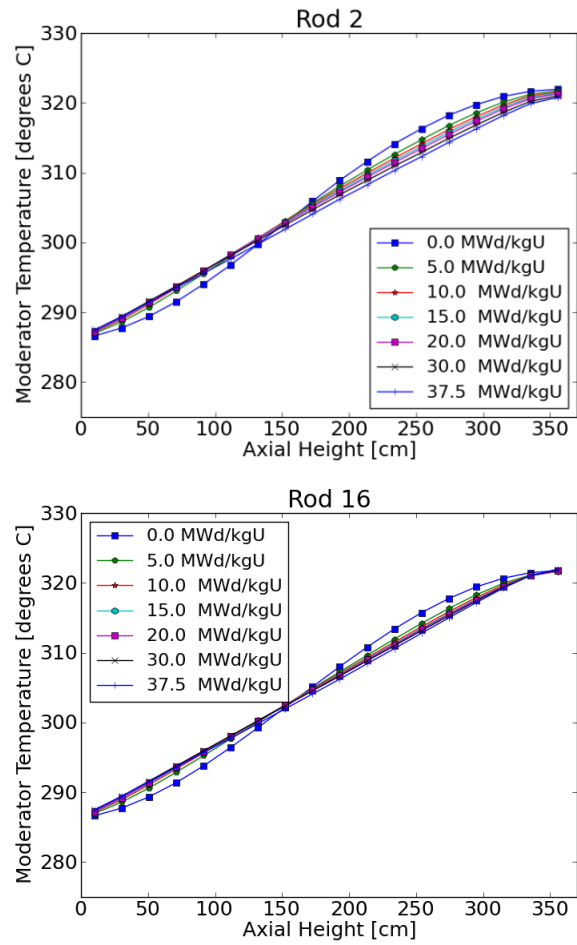


Figure C.28: Rod 2 and Rod 16 Converged Moderator Temperature Distributions for “Internal” [6]

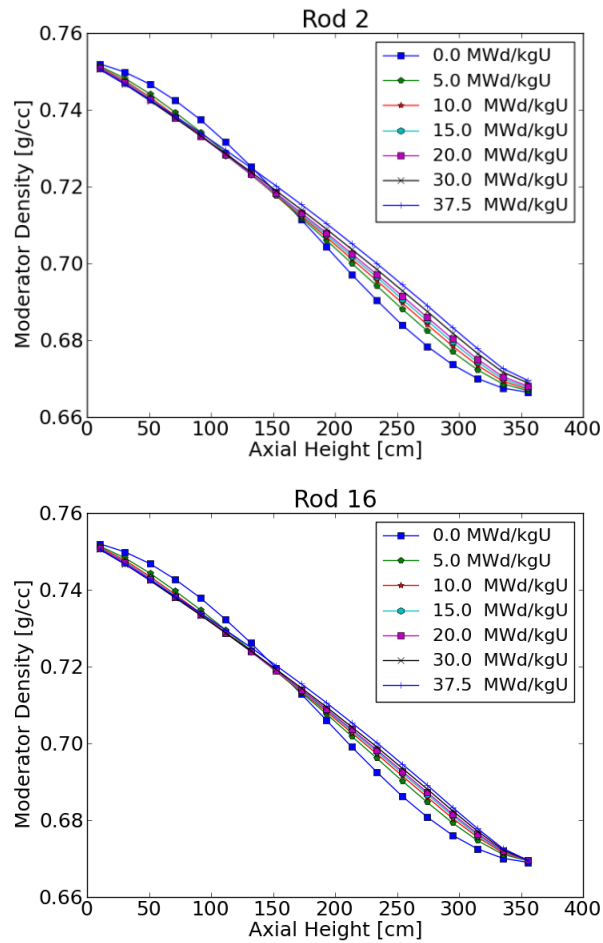


Figure C.29: Rod 2 and Rod 16 Converged Moderator Density Distributions for “Internal” [6]

As expected, the fuel temperature profiles and axial power distributions follow each other closely. In comparison with the axial power distributions from the 4x4 array with only fuel pins (last report), the axial power distributions in Figure C.25, follow the cosine function and are not bottom-peaked. It is important to highlight this difference to show the effect guide tubes can have on the axial power distribution of neighboring fuel pins.

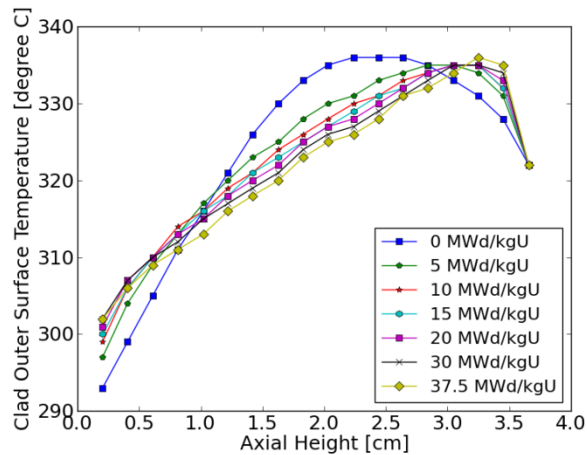


Figure C.30: Rod 2 Clad Outer Surface Temperature Distributions for “Internal” [6]

Figure C.30 visualizes the liquids temperatures in subchannels 7 and 19. Subchannel 7 is an internal channel connected to fuel rods 1, 2, and 5, and also the guide tube in position 6. Subchannel 19 is connected to four fuel rods in positions 11, 12, 15, and 16. Refer to Figure C.3 and Figure C.5 to see this particular layout.

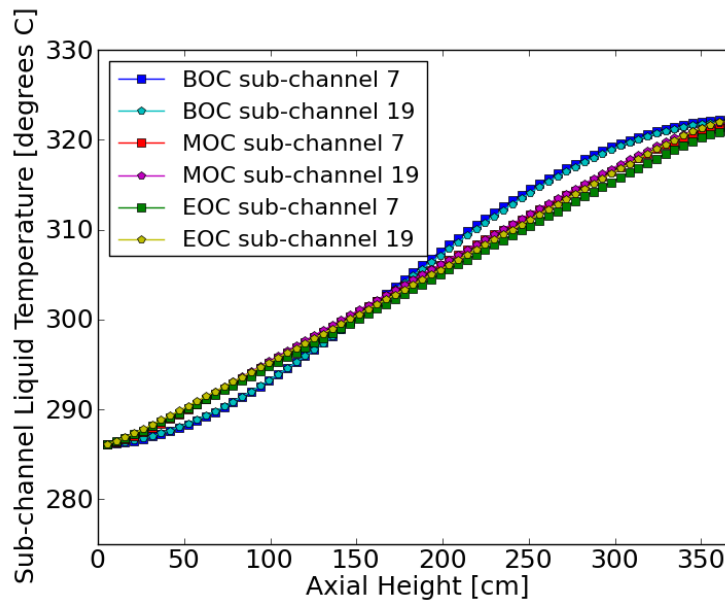


Figure C.31: Subchannel 7 and 19 Liquid Temperature Distributions for “Internal” [6]

Reviewing the results from Figure C.31, it can be deduced that for a relatively small section of a PWR core, there does not exist a significant variation in the heat transfer characteristics of nearby fuel pins. Furthermore, on the scale of a 4x4 sub-assembly array isolated from the effects of the rest of the core, the addition of guide tubes into the model does not significantly change the outcome. Studies would need to expand to larger fuel arrays, or include different radial boundary conditions to see any significant effect. DeCART requires global albedo boundary conditions surrounding the model. To apply realistic non-uniform albedo conditions, surface currents across lattice cells need to be calculated from whole core

simulations. If reflective boundary conditions are placed on a sub-assembly model, guide tubes may not be placed on the periphery. Doing so places a reflected guide tube adjacent to the one in the model, providing not only an unrealistic pin configuration, but also significantly decreases the moderator temperature in this region. As a result, neutron economy is increased greatly and unexpected power and temperature profiles are observed.

### C.4.3 CTF-DeCART Comparison with Frapcon Integral Assessment Case

In addition to the BISON standalone comparison to the Frapcon results, the coupled CTF-DeCART was also used to model the Ocone rod 15309 and used as a benchmark against the FRAPCON output. The FRAPCON experiment and data are the same as in section B.1. Figure C.32 shows the axial power shapes of FRAPCON and Figure C.33 through Figure C.38 show the CTF-DeCART axial power outputs plotted against the FRAPCON results.

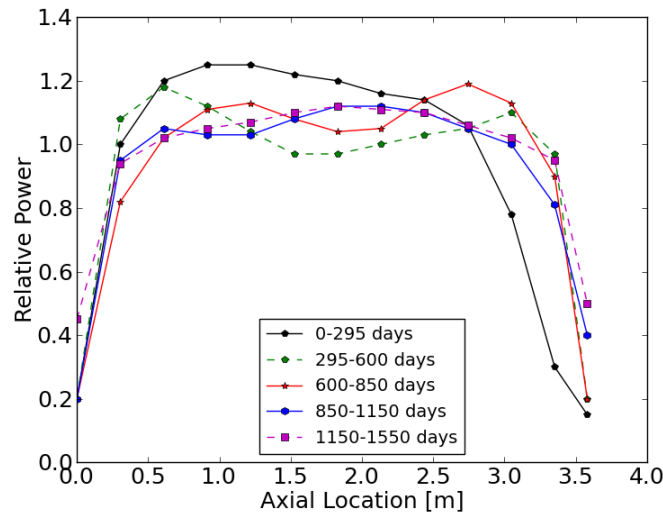


Figure C.32: FRAPCON Axial Power shapes [6]

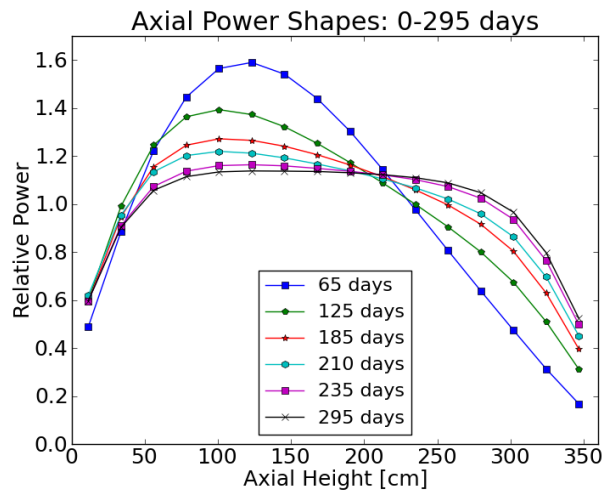


Figure C.33: Rod 15309 Axial Power Shapes from the CTF-DeCART Coupling [6]



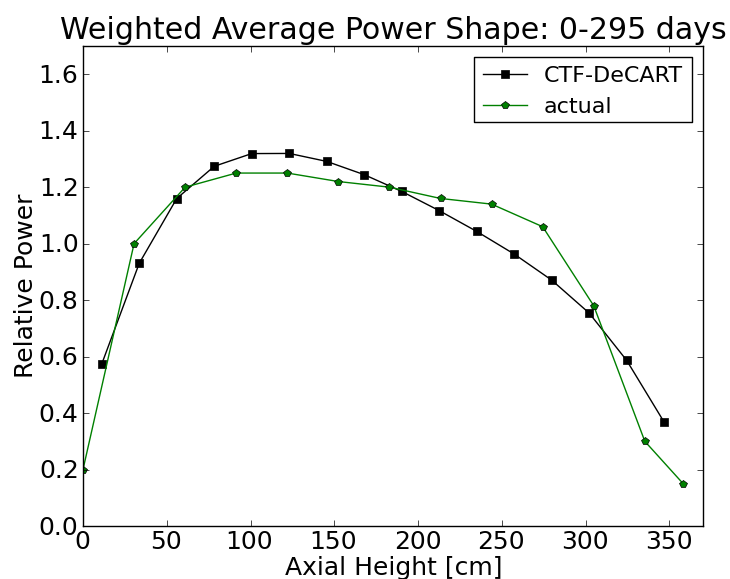


Figure C.34: CTF-DeCART vs Actual Axial Power Shape (0-295 days) [6]

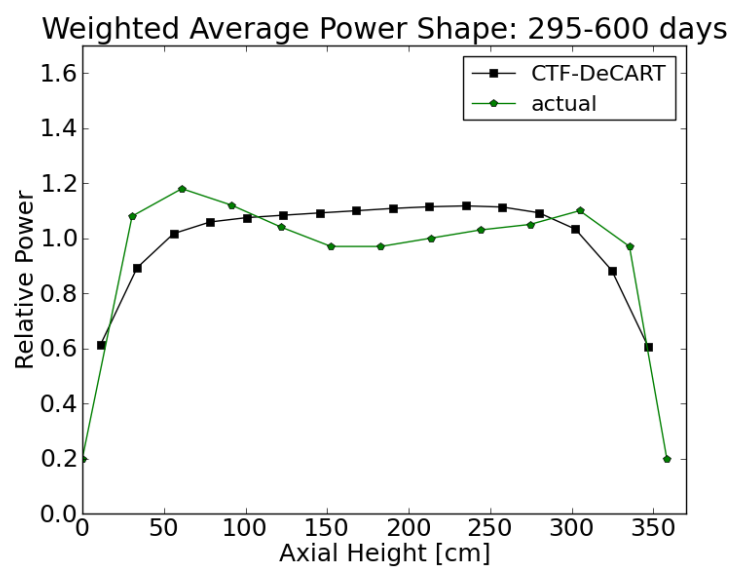


Figure C.35: CTF-DeCART vs Actual Axial Power Shape (295-600 days) [6]

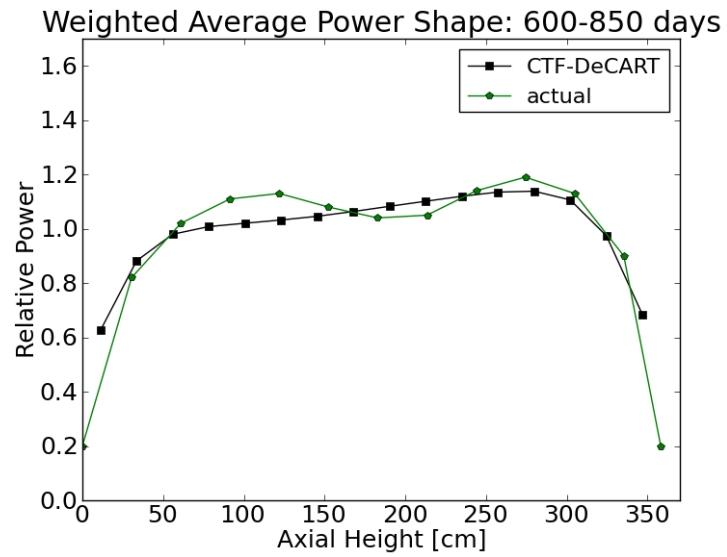


Figure C.36: CTF-DeCART vs Actual Axial Power Shape (600-850 days) [6]

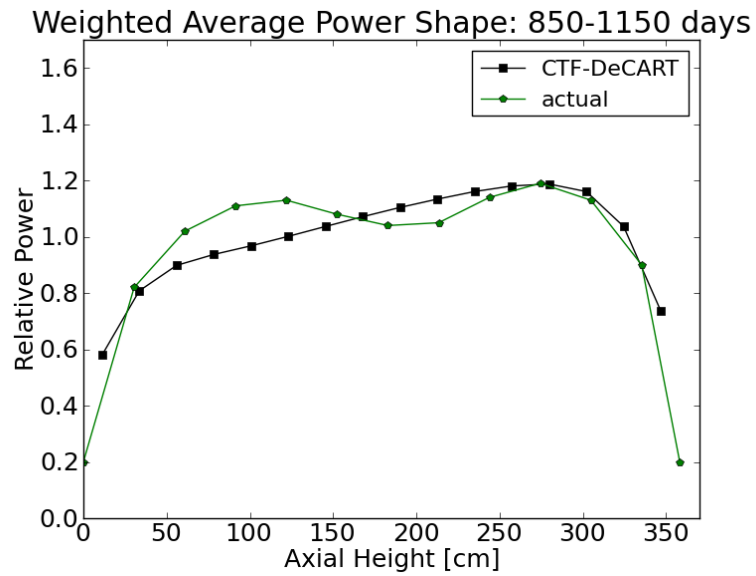


Figure C.37: CTF-DeCART vs Actual Axial Power Shape (850-1150 days) [6]

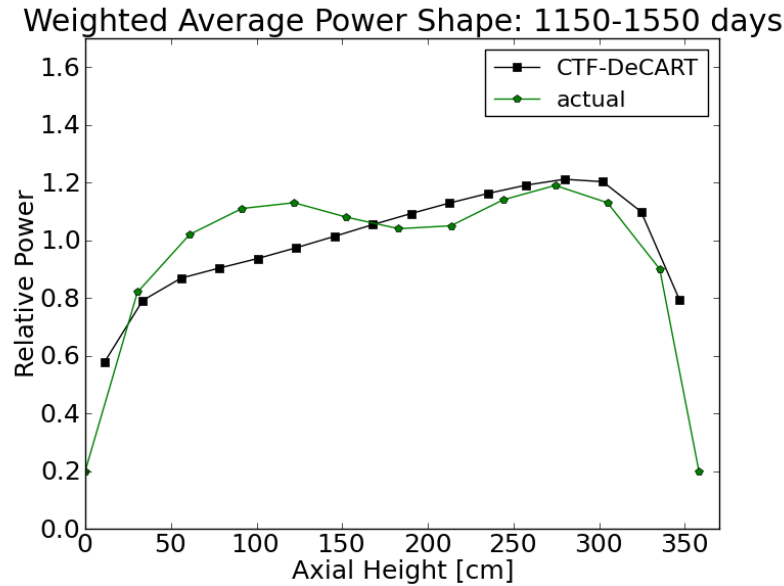
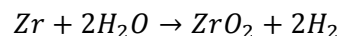


Figure C.38: CTF-DeCART vs Actual Axial Power Shape (1150-1550 days) [6]

Figure C.33 shows a significant bottom peak at the beginning of cycle for rod 15309. This is due to the higher moderation at lower axial levels in the BOC due to a higher flow area and a low initial temperature causing increased moderation as compared to a typical PWR fuel rod. However, the axial distribution can be seen to flatten out with time. The BOC power shape from CTF-DeCART matches well with the FRAPCON results, however, the axial power shapes for 295-600 days do not match the actual power shapes as well as the BOC. The FRAPCON results depress in the center where the CTF-DeCART results remain relatively flat. This could be due in part to the modeling of the rod. The FRAPCON results come from a 15x15 rod and there is flux variation from the surrounding environment. The CTF-DeCART model used reflective boundary conditions around a single rod giving it a more evenly distributed neutron flux. Later on in the cycle, the axial offset can be seen to switch to a top peaked system as would be expected with depletion in the bottom of the rod. Overall, the CTF-DeCART results compare well to the FRAPCON results and follow the expectations of the physical system.

## D. Hydrogen Background

Under normal reactor operating conditions, zirconium cladding is exposed to temperature ranges of 330 °C at the outer cladding surface and 380 °C at the inner cladding surface. The outer surface of the zirconium cladding is in contact with coolant. This interface interaction causes a corrosion reaction which generates hydrogen in the following manner:



D-1

Some of the hydrogen produced in the above reaction may be picked up by the cladding (approximately 10-20%) [9]. The corrosion reaction degrades the fuel cladding and creates zirconium oxide on the outer

surface of the cladding. A consequence of the formation of zirconium oxide is the decrease of heat transfer to the cooling water. Some other notable sources of hydrogen are hydrogen generated by radiolysis and hydrogen intentionally added to the coolant to limit oxidation [10].

## D.1. Hydrogen Diffusion

When hydrogen is picked up the cladding, the hydrogen in solid solution may diffuse via two mechanisms. Hydrogen can diffuse due to a temperature gradient, as described by the Soret Effect, or a concentration gradient, as described by Fick's Law. These gradients are described by the following equation [11]:

$$J_D = -D\nabla C_{ss} - Q^* \frac{DC_{ss}}{RT^2} \nabla T \quad D-2$$

Where,

$J_D$  is the diffusion flux

$C_{ss}$  is the concentration of hydrogen in solid solution

$R$  is the gas constant

$T$  is the temperature in kelvin

$Q^*$  is the heat of transport

$D$  is the diffusion coefficient, which is governed by an Arrhenius law:

$$D = A_D * \exp \left( -\frac{Q_D}{RT} \right) \quad D-3$$

The coefficients have been measured by Kearns [12]:

$$A_D = 7.90 * 10^{-7} m^2/s \quad D-4$$

$$Q_D = 4.49 * 10^4 J/mol \quad D-5$$

A concentration gradient in the hydrogen distribution generates a flux according to Fick's law.

$$J_{Fick} = -D\nabla C_{ss} \quad D-6$$

As more hydrogen is picked up into the cladding, the Fick's law term in equation D-2 means that the concentration gradient will drive the hydrogen from a region of high concentration to a region of low concentration. Since hydrogen is picked up at the outer cladding and coolant interface, the hydrogen will diffuse further into the cladding.

As observed by Sawatzky and confirmed in several studies, hydrogen diffusion is also driven by a temperature gradient. According to the linear thermodynamic model [13], there is a coupling between thermal diffusion and species diffusion. This phenomenon is called Soret effect (flux of particles induced by temperature gradient). A temperature gradient in the hydrogen distribution generates a flux according to the Soret Effect as seen in equation D-7.

$$J_{Soret} = -\frac{DC_{ss}Q^*}{RT^2}\nabla T \quad \text{D-7}$$

Radially, the fuel pellet generates heat while the coolant acts as a heat sink. This creates a radial temperature distribution. A temperature drop of approximately 30 °C is observed across the cladding [14]. The effect of this temperature distribution can be seen by the formation of a hydride rim near the cladding-coolant interface. Figure D.1 shows the radial hydrogen distribution and hydride rim.

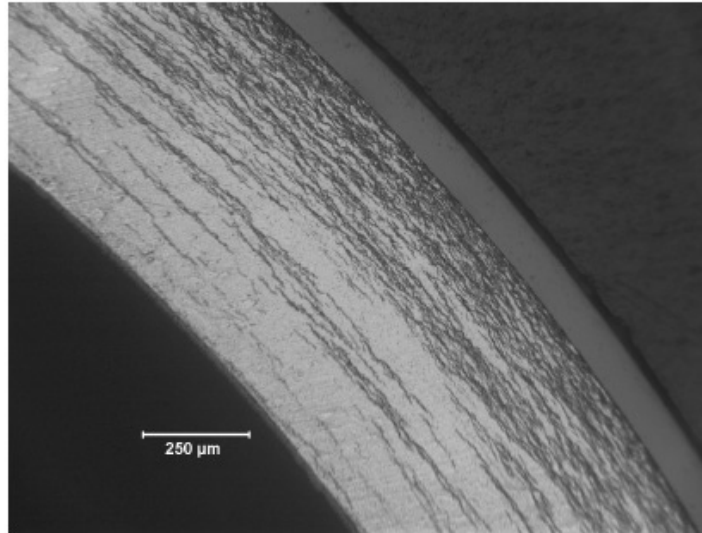


Figure D.1 Radial hydrogen distribution and hydride rim (740-wppm H) [14]

Axially, the coolant of a Pressurized Water Reactor (PWR) enters the core at a temperature of about 287 °C and exits at about 320 °C [15]. This axial temperature gradient in the coolant could tend to cause an axial temperature gradient within the cladding and the corrosion is higher in the upper spacer grids. Fuel pellets are manufactured with dishes and chamfers to allow space for fission gas release, thermal expansion and swelling. With less fuel and consequently less energy deposition, there is an axial temperature gradient along the inter-pellet gaps. Hydrogen diffuses towards the cold regions that the inter-pellet gaps create, however there are very few measurements of the axial distribution of hydrogen as a function of elevation [16].

Azimuthally, temperature gradients can be produced due to geometric heterogeneity in the fuel rod arrangement. An example of this geometry is a water rod placed next to a fuel rod, since in this case one side of the fuel rod is exposed to more moderation than the other side surrounded by fuel rods. This geometry would cause a temperature gradient for the hydrogen to follow. Other examples include replacing the water rod with a control rod, different locations within the assembly (edges, corners, near spacers, etc.) and defects in the cladding such as the spallation of oxide, which can all create heterogeneous temperature distributions that affect the hydrogen distribution.

## D.2. Hydrogen as hydrides

An understanding of the distribution of hydrogen in solid solution is necessary in order to study the formation of the specific hydride distribution. When the hydrogen content reaches the solubility limit in the  $\alpha$ -zirconium matrix, the hydrogen may precipitates as zirconium hydride or the hydrides may dissolve back into hydrogen in solid solution. These limits are called the Terminal Solid Solubility of precipitation and dissolution (TSSp and TSSd). The determination of the TSS is essential for a better understanding of the behavior of zirconium hydrides. According to McMinn [16] and without any additional effects, the TSSd and the TSSp can be approximated by the following equations:

$$\begin{cases} TSSd = 106446.7 * \exp\left(-\frac{4328.67}{T}\right) \\ TSSp = 138746.0 * \exp\left(-\frac{4145.72}{T}\right) \end{cases} \quad \text{D-8}$$

In addition to temperature, the main factors that influence hydride precipitation and dissolution in zirconium and its alloys are irradiation, oxygen in solid solution, alloying elements, and thermal cycles. These effects are not taken into account in the current model.

## D.3. Kinetics of precipitation

The kinetics of precipitation is a critical aspect of hydrogen redistribution in the cladding. While the TSSp and TSSd give the equilibrium value between the hydrogen in solid solution and in the precipitated hydrides, the kinetics provide information regarding the transient behavior between a non-equilibrated initial condition and the final steady state equilibrium. The detailed kinetics of hydride precipitation is likely one of the main causes of the rim feature and specific hydrogen distributions that occur in the nuclear fuel cladding.

In the case of reactor operation, the initial concentration of hydrogen starts at about 0 wt. ppm. The cladding is submitted to a temperature gradient of about 40°C for a thickness of 0.6 mm. The hydrogen flux is coming from the coolant interface, as shown below:

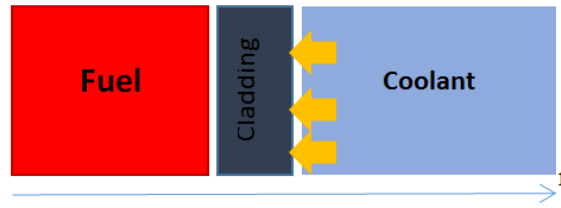


Figure D.2 Hydrogen boundary condition schematic

As noticed by Shewmon [17], it is impossible to predict the redistribution solely from the diffusion laws and the Terminal Solid Solubility. Indeed, as long as the hydrogen concentration does not reach the TSSp, the equilibrium will be established in a quasi-steady-state manner and the highest concentration of hydrogen will occur in the colder area, which is the coolant/cladding interface.

Moreover, the TSSp decreases when the temperature decreases. Therefore the lowest temperature area also has the lowest TSSp. Thus, the point where hydrogen reaches the TSSp first is at the cladding/coolant interface. If instantaneous precipitation is assumed, there is no reason for the hydrogen to diffuse into the cladding. It will precipitate instantaneously upon entry into the cladding. This would however lead to the formation of a solid hydride, and it is not what is observed [17]. Therefore, the role of precipitation kinetics needs to be examined. This precipitation will explain why hydrogen can diffuse into the cladding. If all the hydrogen in solid solution does not precipitate instantaneously, it remains supersaturated in the solid state. In that case, the previous diffusion equilibrium is modified and hydrogen diffuses toward the fuel/cladding interface.

Marino proposed a precipitation rate proportional to the difference between supersaturated hydrogen in solid solution concentration  $C_{ss}$  and the equilibrium value (given by the TSSp) [18,19]:

$$\left\{ \begin{array}{l} \frac{dC_p}{dt} = \alpha^2 (C_{ss} - TSSp) \\ \frac{dC_{ss}}{dt} = -\alpha^2 (C_{ss} - TSSp) \end{array} \right\} \quad \text{D-9}$$

Where,

$C_p$  is the Concentration of hydrogen as hydrides (wt.ppm)

$C_{ss}$  is the Concentration of hydrogen in solid solution (wt.ppm)

$\alpha^2$  is the precipitation rate constant

TSSp is the Terminal Solid Solubility limit of precipitation

The precipitation rate constant,  $\alpha^2$ , has been studied by Kammenzind, who measured it in his experiment and proposed an Arrhenius law to describe its dependence on temperature [20]. The equation found for the kinetics parameter is:

$$\alpha = A_\alpha * \exp\left(-\frac{Q_\alpha}{RT}\right) \quad \text{D-10}$$

Where,

R is the gas constant

T is the temperature in kelvin

$$A_{\alpha} \approx 62.3 \text{ s}^{1/2}$$

$$Q_{\alpha} \approx 4.12 * 10^4 \text{ J}$$

The precipitation rate constant was also studied within this project. This experiment is described in Section E.2.

## D.4. Hydrogen Model in Bison

In order to predict the distribution of hydrogen in solid solution and precipitated hydrides the temperature distribution must be well known. Due to the complexity of the reactor core geometry, it is not possible to have reliable analytical profiles of the temperature distribution. Moreover, the hydrogen model does not provide analytically solvable results when diffusion and precipitation of hydrogen occur simultaneously. For both of these reasons, the prediction of hydrogen distribution required the use of computer codes.

In order to predict the hydrogen distribution, a fuel performance code developed by Idaho National Laboratory called BISON [21]. In this project, a contribution to this computer code has been created in the form of the hydrogen model.

From the precipitation, dissolution and diffusion equations described in the previous sections, the balance equation for hydrogen in solid solution and hydride concentration can be deduced. The variation of hydrogen in solid solution per unit of time is given by the sum of the net flux, the hydrogen created by the dissolution of hydride minus the hydrogen transformed into hydride due to precipitation.

Recall the diffusion flux (Equation D-2), TSS (Equation D-8), and rate of precipitation and dissolution (Equation D-9):

$$J_D = -D \nabla C_{ss} - \frac{D C_{ss} Q^*}{R T^2} \nabla T \quad \text{D-2}$$

$$\begin{cases} TSSd \text{ (wt. ppm)} = 106446.7 * \exp\left(-\frac{4328.67}{T \text{ (K)}}\right) \\ TSSp \text{ (wt. ppm)} = 138746.0 * \exp\left(-\frac{4145.72}{T \text{ (K)}}\right) \end{cases} \quad \text{D-8}$$

$$\begin{cases} \frac{dC_p}{dt} = \alpha^2 (C_{ss} - TSSp) \\ \frac{dC_{ss}}{dt} = -\alpha^2 (C_{ss} - TSSp) \end{cases} \quad \text{D-9}$$



Four different cases have to be taken into account for the writing of the balance equations.

In the first case, the concentration of hydrogen in solid solution is greater than the TSSp. Then, precipitation occurs according to the laws described above.

- Precipitation:

$$\text{if } C_{ss} > TSSp, \left\{ \begin{array}{l} \frac{dC_{ss}}{dt} = -\nabla \cdot J - \alpha^2(C_{ss} - TSSp) \\ \frac{dC_p}{dt} = \alpha^2(C_{ss} - TSSp) \end{array} \right\} \quad \text{D-11}$$

In the second case, the concentration in solid solution is between the TSSd and the TSSp. This is the “hysteresis” area, where neither dissolution nor precipitation occurs.

- Hysteresis:

$$\text{if } TSSp \geq C_{ss} > TSSd, \left\{ \begin{array}{l} \frac{dC_{ss}}{dt} = -\nabla \cdot J \\ \frac{dC_p}{dt} = 0 \end{array} \right\} \quad \text{D-12}$$

In the third case, the concentration in solid solution is below the TSSd. The hydrogen in the precipitated hydrides ( $C_p$ ) is dissolving so that the  $C_{ss}$  matches the TSSd value. This is possible only if there are hydrides ( $C_p > 0$ ).

- Dissolution:

$$\text{if } TSSd \leq C_{ss} \text{ and } C_p > 0 \text{ and } \nabla J > 0, \left\{ \begin{array}{l} \frac{dC_{ss}}{dt} = -\nabla \cdot J + \beta^2(TSSd - C_{ss}) \\ \frac{dC_p}{dt} = -\beta^2(TSSd - C_{ss}) \end{array} \right\} \quad \text{D-13}$$

In the fourth and last case, the concentration in solid solution is below the TSSd but there are no more hydrides to dissolve. In that case, the only change to hydrogen concentration comes from net diffusion flux.

- Diffusion only:

$$\text{if } TSSd \geq C_{ss} \text{ and } C_p = 0, \left\{ \begin{array}{l} \frac{dC_{ss}}{dt} = -\nabla \cdot J \\ \frac{dC_p}{dt} = 0 \end{array} \right\} \quad \text{D-14}$$

The model constants have been taken from the literature and are summarized in Table D.1.

Table D.1: Hydrogen model constants

Phenomenon	Parameter	Value	Unit	Source	Comments
Fick's law	$A_{\text{Diff}}$	$7.90 \cdot 10^{-7}$	$\text{m}^2/\text{s}$	[22]	Longitudinal diffusion
	$Q_{\text{Diff}}$	$4.49 \cdot 10^4$	J/mol	[22]	Longitudinal diffusion
Soret effect	$Q^*$	$2.51 \cdot 10^4$	J/mol/K	[20]	Average value
Precipitation	$A_{\text{P}}$	$1.39 \cdot 10^5$	wt. ppm	[23]	Unirradiated
	$Q_{\text{P}}$	$3.45 \cdot 10^4$	J/mol	[23]	Unirradiated
Dissolution	$A_{\text{D}}$	$1.06 \cdot 10^5$	wt. ppm	[23]	Unirradiated
	$Q_{\text{D}}$	$3.60 \cdot 10^4$	J/mol	[23]	Unirradiated
Precipitation kinetics	$A_{\alpha}$	$6.23 \cdot 10^1$	$\text{s}^{1/2}$	[20]	
	$Q_{\alpha}$	$4.12 \cdot 10^4$	J/mol	[23]	

## D.5. Implementation of the model in the 3D fuel performance code BISON

The temperature in the core is heterogeneous not only along the axial direction, but also along the radial and azimuthal directions. Because of this, a 3D computer code (BISON) has been developed by Idaho National Laboratory. This code is based on the framework MOOSE [24]. BISON provides accurate 3D temperature distributions in the fuel and in the cladding. Thanks to the modularity of these codes, it has also been possible to implement the hydrogen model into it, and thus to obtain 2D and 3D hydrogen distribution evolution. MOOSE, Multiphysics Object Oriented Simulation Environment, is a framework for solving computational engineering problems in a well-managed and coordinated manner [24].

BISON is used primarily for analysis of  $\text{UO}_2$  fuel, but has also been used to model TRISO fuel and rod and plate metal fuel [25]. Since it is based on MOOSE, it is also an implicit and fully coupled core, capable of running in parallel. It uses the library from ELK (mechanical properties) and FOX (materials properties).

As stated above, because of its modularity, it is possible to implement new models and equations into BISON. However, a transformation of the equations is necessary. Since BISON is based on the Galerkin Finite Element theory, the equation has to be transformed into their weak form [26]. The weak form corresponds to the scalar product (in the function space) of the equation and a given shape function:

$$\text{WeakForm}(f) = (f, \psi) = \iiint_V f(x, y, z) \cdot \psi_i(x, y, z) dV \quad \text{D-15}$$

The function scalar product is represented by  $(f, g)$ , where  $f$  and  $g$  are space and time dependent functions. In the case of the second derivative, the weak form requires integration by parts, to remove the second order derivative. Once the weak form of an entire equation is obtained, each term is considered individually. This piece of the equation (in its weak form) is called a Kernel, and it is what has to be implemented in the code.

In order to evaluate the convergence of the code toward a solution (through iteration), MOOSE uses a mathematical tool called the Free Jacobian Newton Krylov. This is considerably faster than the calculation of the residuals of each variable. This Jacobian has to be calculated for each kernel, and is obtained by calculating the derivative of the kernel weak form with respect to the primary variable [24].

The following kernels were created: Diffusion (only for hydrogen in solid solution), Precipitation/Dissolution for hydrogen in solid solution, Precipitation/Dissolution for precipitated hydrides, Time derivative (Implemented in MOOSE). The source code for these can be found in Olivier Courty's Thesis [46].

## **E. Hydrogen Experiment**

This section describes two experiments which were set up and performed in order to measure the data regarding two empirical constants: the heat of transport and the rate of precipitation.

### **E.1. Measurement of the heat of transport $Q^*$**

Previous measurements of the heat of transport ( $Q^*$ ), for hydrogen in Zircaloy-4, show significant dispersion among measured values. These measurements were gathered and presented by Menibus in his thesis [27], and his table is reproduced in Table E-1. Figure E.1 shows the average value of each experiment against the temperature range that is used. All the measurements follow similar procedures. A zirconium (or Zircaloy) plate is initially charged with hydrogen. Then the plate is submitted to a constant temperature gradient over a long time period. At the end of the experiment, the hydrogen distribution is assumed to have a steady state profile.

Table E.1 Summary of heat of transport of hydrogen in Zircaloy measurements

Material	Temperature (°C)	H (wt.ppm)	Q* (kJ/mol)	# of exp.	Source	$\Delta T / \Delta x$ (°C/cm)
Zr- $\alpha$	300-500	60	$24.7 \pm 0.6$	2	Sawatzky [11]	167
	350-400	<55	$29.5 \pm 0.7$	2	Sugiaski [28]	n/a
	200-480	10	22.2	1	Morozumi [29]	175
	350-560	55	$11 + 0.026 T$	11	Hashizume [30]	137, 150
Zircaloy-2	295-450	300	14.2	1	Markowitz [31]	n/a
	300-500	60	$22.6 \pm 4.2$	2	Sawatzky [32]	167
Zircaloy-4	260-648	46-250	$26.9 \pm 5.4$	11	Kammenzind [20]	66, 87
	300-340	60	28.1	1	Hong[33]	13
Zr- $\alpha$ -1%Nb	200-480	10	24.7	1	Morozumi[29]	175
Zr- $\alpha$ -2.6%Nb	300-500	68	$23.4 \pm 1.8$	2	Sawatzky[11]	163
Zr- $\alpha$ -2.5%Nb	240-500	28-108	$19.3 \pm 1.8$	8	Jovanovic [34]	43, 47, 50
Zircaloy-2 / Deuterium	300-500	120	$27.2 \pm 1.8$	2	Sawatzky [11]	133
Zr-Tritium	250-350	<55	$24.3 \pm 2$	3	Sugiaski [28]	n/a

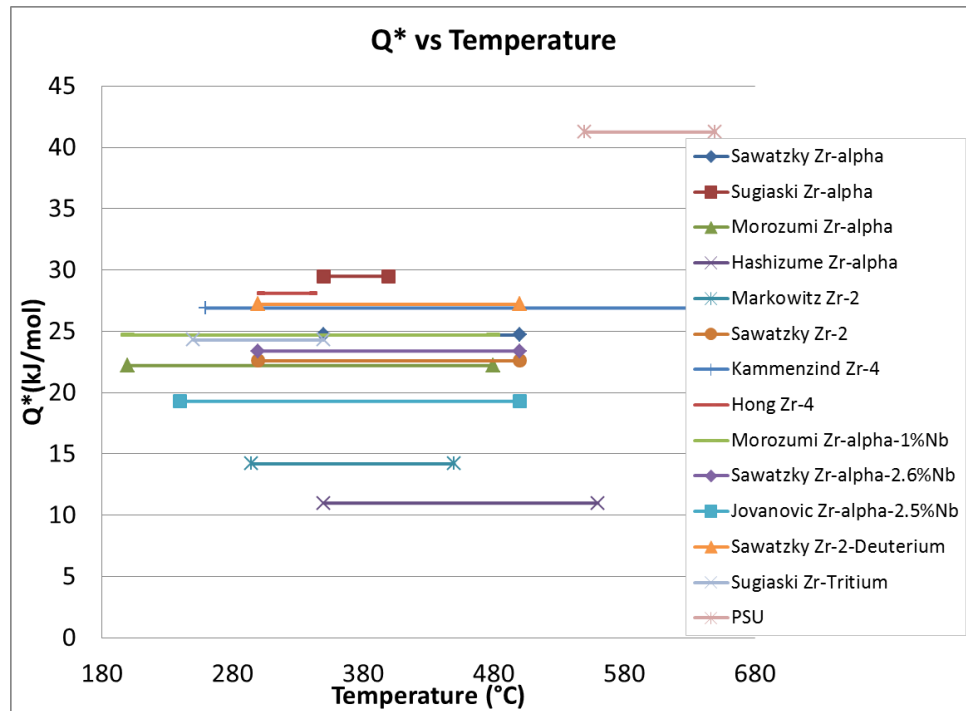


Figure E.1 Measurement of  $Q^*$  with respect to the temperature

Only two studies are devoted to Zircaloy-4. The Kammenzind's study shows a variation of the heat of transport with the temperature, but also with the gradient applied. However, no clear law seems to be deducible from his measurements [35]. Figure E.2 shows the measured values of  $Q^*$  versus the inverse of the absolute temperature. Kammenzind's experimental results show a high dispersion. Since this parameter is critical in the diffusion model and that it cannot be calculated, an experiment was designed to measure the value of  $Q^*$ .

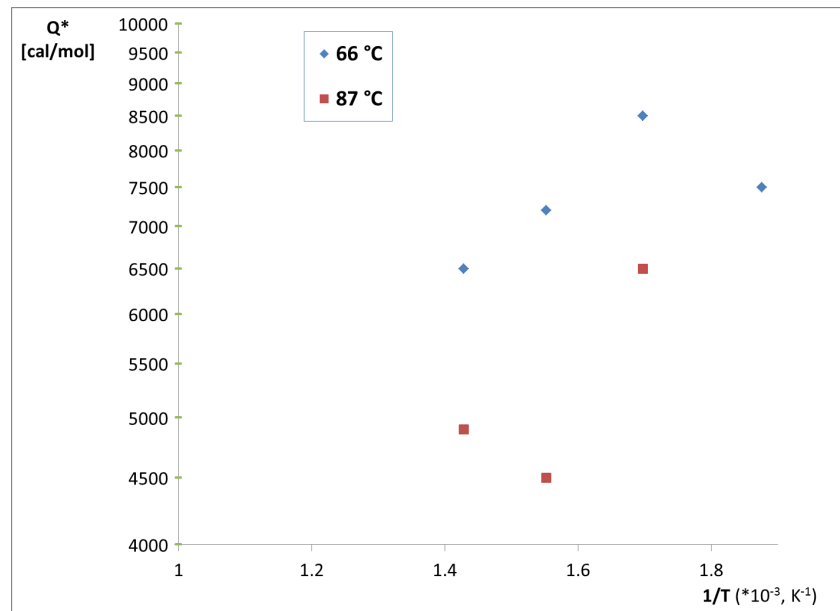


Figure E.2: Heat of transport measured by Kammenzind

### E.1.1 Experimental design for measurement of $Q^*$

The experiment was designed, with the help of Daniel Nunez, to observe the redistribution of hydrogen under a temperature gradient in the absence of precipitation. In this case, the steady state equilibrium hydrogen concentration in solid solution is given by:

$$C_{ss}(x) = C_0 * \exp\left(\frac{Q^*}{RT}\right) \quad \text{E-1}$$

The sample chosen for the study is a Zircaloy-4 plate, measuring 1cm x 3.4cm x 0.06cm. The sample is stacked between two stainless steel holders, as shown in Figure E.3.

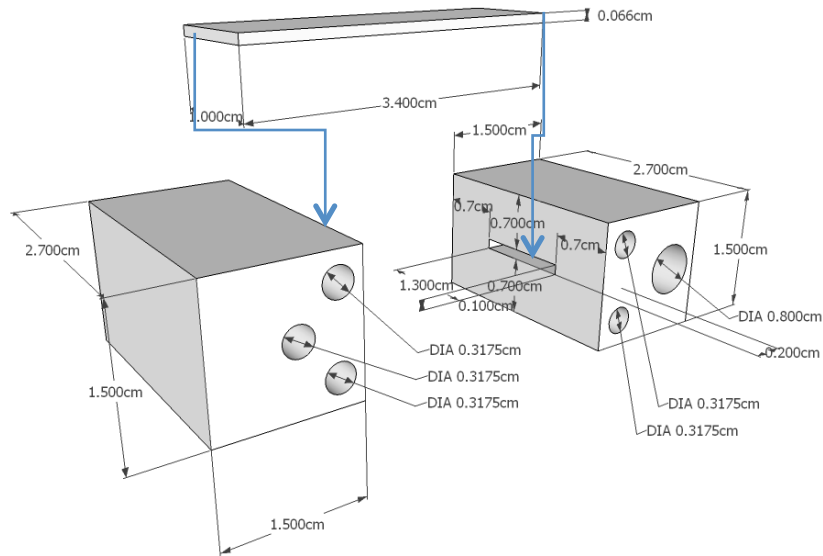


Figure E.3: 3-D View of the 304 Stainless Steel holders and the Zircaloy-4 plate sample

The holder with 3 small holes is heated to the higher temperature and the second one is one heated to a lower temperature. The plate is inserted about 2 mm into the slot in each holder, which means that the experimentally usable section of the sample is 3 cm long. The holders were heated with silicon carbide surface igniters [36]. These igniters can reach a temperature greater than 1000°C, and allow obtaining high temperatures in a localized spot. The igniters are placed on the outside of the holders, as shown in Figure E.4.

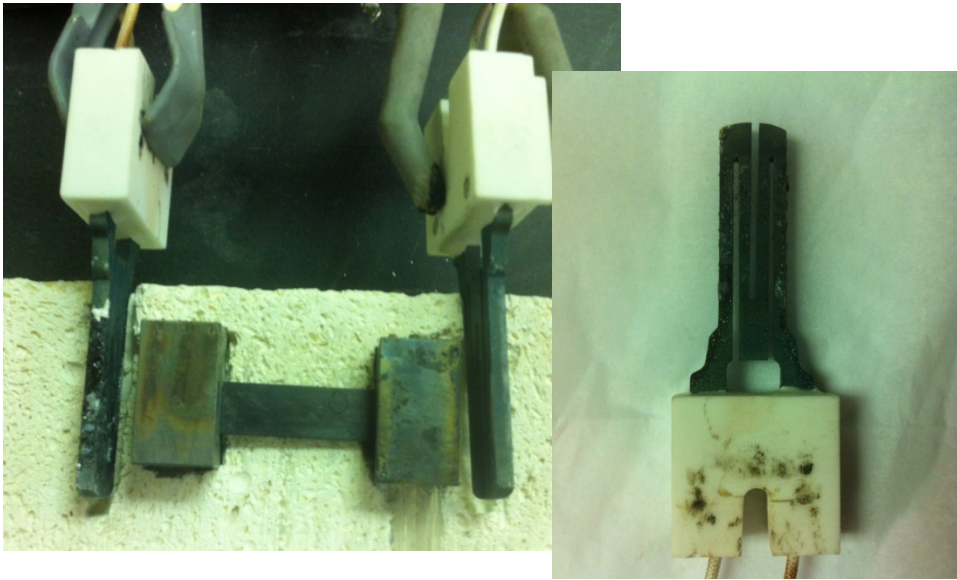


Figure E.4: Heaters, holders and sample in the heat of transport experiment

sed throughout the experiment.

Table E.2 below shows the main specifications of the controllers used throughout the experiment.

Table E.2: Temperature controller Specifications

Specification	Value
<b>Resolution:</b>	1°/0.1°; 10 $\mu$ V process
<b>Temperature Stability:</b>	RTD: 0.04°C/°C
<b>Reading Rate:</b>	3 samples per second
<b>Display:</b>	4-digit, 9-segment LED;
<b>Input Types</b>	Thermocouple, RTD, analog voltage, analog current
<b>Thermocouple Lead Resistance</b>	100 $\Omega$ (max)
<b>Digital Filter:</b>	Programmable

These controllers are configured in a Proportional-Integral-Derivative mode. The controlled temperature is given by a type-K thermocouple, attached to the extremity of the plate (But not in the holder). Figure E.5 shows the control loop pattern.

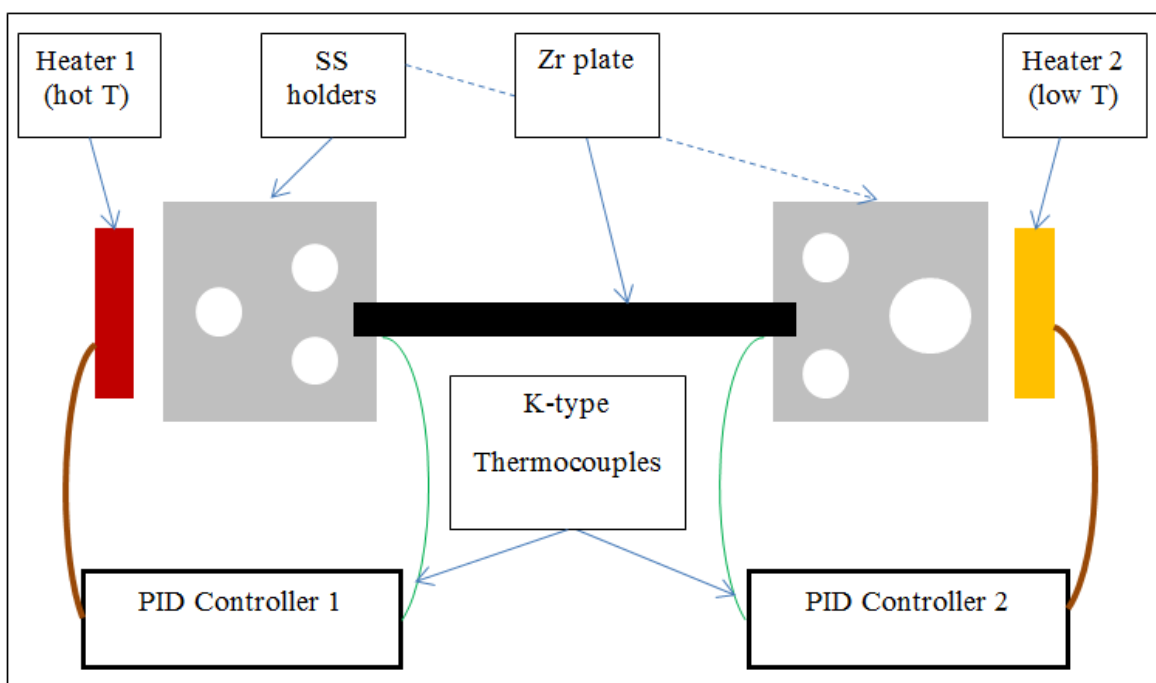


Figure E.5: Schematic of the temperature control for the diffusion experiment

The PID values have been chosen using a manual configuration. Table E.3 reproduces the values chosen.

Table E.3: PID values of the thermal controllers

Parameter	PID controller 1	PID controller 2
P	50	300
I	100	150
D	6.0	25

Since there is heat transfer from the hot side to the cool side of the plate, a thermal flux is created toward the “cool” holder, where the heat is removed using an air cooling system connected to this holder. The air flow is controlled by a regulator. Air is blown through a glass tube into the main hole of the second holder. However, due to heat loss caused by natural convection, this system is not used in most of the experiments.

In order to minimize heat losses, two different types of insulation have been installed. First, the entire setup (holder, heating elements, sample and thermocouples) is contained within two insulating bricks. Second, insulation blankets are used to wrap the sample to provide additional thermal insulation. The design of the insulation is shown in Figure E.6. A second brick covers the experiment.



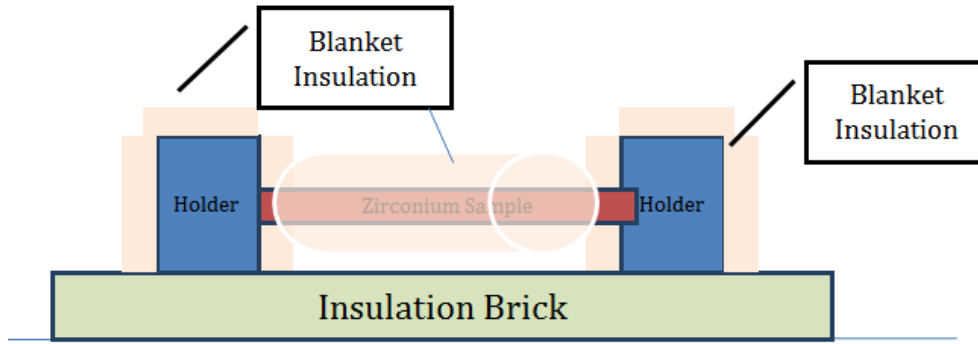


Figure E.6: Design of the insulation of the experiment

Once the second brick covers the experimental set up and the specimen is at temperature, the temperature measured outside of the experimental setting is smaller than 25 °C (for a room temperature of 20°C). This indicates a small heat loss and good thermal insulation.

The temperature profile was measured nonlinear in the sample, using a thermocouple in the middle of the plate. This indicates the presence of temperature losses. After several attempts, it was not possible to obtain a linear gradient. Nevertheless, the steady state hydrogen concentration profile is expressed as a function of temperature. Therefore, by knowing the temperature profile, the hydrogen concentration profile can be calculated. In order to accurately obtain the steady state temperature profile, 5 thermocouples have been attached to the plate, as shown in Figure E.7.

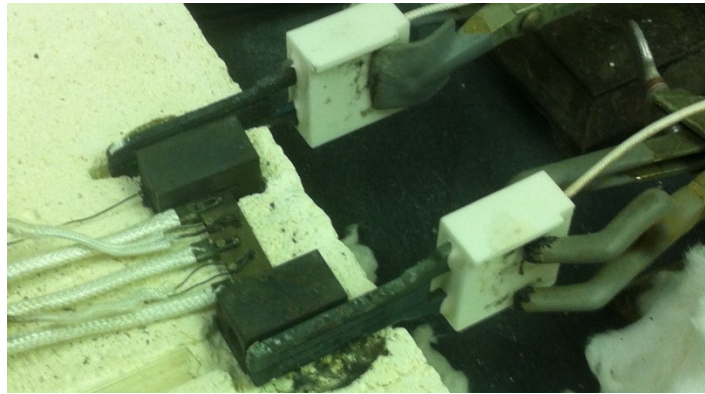


Figure E.7: Thermocouples on the sample

### E.1.2 Experimental procedure

The experiment was run with a temperature gradient of 550°C-650°C. In this case, the initial hydrogen concentration has to be 650 wt. ppm in order to prevent hydride precipitation. The hydrogen concentration has been measured after the charging and was equal to 709 wt.ppm. Therefore, the temperatures conditions were moved to 660°C-560°C to avoid precipitation. During preliminary tests, the temperature profile has been measured to estimate the heat loss. Assuming a constant linear heat loss, and using a sample length  $l=3$  cm,

$$T(x) = \frac{q}{2k} * x^2 - \frac{q}{2k} l * x + T_{maxi} \quad \text{E-2}$$

Where,

$q$  is the linear heat loss,

$k$  is the thermal conductivity

$T_{\max i}$  is the temperature at the hot end

It has been determined experimentally that  $\frac{q}{2k} = 27K.cm^{-2}$ .

The steady state hydrogen profile (and the TSSp) obtained for this temperature profile are given in Figure E.8. The steady state profile confirms the fact that there should not be any precipitation. In order to perform the calculation, the value heat of transport was assumed equal to  $2.51 \times 10^4 J/mol$ . This average value comes from Kammenzind work [37].

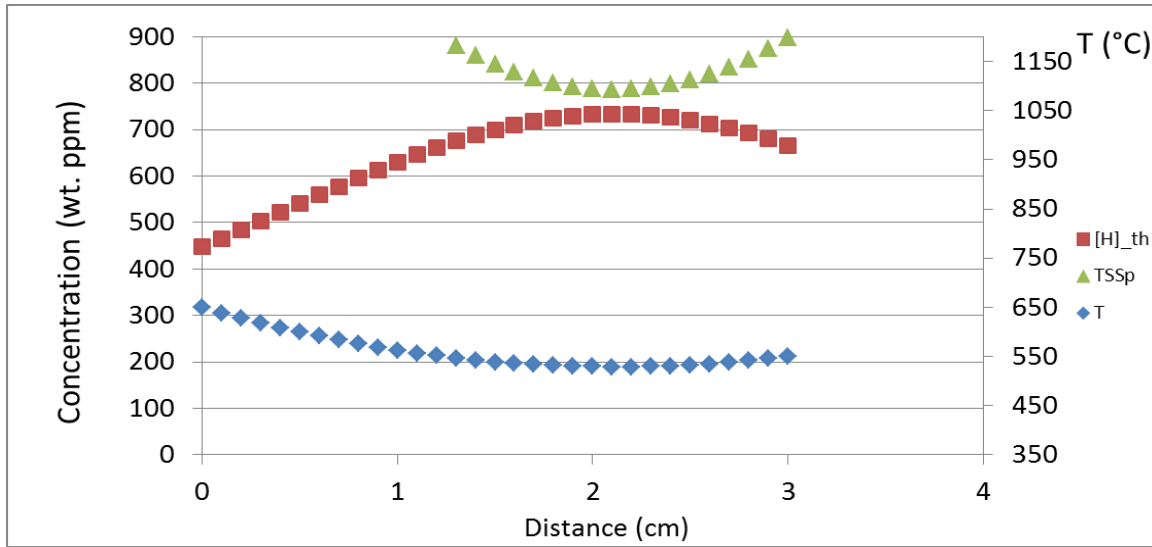


Figure E.8: Temperature and hydrogen steady state profile under 650°-550° gradient

To perform the experiment, dissolution of all the hydrides is required. To dissolve the hydrides, it is necessary to heat up the sample to a temperature higher than the dissolution TSS (TSSd) in the sample before applying the temperature gradient. Assuming the same quadratic profile, a temperature of 680°C applied at each side of the sample is necessary. According to a steady state calculation, the application of this temperature to the sample implies a full dissolution of the hydrogen, as shown in Figure E.9.

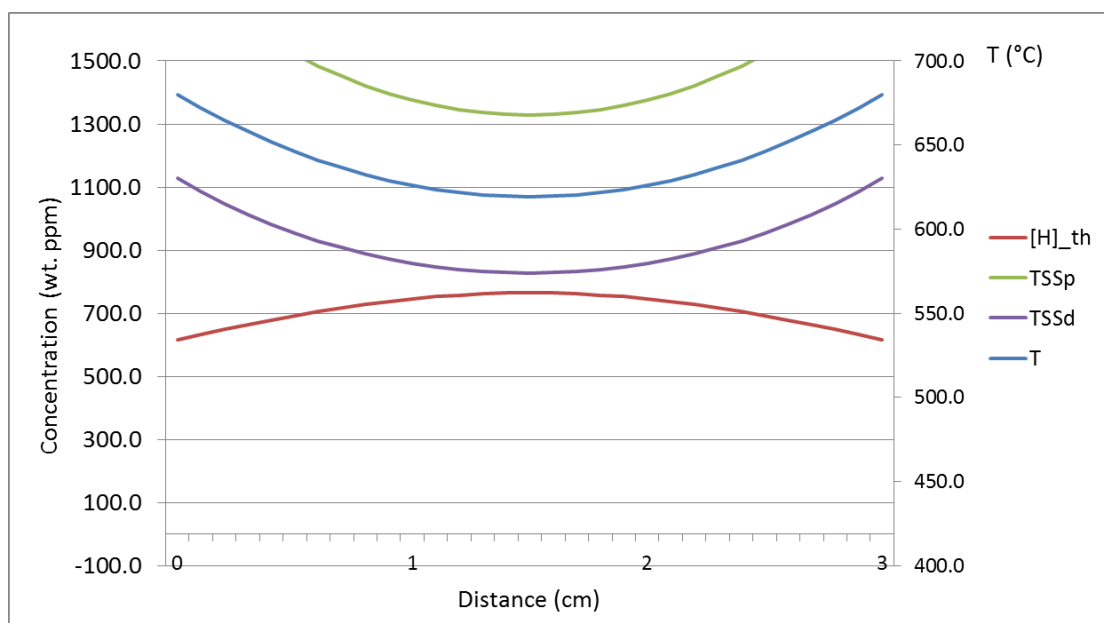


Figure E.9: Hydrogen profile before starting 660°C-560°C gradient experiment

After the dissolution step, the 560°C-660°C gradient has been applied. The transient profiles are represented on Figure E.10 and Figure E.11 for hydrogen in solid solution and hydrides respectively. Each line represents 10 hours. Table E.4 shows a numerical estimation of the difference between the steady state profile and each transient profile, by calculating the maximum, minimum and average difference of the 200 mesh points. Considering that the uncertainty of the hydrogen measurement is 20 wt.ppm, it can be concluded that after 60 hours, the transient is sufficiently close to the steady state (with a difference of about 5 wt. ppm).

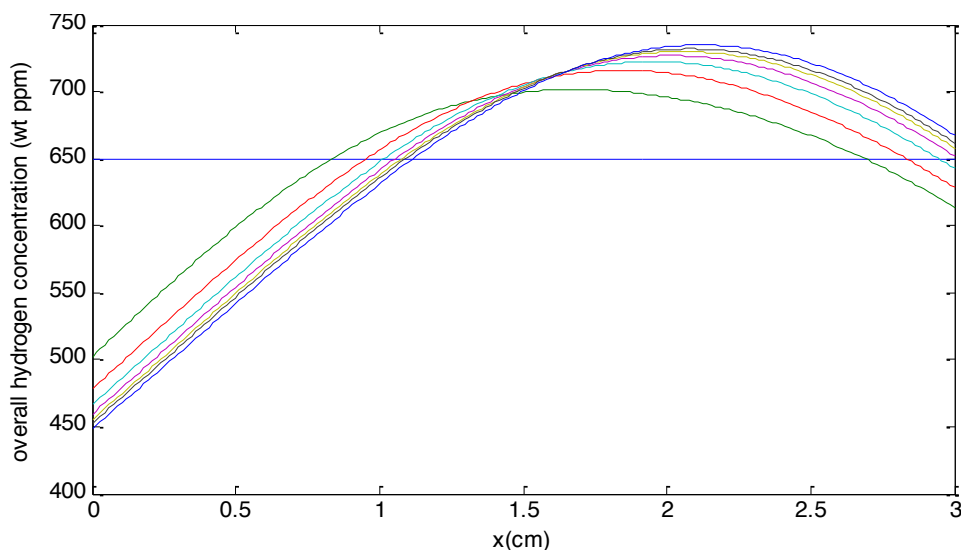


Figure E.10: Kinetics of the concentration profile (one line per 10 hours) with a 650°-550°C gradient

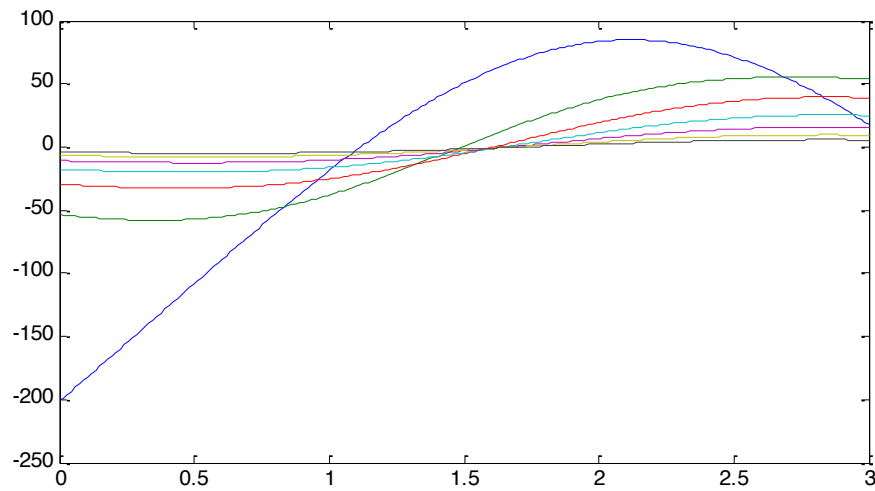


Figure E.11: Difference with steady state (one line per 10 hours) with a 650°C-550°C gradient

Table E.4: Estimators of the difference between transient and steady state profile (650°C-550°C)

time (h)	average difference with SS	maximum difference with steady state	minimum difference with steady state	standard deviation
0.0	198.8	84.8	-200.6	86.3
10.0	53.9	55.5	-58.0	44.9
20.0	29.6	39.5	-32.6	27.9
30.0	17.8	25.3	-19.9	17.4
40.0	10.9	15.7	-12.4	10.8
50.0	6.7	9.6	-7.8	6.7
60.0	4.1	5.7	-4.9	4.1

Figure E.12 shows the sample after 60 hours. There is some oxidation on the surface, but it is mostly a black protective layer. After measurement of the oxygen content, the oxide layer is thinner than 20 microns.



Figure E.12: Sample after 560°C-660°C experiment

### E.1.3 Results of the heat of transport experiment

The temperature profile has been measured during the experiment at five different locations on the plate. The temperature was measured constant during the 60 hours of the experiment. Table E.5 provides the temperatures and the locations of these thermocouples. The length of the sample in which analysis is judged to be reliable, goes from the first to the last thermocouple, which corresponds to a length of 2.6 cm

Table E.5: Temperature in the plate during the diffusion experiment

Location of the thermocouple	Temperature (°C)
0.4	550
1	567
1.7	581.5
2.4	607
3	660

This temperature profile cannot be estimated with the simplified profile described by equation E-2. The heat losses are modeled with by convective heat transfer with the air. The equation E-3 describes the steady state equilibrium.

$$k\nabla^2 T + \frac{2 \cdot h}{l_{Zr}} (T - T_{air}) = 0 \quad \text{E-3}$$

Where,

k is the conductivity of the Zircaloy-4

$l_{Zr}$  is the length of the plate

h the heat transfer coefficient for Zircaloy in air

$T_{air}$  the temperature of the air

Equation E-3 has for solution:

$$T(x) - T_{cool} = (T_{cool} - T_{air}) \cdot \cosh\left(\frac{x}{\sqrt{\frac{2 \cdot h}{l_{Zr}}}}\right) + \left[ T_{hot} - T_{air} - (T_{cool} - T_{air}) * \coth\left(\frac{2.6}{\sqrt{\frac{2 \cdot h}{l_{Zr}}}}\right) \right] \cdot \sinh\left(\frac{x}{\sqrt{\frac{2 \cdot h}{l_{Zr}}}}\right) \quad \text{E-4}$$

The temperature of the air is assumed to be equal to the temperature of the coolest side. The h is assumed to be equal to  $45 \text{ K}^{-1}$  and the conductivity is  $2100 \text{ m/K}$ . Figure E.12 shows the calculated profiles and the measured thermocouple data points, showing that the temperature model given by equation E-3 provides a good estimate of the actual temperature profile.

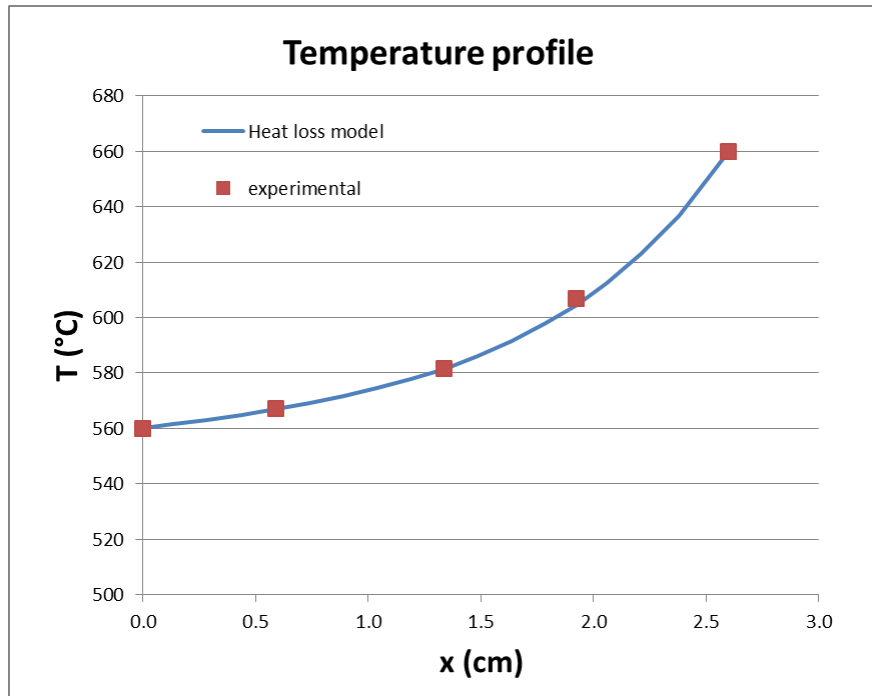


Figure E.13: Temperature profile for diffusion experiment

Subsequent to the experiment, the plate was cut into small samples 1.5 mm wide, and the hydrogen measured in each slice using hot vacuum extraction (performed by Luvak company) [38]. Figure E.14 shows the natural logarithm of the concentration (multiplied by the gas constant  $R$ ) as a function of the inverse of temperature. The slope of the curve is  $Q^*$  in J/mol.

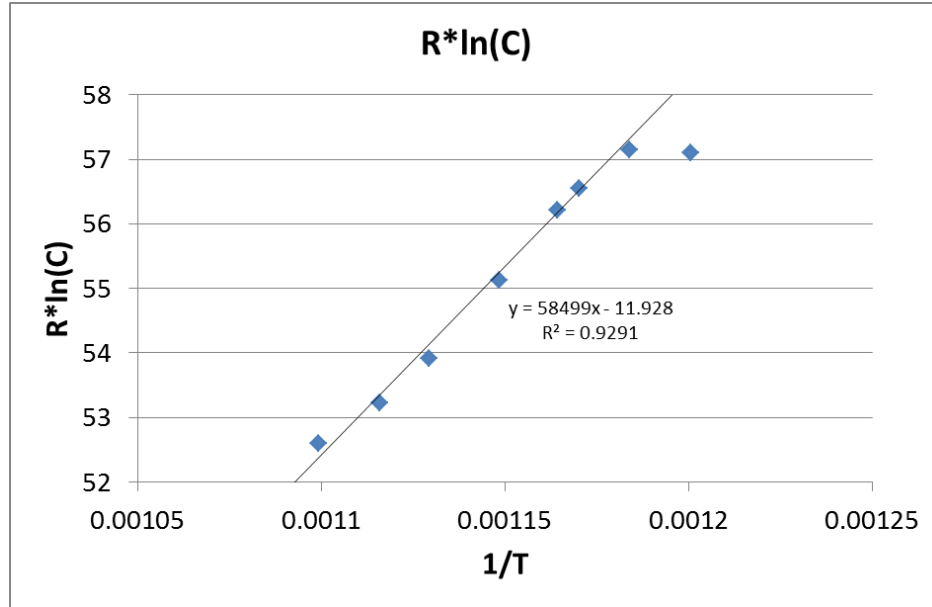


Figure E.14: Result of the diffusion experiment

The value find for  $Q^*$  is 58.50 kJ/mol.

#### E.1.4 Conclusion of the results of the $Q^*$ measurement

The value for  $Q^*$  found in this work is higher than Kammenzind's measurements. The order of magnitude is comparable, as shown in Figure E.15. Considering Kammenzind data, it is possible that the value of the temperature gradient has an impact on the value of  $Q^*$ . This trend seems to be confirmed by the measurement made during this work. The temperature gradient was 38°C/cm, which is significantly lower than Kammenzind's data. However, the comparison of all the measurements versus the temperature gradient, as shown in Figure E.16, does not confirm such a trend. This result should be confirmed with other temperature gradient in order to validate or not the conjecture. If the value of  $Q^*$  is dependent on the temperature gradient, the model of the Soret effect should be modified.

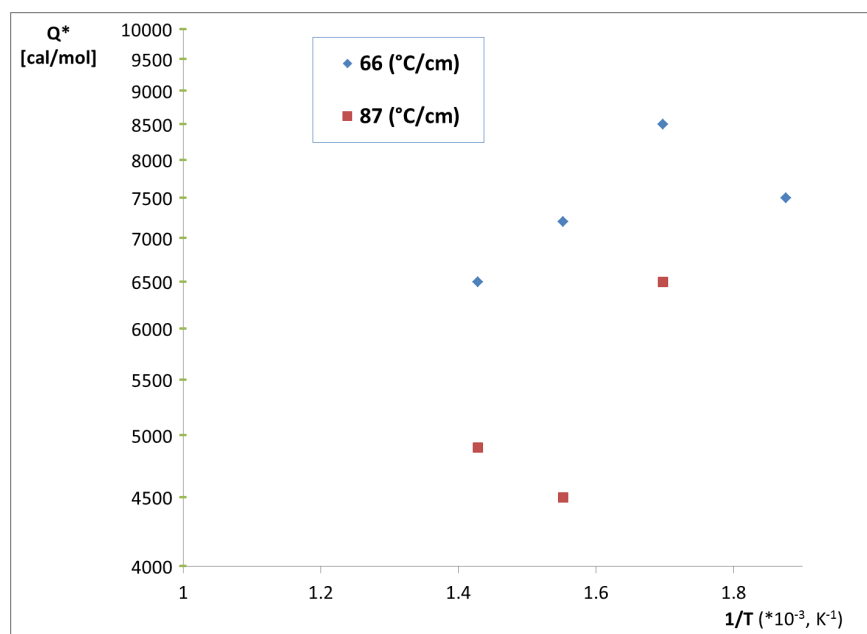


Figure E.15: Comparison of experimental results with Kammenzind's data [20]

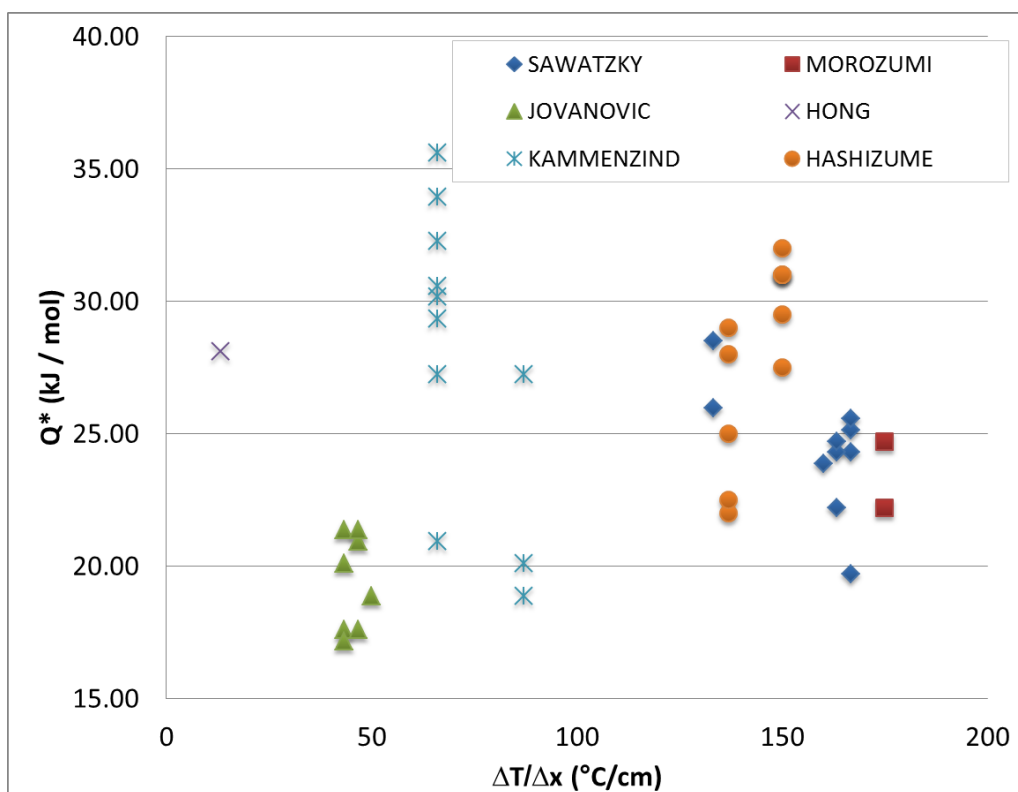


Figure E.16: Heat of transport  $Q^*$  measured in the literature as a function of the temperature gradient



## E.2. Measurement of the rate of precipitation

The rate of hydride precipitation in Zr alloys has been poorly studied. Except for Kammenzind's measurements and his Arrhenius law correlation, no extensive study has been performed to measure this rate. The main difficulty in the calculation of rate of precipitation is that it contains kinetic parameters, and therefore has to be studied in-situ. Zanellato and al., have measured the precipitation kinetics at 400°C, using a similar technique to the one used in the experiment presented below. They found a precipitation rate value of  $\alpha^2 = 0.012s^{-1}$  [39].

### E.2.1 Experimental technique

The technique used in this study is synchrotron radiation X-Ray diffraction at the Advanced Photon Source (APS) at Argonne National Laboratory (Argonne, Ill). X-Ray diffraction is the process of the coherent scattering of an X-Ray beam by planes of atoms in a crystal and is governed by Bragg's law [40, 41]:

$$\lambda = 2 d \sin(\theta) \quad \text{E-5}$$

Where,

$\lambda$  is the wavelength of the x-ray beam (m)

$d$  is the inter-planar spacing of the atoms (m)

$\theta$  is the diffraction angle (radians)

The quality of X-Ray diffraction data is directly related to the quality of the X-Ray source used. In this study, the X-Ray source is the APS synchrotron. The APS is a third generation synchrotron which produces X-rays at a very high brilliance which allows enhanced resolution and high energy radiation compared to conventional laboratory X-ray sources such as Cu-K $\alpha$  for example. The brilliance is a measure of the intensity (photons per second per unit area) and directionality of the X-ray beam through its divergence (milliradians squared). The brilliance of the APS is 6 to 10 orders of magnitude higher than that of a conventional X-Ray source such as Cu-K $\alpha$  [42]. This very high brilliance allows quick acquisition of data, high resolution and low background. This enables the detection of small volume fractions of phases that would otherwise not be detected. In addition, the high photon flux can be produced over a wide range of energies. This enables either the use of a monochromatic beam with a high and well known energy for our material or the use of a polychromatic beam.

Beamline 1-ID was used for this experiment because of the unique capability to operate at very high photon energies (more than 80 keV) allowing X-Rays to penetrate through the sample, while operating in transmission X-Ray diffraction. This allows data to be averaged over the full sample thickness which provides very good statistics. This beamline is also equipped with a fast amorphous silicon GE detector that allows very fast data collection rates. The beam is focused to a rectangular shape with slits which can be as small as 50 x 50  $\mu\text{m}$  [43]. The 1-ID allows the full diffraction rings to be recorded, which helps reveal in-plane texture.

## E.2.2 Experimental procedures

### a) Sample Preparation

One of the advantages of the 1-ID beamline is that very little sample preparation is needed in order to obtain reliable X-Ray diffraction data. Since the high energy X-Rays penetrate through the entire sample thickness, no particular surface preparation is needed, although having two parallel surfaces through the sample thickness simplifies the calculation of sample to detector distance. The only requirement is to allow full transmission of X-Rays through the sample. In the case of zirconium atoms probed by 80 keV X-Rays, a maximum thickness of 2 mm is allowed for the samples.

### b) Calibration

A calibration sample of an APS ceria powder is run at the beginning of every experiment in order to measure the exact beam position, angle and sample-to-detector distance. The X-Ray diffraction data from this sample is fitted, and the results of the fit are used to measure the volume fraction of hydrides in the zirconium matrix.

### c) Data Acquisition

The data is acquired on a large two-dimensional plate detector that allows the recording of the full diffraction ring. The detector recording area is 2048 x 2048 pixels big with each pixel measuring 200 x 200  $\mu\text{m}$ , which gives an angular resolution of  $4.6 \times 10^{-3}^\circ$  with our typical set-up. In the experiments performed at beamline 1-ID, continuous recording of data was performed while heating and cooling of samples under load. This allowed studying the kinetics of hydride precipitation *in situ*. One diffraction frame was recorded as ten consecutive images with a typical exposure time of 1 second (to avoid saturation of the detector). While recording data, the temperature and load were monitored and recorded by control computers.

### d) Data Analysis

Several steps were needed to analyze the raw two-dimensional diffraction frames. The ten images recorded for one frame were summed and averaged by a Matlab® routine developed by J. Almer [43] and the background was subtracted, as described below. Using the Matlab® routine, full diffraction rings were integrated over the whole azimuth ( $360^\circ$ ). The integration files obtained were then reduced to a one dimensional GSAS file by the Matlab® routine as illustrated in Figure E.19. The GSAS peaks obtained were then analyzed using GSAS/Rawplot® [44]. This software program is primarily a Rietveld refinement program that can fit all the different parameters that would affect peak height, shape and position (these parameters can be sample characteristics such as composition, crystal structure, atom positions, etc. or exterior parameters such as sample-to-detector distance, temperature, pressure, etc). However GSAS also allows a faster refinement by only fitting the peak shape, position and intensity of the raw data in a sub routine called Rawplot. For our peak fitting, the precision and amount of information given by Rawplot were sufficient. The peaks are fitted to a pseudo-Voigt function which is a convolution of Gaussian and Lorentzian peak shapes. Only the Gaussian full-width at half-maximum (FWHM) was fitted while the Lorentzian FWHM remained constant; this Gaussian FWHM gives an understanding of the sample contribution to broadening. The background was modeled using a third-degree polynomial function and several refinement steps were iterated (usually 10 successive refinements

for each parameter we chose to refine). This allowed us to fit the diffraction peaks and obtain (i) the integrated intensity, (ii) the Gaussian full width at half maximum (FWHM), (iii) the peak positions for the desired peaks. Additional details on the data analysis procedure can be found in Kimberly Colas thesis [45].

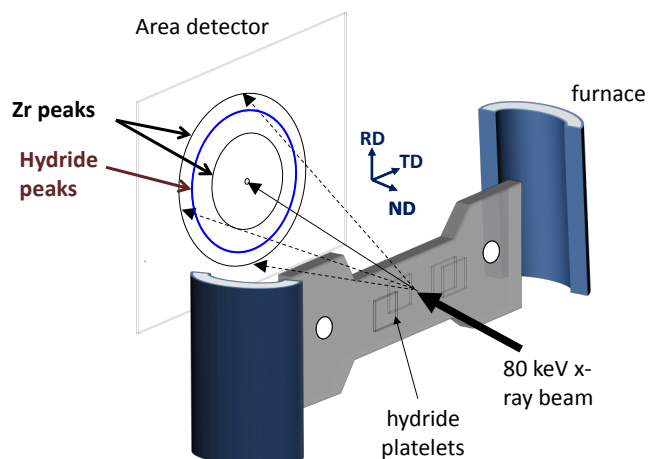


Figure E.17: Schematic representation of beamline 1-ID experimental set-up.

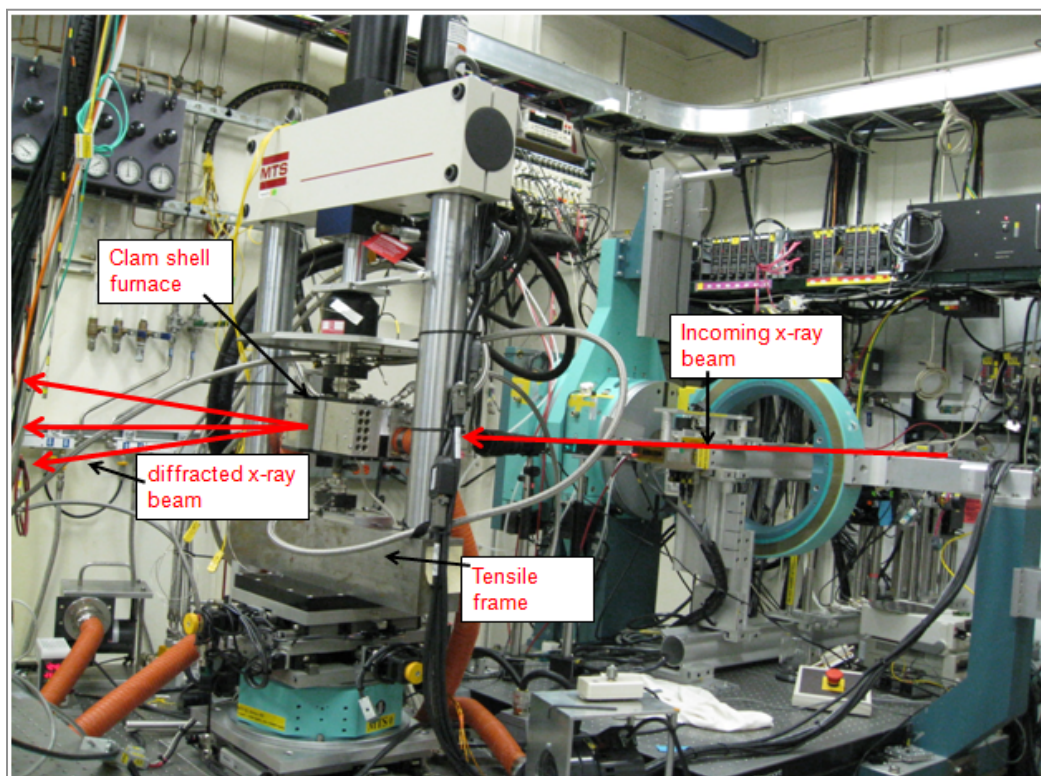


Figure E.18: Picture of the experimental set-up at beamline 1-ID.

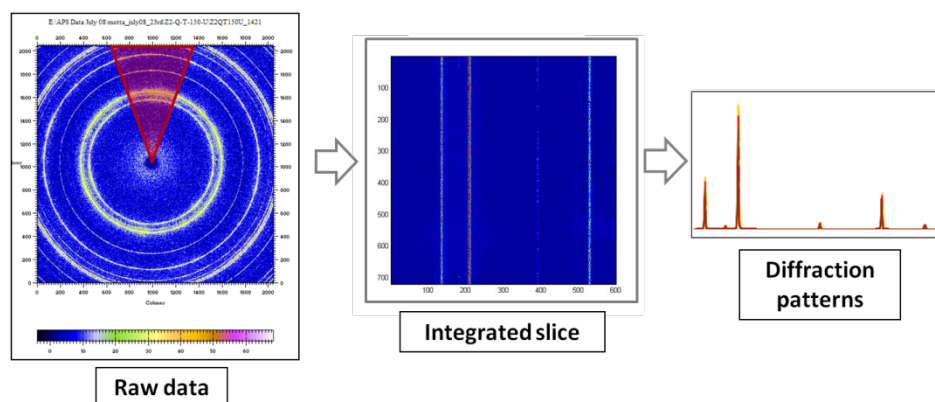


Figure E.19: Data Analysis procedure for X-Ray diffraction data collected at beamline 1-ID.

### *e) Sample preparation*

The preparation of the samples requires the following steps. The sample is exposed to high temperature of approximately 500–700°C in order for the sample to recrystallize to avoid change to the microstructure during the experiment. To prevent oxidation, the samples are coated with a deposited 100 nm layer of Nickel. Hydrogen is put into the sample using to the hydrogen charging equipment at Penn State University. Prior to the experiment, the concentrations were checked by performing a hydrogen hot vacuum extraction on small parts of the samples. Concluding the experiment, the hydrogen content was found by measuring the hydrogen concentration when then all of the hydride have dissolved because all of the hydrogen would be in solid solution. The hydrogen content found using these methods is gathered in Table E.6.

Table E.6: Overall hydrogen concentration in the APS samples

Sample Designation	Hot Vacuum Extraction content (wt. ppm)	Content at full dissolution (wt ppm)
A	400 ± 30	437 ± 40
B	541 ± 24	616 ± 60
C	603 ± 41	682 ± 70

The samples were heated to the dissolution temperature, in order to dissolve all the hydrides. This maximum temperature is held for 20 minutes, in order to reach a steady state. Then, the sample is cooled as fast as possible (about 1°C/s) to the target temperature (330°C in Figure E.20). The sample is then held at this temperature, while the supersaturated hydrogen precipitates. The resulting increase of the hydride peak intensity allows measuring the kinetics of precipitation.

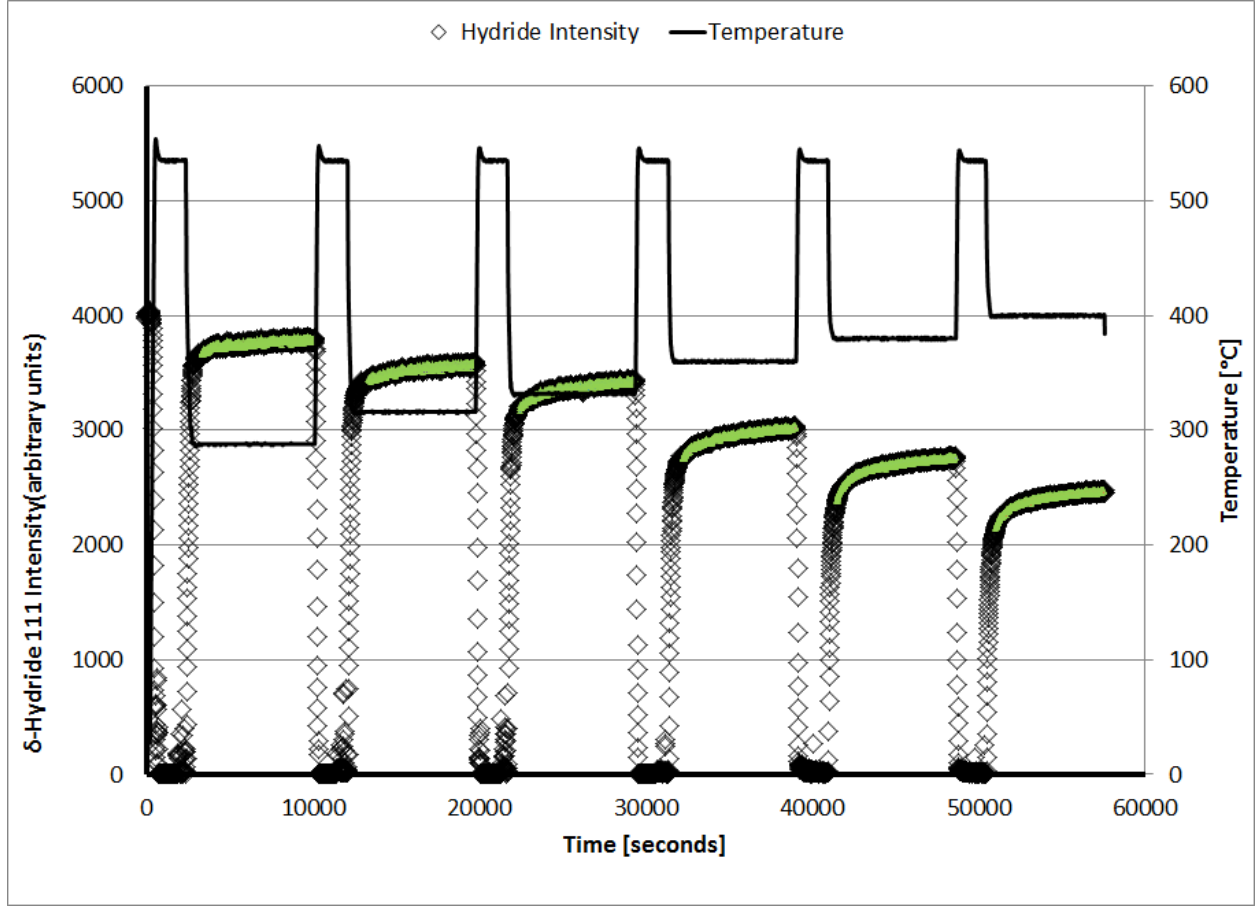


Figure E.20: Evolution of temperature and hydrides concentration during synchrotron experiment sample containing 541 wt ppm H

Since the loss of hydrogen from solid solution corresponds to hydrogen precipitation at the hydrides, the change in the amount of hydrogen in the hydrides ( $C_{pp}$ ) and the amount in solid solution ( $C_{ss}$ ) is given by:

$$\left\{ \begin{array}{l} \frac{dC_{pp}}{dt} = \alpha^2 (C_{ss} - TSSp) \\ \frac{dC_{ss}}{dt} = -\alpha^2 (C_{ss} - TSSp) \end{array} \right\} \quad \text{E-6}$$

According to the model, for a given holding temperature both the kinetics parameter  $\alpha^2$  and TSSp are constant. Rearranging equation E-6:

$$C_{ss}(t) = (C_{ini} - TSSp) \exp(-\alpha^2 t) + TSSp \quad \text{E-7}$$

where  $C_{ini}$  is the overall concentration of hydrogen in solid solution when the target temperatures has just been reached, corresponding to the beginning of the kinetics analysis. The concentration of hydrogen in the hydrides is:

$$C_{pp}(t) = -(C_{ini} - TSSp) \exp(-\alpha^2 t) + \text{constant} \quad \text{E-8}$$

By conservation of mass,

$$C_{TOTAL} = C_{pp}(t) + C_{ss}(t) = C_{pp}^{eq} + TSSp \quad E-9$$

With  $C_{TOTAL}$  being the total amount of hydrogen in the sample and  $C_{pp}^{eq}$  the equilibrium amount of hydrogen in the hydrides. Rearranging:

$$-\ln(C_{pp}^{eq} - C_{pp}(t)) = \alpha^2 t - \ln(C_{ini} - TSSp) + \text{constant} \quad E-10$$

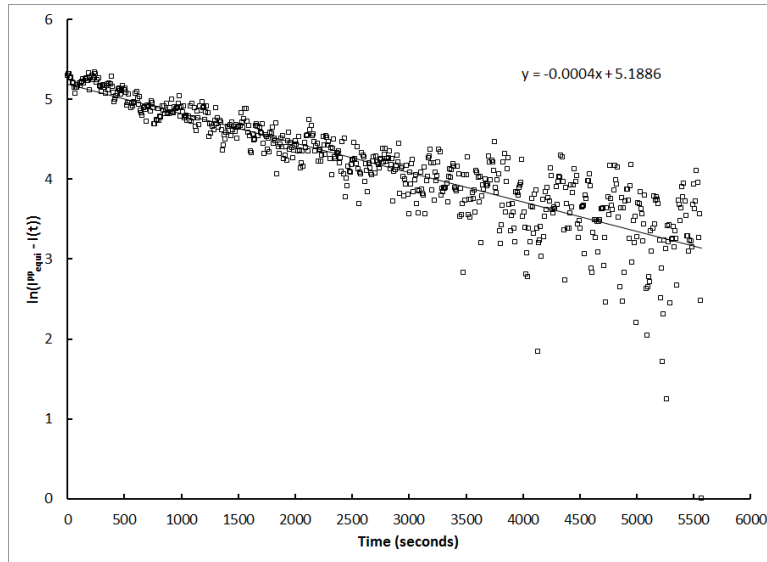
Assuming that the intensity of the (111) delta hydride peak is proportional to the volume fraction of hydrides, which is also proportional to the amount of hydrogen in hydrides (in wt. ppm), equation E-10 can be rewritten as a function of the hydride diffracted intensity  $I_{pp}$  and the same value at equilibrium

$I_{pp}^{eq}$  :

$$-\ln(I_{pp}^{eq} - I_{pp}(t)) = \alpha^2 t - \ln(C_{ini} - TSSp) + \text{constant} \quad E-11$$

This is due to an assumption that there no preferential orientation of the hydrides which may be a strong assumption. By holding the samples at the target temperature for sufficient time, it can be assumed that by the end of the respective cycle the amount of hydrogen in the hydrides has reached the  $C_{pp}^{eq}$ . Following this assumption, the last 1% of the points in each case were averaged to determine the equilibrium value of the hydride peak intensity  $I_{pp}^{eq}$  for the temperature of interest. Following equation E-11 the natural log of the difference of the hydride diffracted intensity and the same value at equilibrium was plotted against holding time. If the process is linear, a straight line should be obtained and the slope of the line is then equal to  $-\alpha^2$ .

Plotting the ln of the intensity against time allow the estimation of  $\alpha^2$  with a linear regression.



The hydride precipitation rate has been determined for five different temperatures and with three different initial concentrations. The measured values of  $\alpha^2$  are summarized in **Error! Not a valid bookmark self-reference.** Figure E.21 shows the value of  $\alpha^2$  against the absolute temperature.

Table E.7 Summary of  $\alpha^2$  measurements

Sample	T (°C)	$\alpha^2$ (seconds <sup>-1</sup> )	R <sup>2</sup> (%)
A	288	1.48 x 10 <sup>-4</sup>	65
	316	2.11 x 10 <sup>-4</sup>	90
	332	2.07E-04	94
B	288	1.63 x 10 <sup>-4</sup>	54
	316	1.90 x 10 <sup>-4</sup>	79
	332	1.82 x 10 <sup>-4</sup>	84
	360	1.82 x 10 <sup>-4</sup>	92
	380	1.96 x 10 <sup>-4</sup>	94
	400	2.10 x 10 <sup>-4</sup>	94
C	316	1.91 x 10 <sup>-4</sup>	78
	332	1.81 x 10 <sup>-4</sup>	89
	360	2.30 x 10 <sup>-4</sup>	89

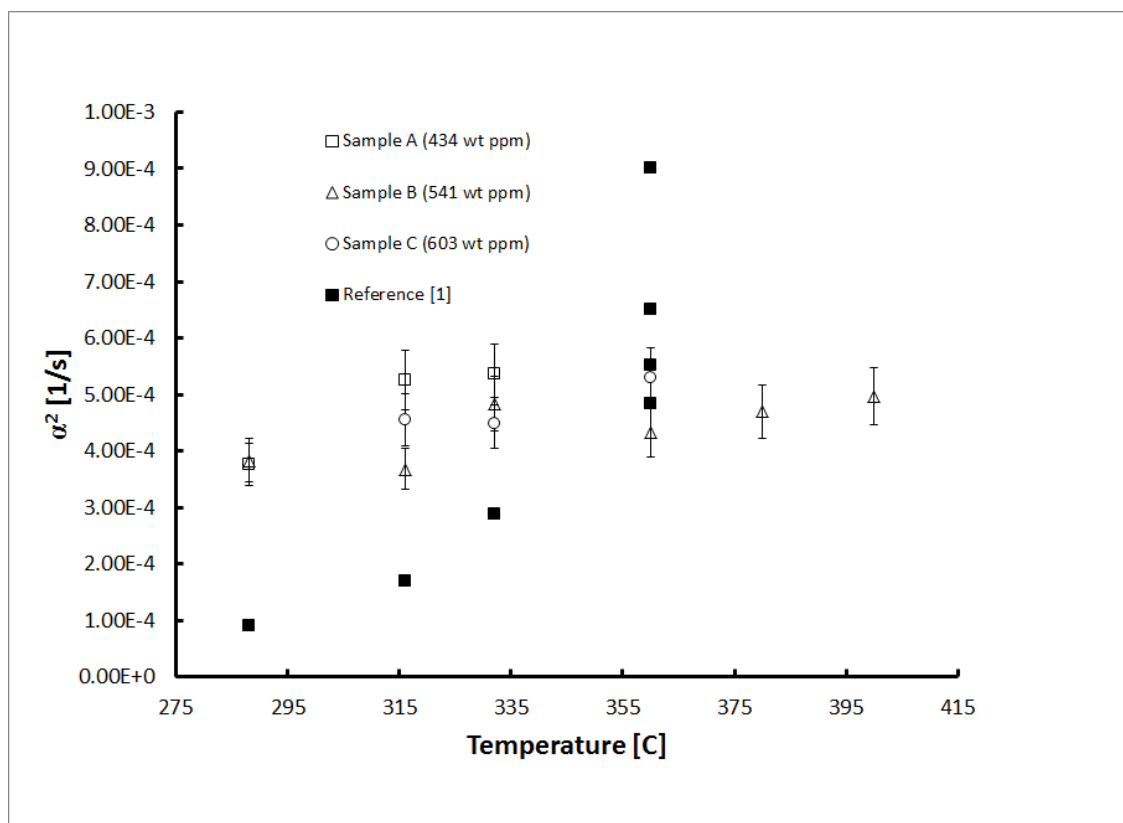


Figure E.21: Measured precipitation parameter  $\alpha^2$  with respect to T, with different initial concentration (434, 541 and 603 wt. ppm)



## F. Combined Results

This section covers the five primary results of this investigation. It includes multiple geometries that were used as models for the full three code coupling. The models were first run through the CTF-DeCART coupling to obtain power and temperature outputs which were then fed into the BISON code for finer temperature distribution, thermomechanics and hydrogen and hydride distribution simulations. The first model is a test, two-dimensional ( $r, z$ ) five pellet mesh. The next model is a full 360 fuel pellet rod. The last three models are two dimensional ( $r, \theta$ ) scenarios used to determine the azimuthal variation in temperature, hydrogen and hydride distribution. The first is a 4x4 sub assembly with a guide tube, the second is a 4x4 sub assembly with a control rod, and the third is a spalled oxide case. These cases were chosen based on certain artificial boundary conditions and scenarios that would cause large azimuthal variations in temperature and power.

### F.1. Results of 5-pellet rod simulation using BISON

#### F.1.1 Geometry and boundary conditions

The geometry consists of five  $\text{UO}_2$  stacked pellets with typical PWR pellets dimensions. Each pellet has dishes and chamfers. The pellets are surrounded by a Zircaloy-4 fuel cladding. The dimensions are given in Table F.1. The geometry is in 2 dimensions (radial and axial). Figure F.1 shows the simulation mesh, represented as half of each pellet and the cladding on one side (in blue), due to the invariance per rotation.

The two main inputs that have to be provided to BISON are the burnup and the outer cladding temperature. This data are obtained from the high fidelity calculation using CTF and DeCART, made by Ian Davis and described in section C. The calculations are made for a 4x4 assembly with the conditions described in Table F.2.



Table F.1: Pellet geometry in the PWR simulations

Type	Value	Units
Reactor	PWR	
Layout	4 x 4	
Fuel	UO <sub>2</sub>	
Enrichment	3.45%	
Fuel density	10.4	g/cc
% of theoretical density (10.96 g/cc)	95%	
Burnable poison	None	
Clad	Zircaloy-4	
Clad density	6.55	g/cc
Coolant	H <sub>2</sub> O	
Fill gas	Helium	
Fill gas density	0.0002	g/cc
Fuel pellet radius	0.4095	cm
Clad inner radius	0.418	cm
Clad outer radius	0.475	cm
Clad thickness	570	microns
Pin pitch	1.26	cm
Active fuel height	365.76	cm
Top reflector height	35.512	cm
Bottom reflector height	35.512	cm
Array power	1.0808	MW
Average linear heat rate	18.5	kW/m
Core pressure	15.5	Mpa
Mass flow rate	4.86	kg/s
BOC boron loading	1400	ppm
Inlet temperature	287	°C

Table F.2: Condition for five pellet DeCART-CTF coupling

Condition	Value
Geometrical parameters	PWR standard values*
Nominal Power	1.0808 MW
Inlet temperature	287°C
Pressure	15.5 MPa
Mass Flow Rate	4.8 kg/s
Isotopic fractions, Xenon, boron, depletion test	PWR standard values*

\* Detailed values are reported in Ian Davis's thesis [6]

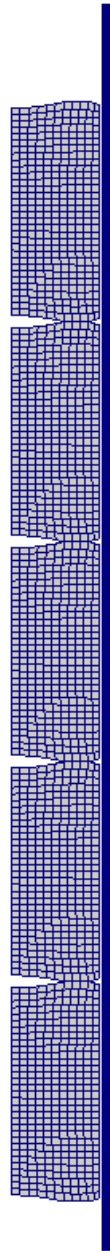


Figure F.1: Five pellet geometry for BISON simulation

The DeCART-CTF provides temperature and heat deposition distributions for each of the fuel rod of the simulated assembly. Each fuel rod contains 360  $\text{UO}_2$  pellets. A five pellet section is selected and the boundary conditions (Cladding temperature and energy deposition) are extracted from the CTF-DeCART calculation. It is assumed in the calculation that there is no axial heat flux and no axial hydrogen diffusion flux. Two different axial sections were chosen. The first one is where the highest temperature is observed in the cladding. It will be called the “hot 5 pellet rod” in the next sections. The second section is located close to the inlet and will be called the “cold 5 pellets rod” in the next sections.

### F.1.2 Hydrogen distribution in hot 5 pellets rod

Figure F.2 shows the axial temperature profile for this geometry. It can be observed that the temperature profile is similar from one pellet to another. This is due to the fact that the elevation of the temperature of the coolant is negligible for the small elevation corresponding to 5 pellets (about 6 cm). The cladding is subjected to a temperature gradient going from 330°C to 360°C, as shown in Figure F.3. The temperature in the cladding does not change significantly with time, as shown in Figure F.4. The average concentration of hydrogen after 4.5 years at 330°C will be about 70 wt. ppm. The TSSp at this temperature is 140 wt.ppm. [46] Therefore, no precipitation can be seen for this temperature. A BISON calculation confirms this observation. Figure F.5 shows the axial distribution that follows the same kind of pattern. The hydrogen moves toward the bottom of the cladding, as a result of the Soret effect. A small drop is observed at the location of the inter-pellet gap. Even if this difference is small, it creates a local cold spot where hydrogen will precipitate preferentially in the future.

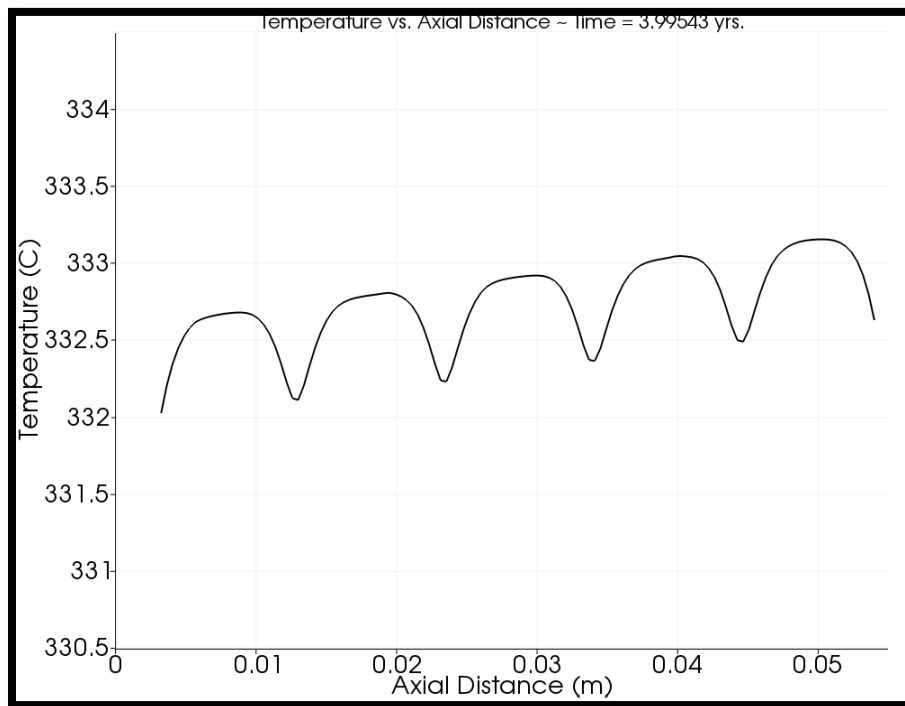


Figure F.2: Axial temperature profile for the hot 5 pellets mesh at the outer edge of the cladding, after 4 years

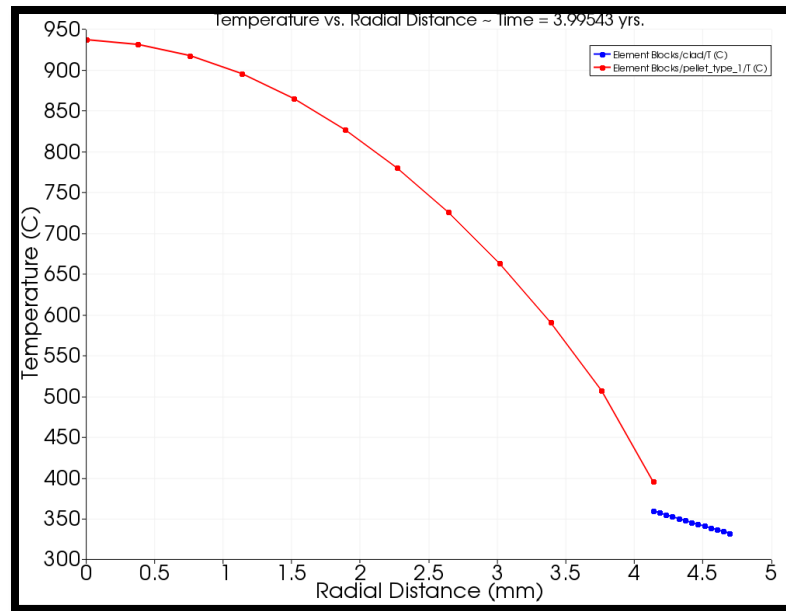


Figure F.3: Radial temperature profile for the hot 5 pellets mesh at  $z=2.75$  cm, after 4 years

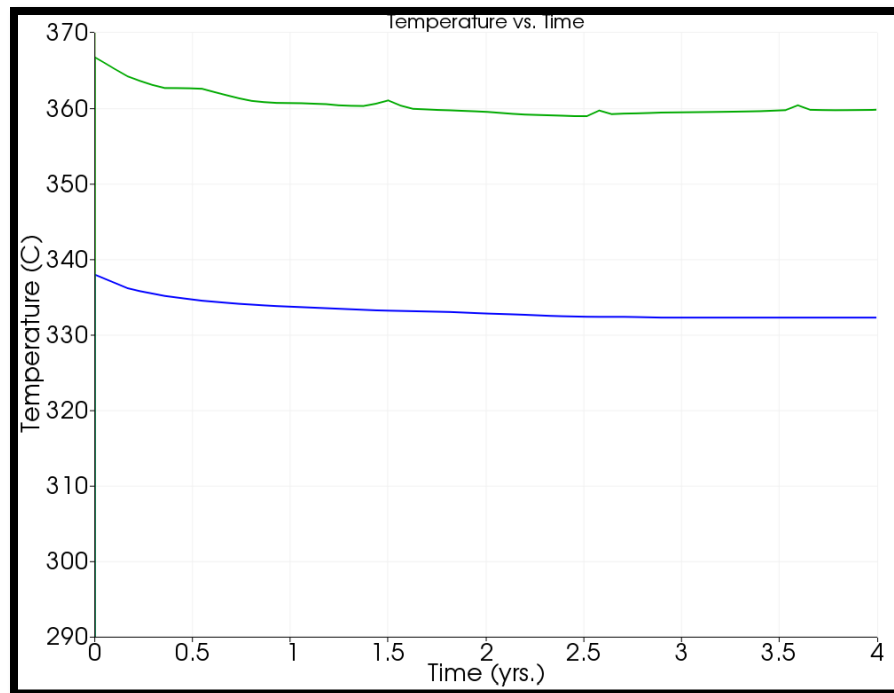


Figure F.4: Evolution of the cladding temperature for the hot 5 pellets at  $z=3.0$  cm and  $r=4.15$  mm and 4.2 mm (in green, inner edge), and  $r=4.67$  mm and 4.72 mm (blue, outer radius), between 0 years and 4 years

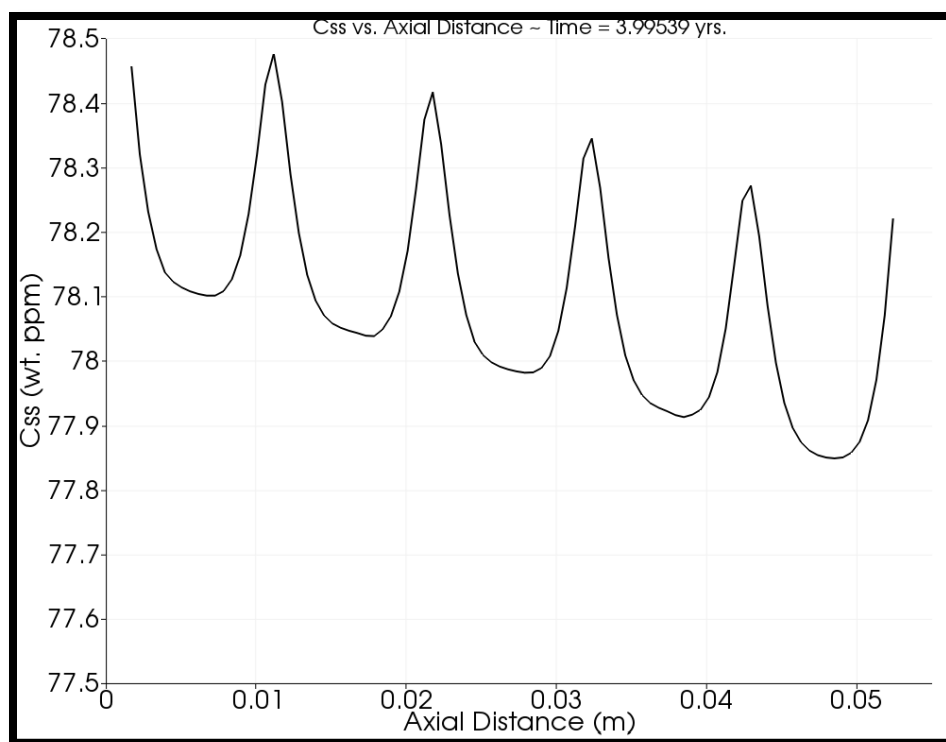


Figure F.5: Axial hydrogen profile for the hot 5 pellet mesh at the outer edge of the cladding, after 4 years

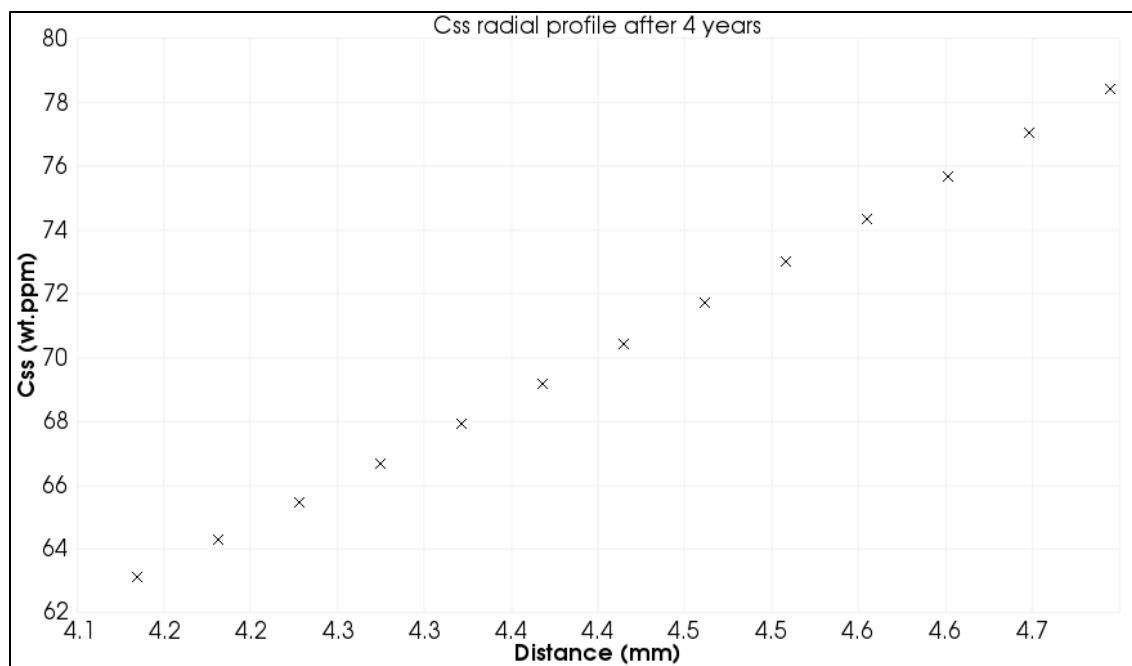


Figure F.6: Radial hydrogen profile for the hot 5 pellets mesh at  $z=2\text{cm}$ , after 4 years

### F.1.3 Hydrogen distribution in a cold 5 pellets rod

Figure F.7 shows the axial temperature profile for this simulation, after 4 years. Again, the temperature distribution depends mainly on the pellet geometry but does not show a significant increase relative to the coolant. Figure F.8 shows the radial distribution of hydrogen. The temperature goes from 300°C to 315°C. At 300°C, the average concentration of hydrogen after 4 years is about 22 wt.ppm and the TSSp is 99wt.ppm. Therefore no precipitation should be observed.

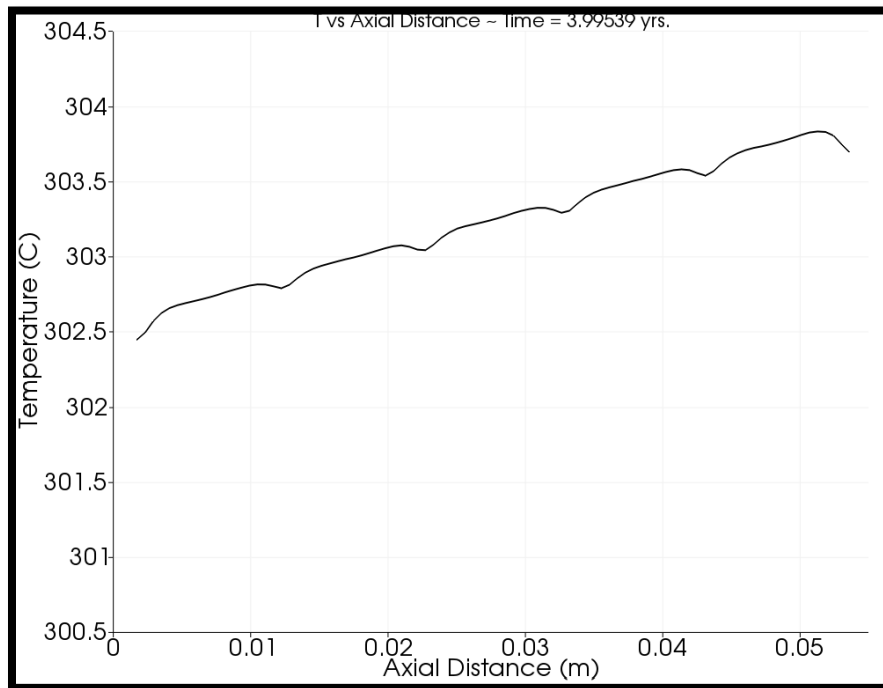


Figure F.7: Axial temperature profile for the 5 pellets mesh at the coldest spot of the fuel at the outer edge of the cladding, after 4 years

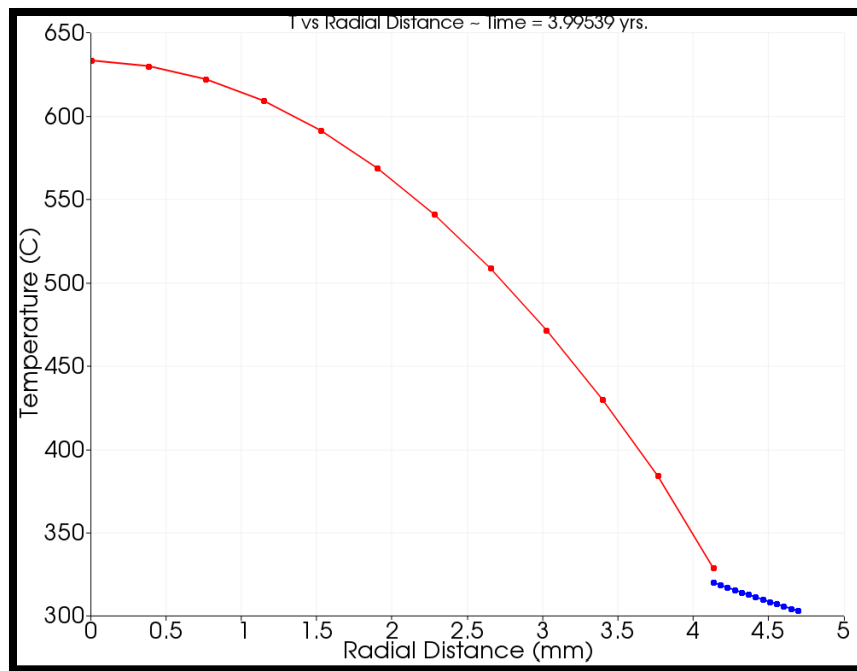


Figure F.8: Radial temperature profile for the hot 5 pellets mesh at  $z=3\text{cm}$ , after 4 years

However, the hydrogen diffuses from the top to the bottom of the rod. Because of this diffusion, the hydrogen concentration at the lower part of the cladding can reach the TSSp. In order to study the behavior of hydrogen in this case, the simulation was run with an initial concentration of 125 wt.ppm. Figure F.9 shows the variation of the hydrogen concentration with the axial dimension. The profile shows similar shape to the one seen in section corresponds to the formation of the rim. Figure F.10 shows the concentration of hydrogen in the hydrides as a function of radial distance. The radial direction is divided into 14 nodes. Only the last node shows precipitation, since once precipitation occurs, the hydrogen tends to migrate there. Thus, there is a very high (more than 6000 wt.ppm) concentration of precipitated hydrogen in the first node and none in the others. This can be corrected with a limit to the amount of precipitated hydrogen per unit of volume. This feature has not yet been implemented in BISON.

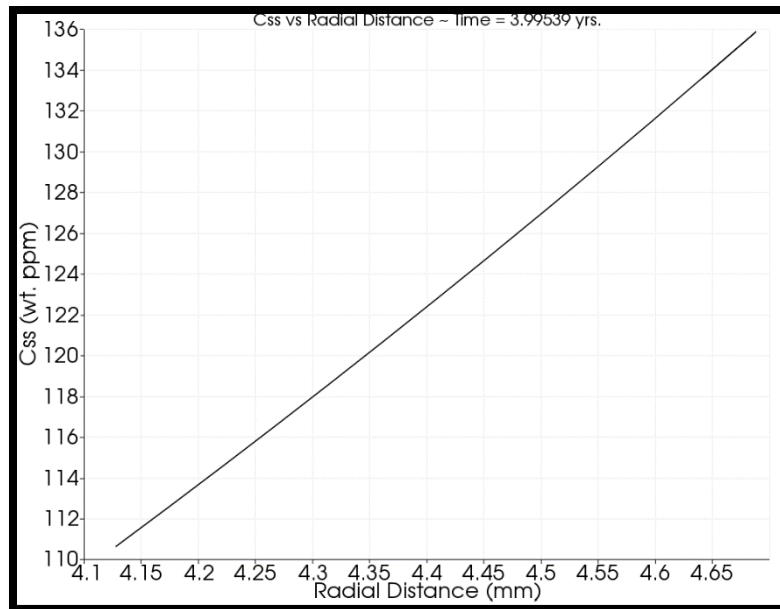


Figure F.9: Radial hydrogen profile for the cold 5 pellets mesh at  $z=$ , after 4 years

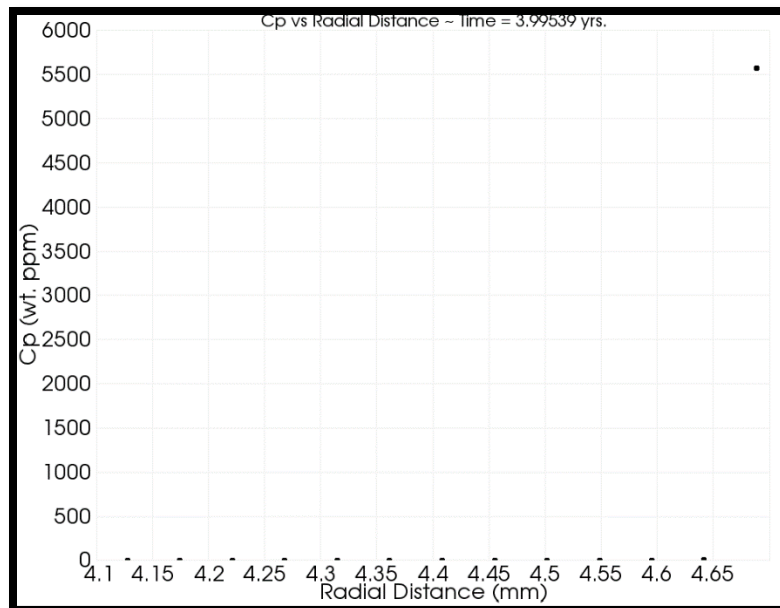


Figure F.10: Radial hydride profile for the cold 5 pellets mesh at  $z=$ , after 4 years

## F.2. Full rod results with BISON

As mentioned previously, the simulation of an entire fuel rod is not computationally feasible yet. This is due to the fact that the minimum time step required to run the hydrogen model is 200 seconds, which has to be done over a mesh of 360 pellets, requiring more than 65,000 nodes. The temperature calculation can be run separately using a large timestep (1E6 seconds) and takes about 12 hours for a 4-year simulation. The calculation of the evolution of the hydrogen distribution for 1 day took about 12 hours. Therefore, it



has been decided to run the hydrogen calculation only for 1 day. This calculation is still useful because at operating temperature, the typical diffusion length of hydrogen is about 1 cm, so that significant diffusion can occur. The purpose of this calculation is to confirm the axial redistribution of hydrogen. The initial hydrogen content was chosen at 60 wt.ppm. Figure F.11 shows the axial hydrogen profile after 1 hour. All the mesh points are represented in the figure. The upper line corresponds to the outer cladding. The second line is the second axial row of node (at a smaller radius). The third line is the third row. The bottom line corresponds to the inner cladding. The difference that occurs during the first hour corresponds to radial redistribution that is very fast. Figure F.12 represents the same distribution after 1 day. When compared to Figure F.11, a slight shift of the hydrogen concentration towards the bottom of the fuel can be observed. Figure F.13 shows the evolution of the radially averaged concentration of hydrogen for several elevations. This evolution is described by equation F-1.

$$DC_{ss} = [\bar{H}]_{3m} - [\bar{H}]_{1m} \quad \text{F-1}$$

Although the change is small, this confirms that the concentration is increasing at the bottom of the cladding and decreasing at the highest part of the cladding, thus confirming the fact that an axial diffusion occurs in the cladding in the time period observed (one day).

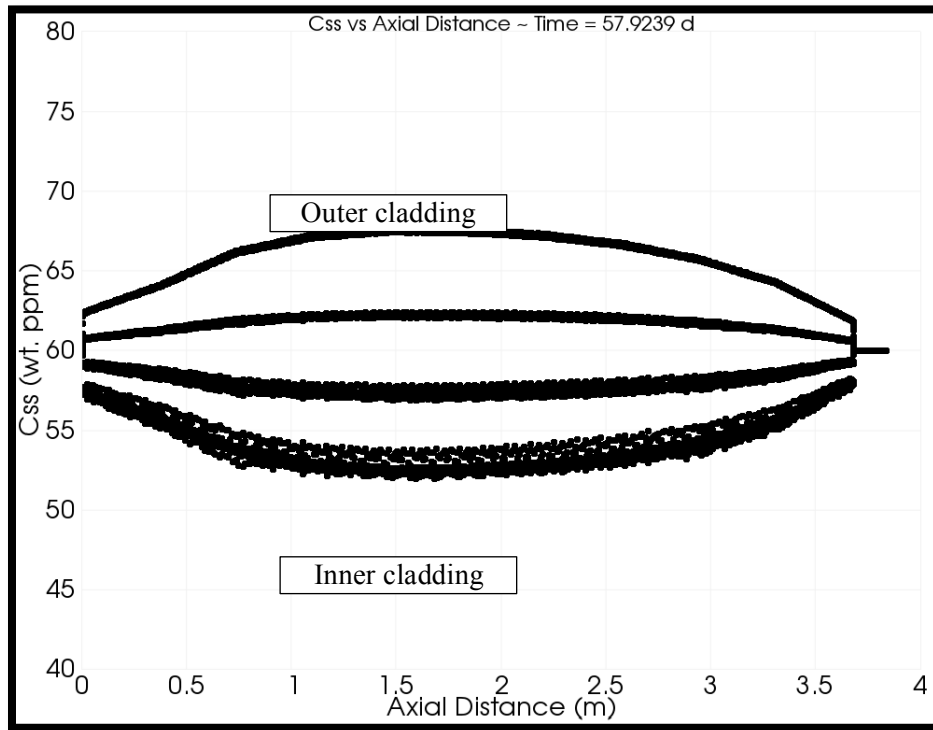


Figure F.11: Hydrogen profile in a 360-pellets fuel cladding after 1 hour, with an initial homogeneous concentration of 60 wt.ppm

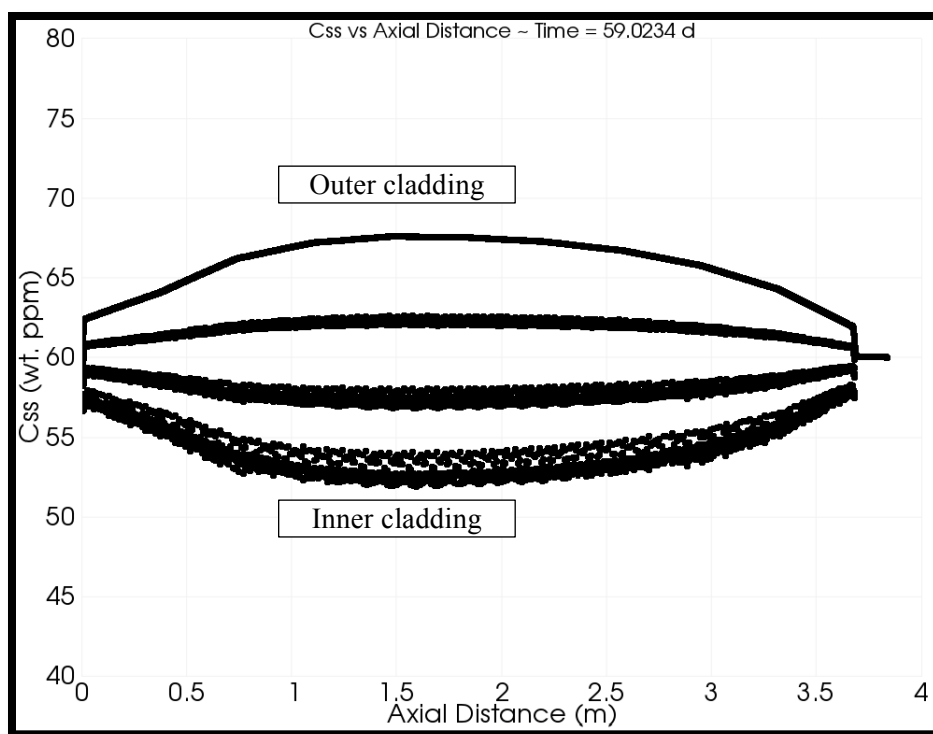


Figure F.12: Hydrogen profile in a 360-pellets fuel cladding after 1 day, with an initial homogeneous concentration of 60 wt.ppm

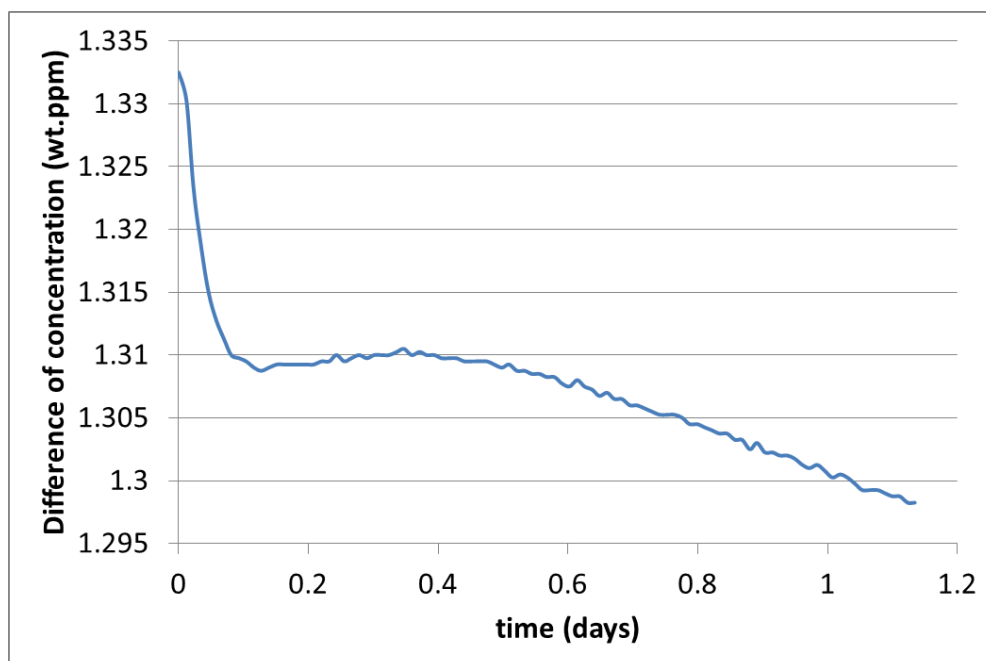


Figure F.13: Evolution of the difference average concentration between high ( $z=3\text{m}$ ) and low ( $z=1\text{m}$ ) elevations.

### F.3. 4x4 Sub-Assembly with Water Rod Combined Results

In order to test the azimuthally anisotropic capabilities of the hydrogen models, several cases were constructed to ensure azimuthal variations in the outer cladding temperature. The first case was similar to the section C.4.2 4x4 sub assembly, however, the enrichment was changed to a south east boarder of high enriched fuel and a remainder of the assembly as low enrich fuel (excluding the water tube in location 6). The parameters input for the CTF-DeCART model are found in Table F.3. A graphical representation of the geometry and enrichment distribution can be found in Figure F.14.

Table F.3: Parameter input for 4x4 Sub-Assembly with Guide Tube and Varying Enrichments

Parameter	Value	Units
Reactor	PWR	
Layout	4 x 4	
Fuel	UO <sub>2</sub>	
Enrichment		
High	4.95	
Low	1.00	
Fuel Density	10.4	g/cm <sup>3</sup>
Percent Theoretical Density	0.95	
Burnable Poison	None	
Cladding	Zircaloy-4	
Cladding Density	6.55	g/cm <sup>3</sup>
Coolant	H <sub>2</sub> O	
Fill Gas	Helium	
Fill Gas Density	0.0002	g/cm <sup>3</sup>
Fuel Pellet radius	4.095E-3	m
Cladding Inner Radius	4.18E-3	m
Cladding Outer Radius	4.75E-3	m
Cladding Thickness	5.70E-4	m
Pin Pitch	1.26E-2	m
Active Fuel Height	3.6576	m
Top Reflector Height	0.35512	m
Bottom Reflector Height	0.35512	m
Array Power	1.00	MW
Average Linear Heat Rate	18.5	kW/m
Core Pressure	15.5	MPa
Mass Flow Rate	4.86	Kg/s
Beginning of Cycle boron loading	1700	Ppm
Inlet Temperature	287	°C

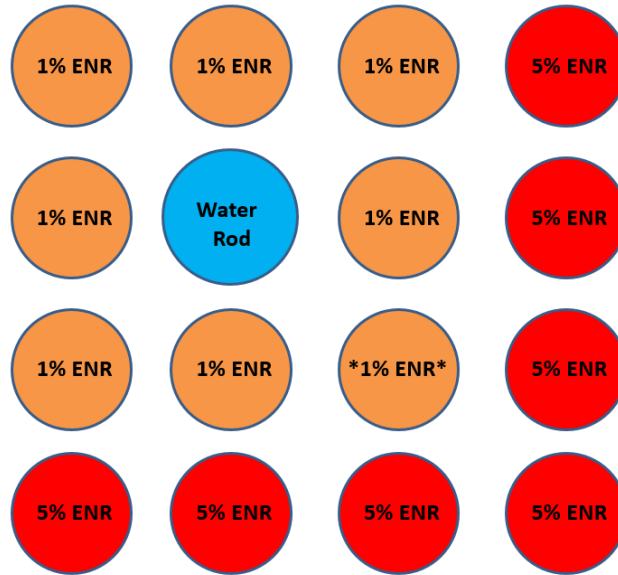


Figure F.14: 4x4 Sub-Assembly with Guide Tube layout at 0 MWd/kgU Burnup

For the CTF-DeCART coupling, the input was a full three-dimensional input that modeled the entire 3.62 meter active fuel length. However, the BISON model was created as a single two dimensional ( $r, \theta$ ) model, i.e., an x-y plane cut of a single fuel rod. The CTF-DeCART coupled calculation was first executed. An example of the outer cladding temperature distribution can be seen in Figure F.15. This temperature distribution is for the 38<sup>th</sup> axial COBRA-TF node for the 0 MWd/kgU burnup step (time zero). This vertical node corresponds to the 1.85 m - 1.90 m height in the core (just above the vertical center of the core). DeCART uses a different nodalization and has 18 vertical nodes meaning this CTF node corresponds to the 10<sup>th</sup> DeCART node.

305.1	305.0	304.8	304.5	303.7	310.7	334.2	341.5
1% Enr.		1% Enr.		1% Enr.		4% Enr.	
305.0	305.3	305.1	304.7	303.8	310.6	334.1	341.3
304.8	305.0	293.3	292.9	303.6	310.4	333.5	340.6
1% Enr.		Water Rod		1% Enr.		5% Enr.	
304.4	304.6	292.9	292.5	303.3	309.9	333.0	340.0
303.5	303.6	303.5	303.2	302.5	309.4	331.4	338.4
1% Enr.		1% Enr.		1% Enr.		5% Enr.	
310.7	310.5	310.4	310.0	309.3	312.2	334.3	337.4
333.9	333.8	333.2	332.7	331.2	334.1	332.4	335.6
5% Enr.		5% Enr.		5% Enr.		5% Enr.	
341.2	341.1	340.5	339.8	338.3	337.3	335.6	335.0

Figure F.15: Azimuthal Outer Cladding Temperature Distributions for CTF plane 38 at 0 MWd/kgU

The rod selected to run in the BISON simulation was rod 11 (highlighted on Figure F.15) as it had the largest azimuthal difference in temperature.

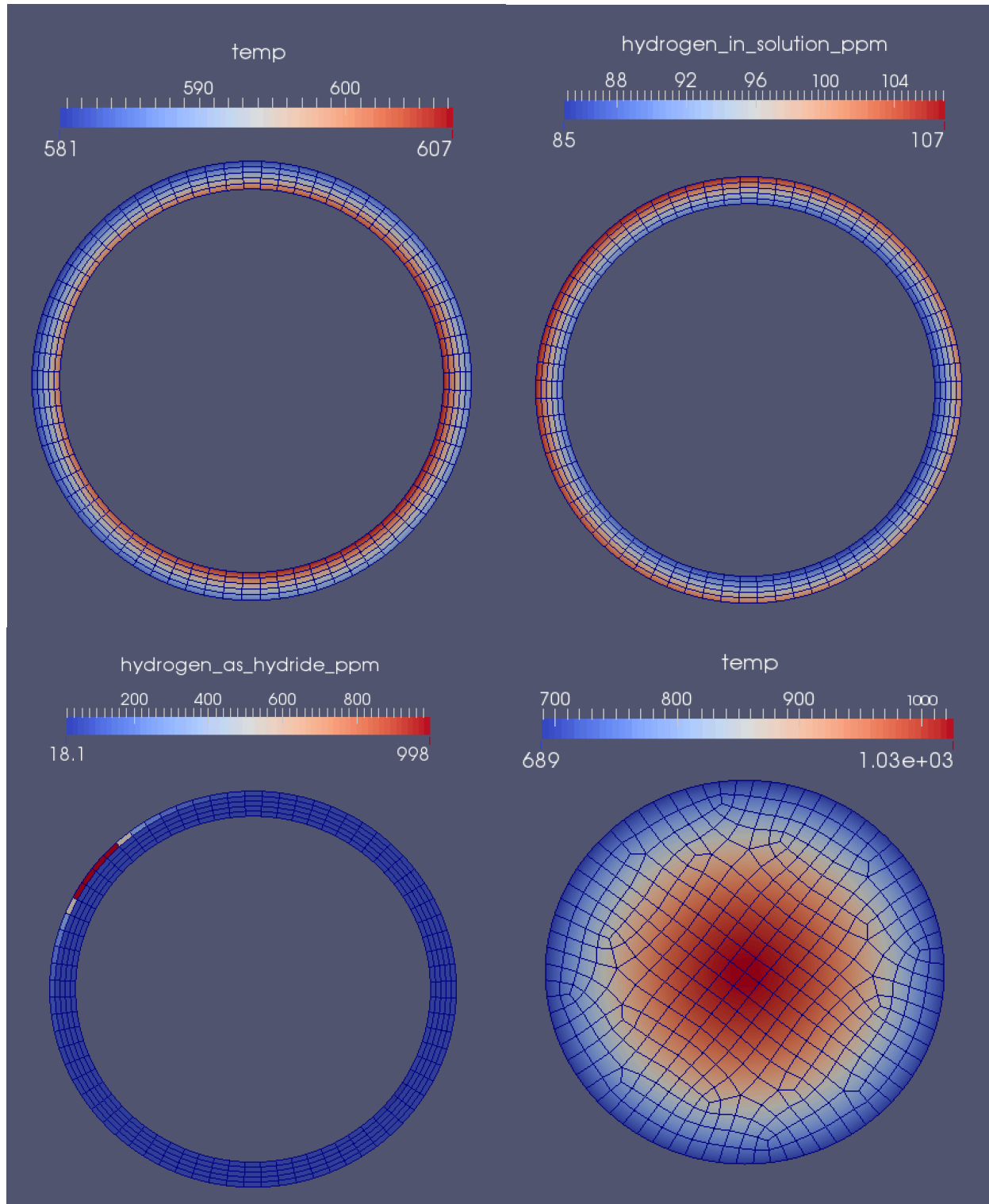


Figure F.16: Rod 11 1.85 m height BISON output at 3.43E7 seconds Top Left: Cladding temperature distribution Top Right: Cladding Hydrogen Distribution Bottom left: Cladding Hydride Distribution Bottom Right: Fuel Temperature

Note that the outer cladding temperatures in Figure F.16 do not reflect those seen in Figure F.15. This is because the azimuthal temperature variation changes with time. The BISON results shown are for the end of the 3.4 E7 second simulation. Also note the low fuel centerline temperature. This is due to the very low rod enrichment. Figure F.16 shows clear azimuthal variation in temperature and an appropriate response from the dissolved hydrogen and the precipitated hydride, following the lowest cladding temperatures. Figure F.17 shows the end of simulation temperature distribution within the cladding with respect to distance across the largest temperature gradient. As seen in the equation below.

$$TSSp_{water\_rod} = 138745.0 \exp\left(-\frac{4145.72}{581}\right) = 110 \text{ wt. ppm} \quad \text{F-2}$$

There shouldn't be any hydrides within the cladding. There is however a small amount in the top right corner and this is likely due to a hysteresis effect. In the timestep before the criteria for precipitation was met and the hydrogen in solid solution precipitated. However after precipitating the concentration of hydrogen in solid solution decreases and falls below the TSSp. When looking at the TSSd for this location,

$$TSSd_{water\_rod} = 106446.7 \exp\left(-\frac{4328.67}{581}\right) = 62 \text{ wt. ppm} \quad \text{F-3}$$

it becomes apparent that the criteria for dissolution is also met. This confirms why there would be a small amount in this cold region. Given more time a hydride rim would likely be seen as more hydrogen will be picked up by the cladding.

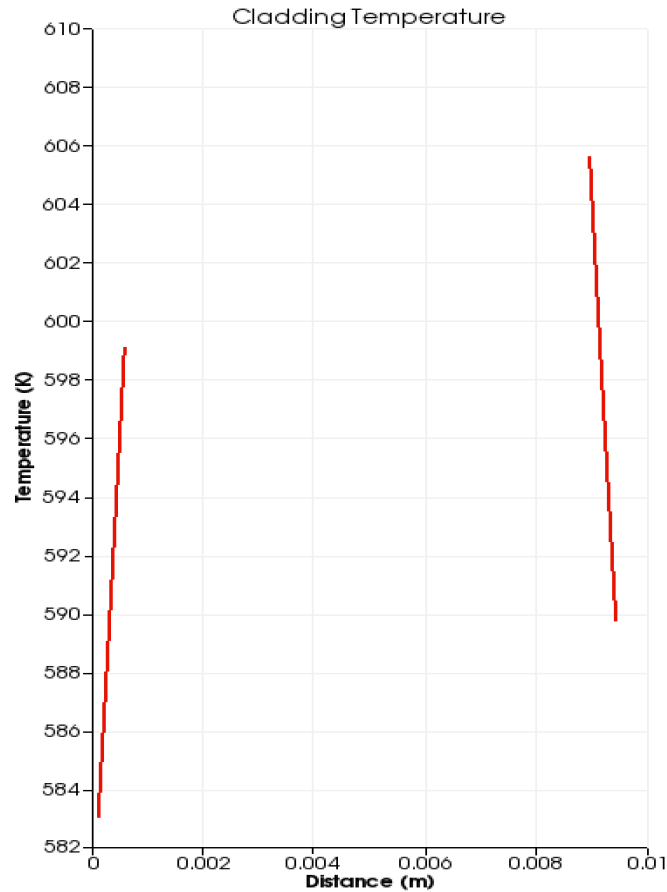


Figure F.17: Rod 11 axial height 1.85-1.90 m end of simulation BISON Cladding Temperature Distribution

#### F.4. 4x4 with control rod (increased power) results (including BISON)

The next azimuthally varying temperature case created was a 4x4 sub-assembly with a control rod inserted where the guide tube was. This was created not to model a physical situation, as commercial PWRs do not operate with rods inserted, but to create an anisotropic system. The input parameters were identical to the 4x4 water rod case in section F.3, with the only difference being the guide tube was filled with boron. Figure F.18: 4x4 Sub-Assembly with Control Rod layout at 0 MWd/kgU Burnup shows the xy planar layout of the sub-assembly.

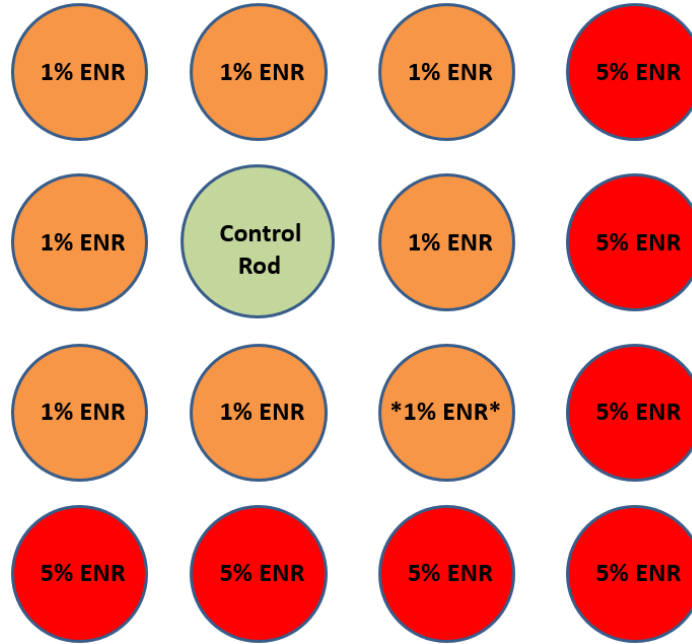


Figure F.18: 4x4 Sub-Assembly with Control Rod layout at 0 MWd/kgU Burnup

This calculation was simulated for a shorter operation time in BISON,  $1.1E7$  seconds as opposed to  $3.4E7$  in the previous case. The results at the end of this cycle time are shown in Figure F.19. It can be seen that there was no concentration of hydrides. This is due to the conditions in the core not allowing enough hydrogen absorption in the cladding to exceed the TSSp which is the minimum requirement for precipitation of hydrogen. For the lowest temperature of the cladding, the TSSp has a value of:

$$TSSp_{control\_rod} = 138745.0 \exp\left(-\frac{4145.72}{583}\right) = 113 \text{ wt. ppm} \quad \text{F-4}$$

The reason why the concentration of hydrogen in solid solution is lower compared the water rod case is because the simulation was shorter which did not allow for enough time to pick up hydrogen within the cladding. Figure F.20 shows the temperature distribution within the cladding with respect to distance across the largest temperature gradient.



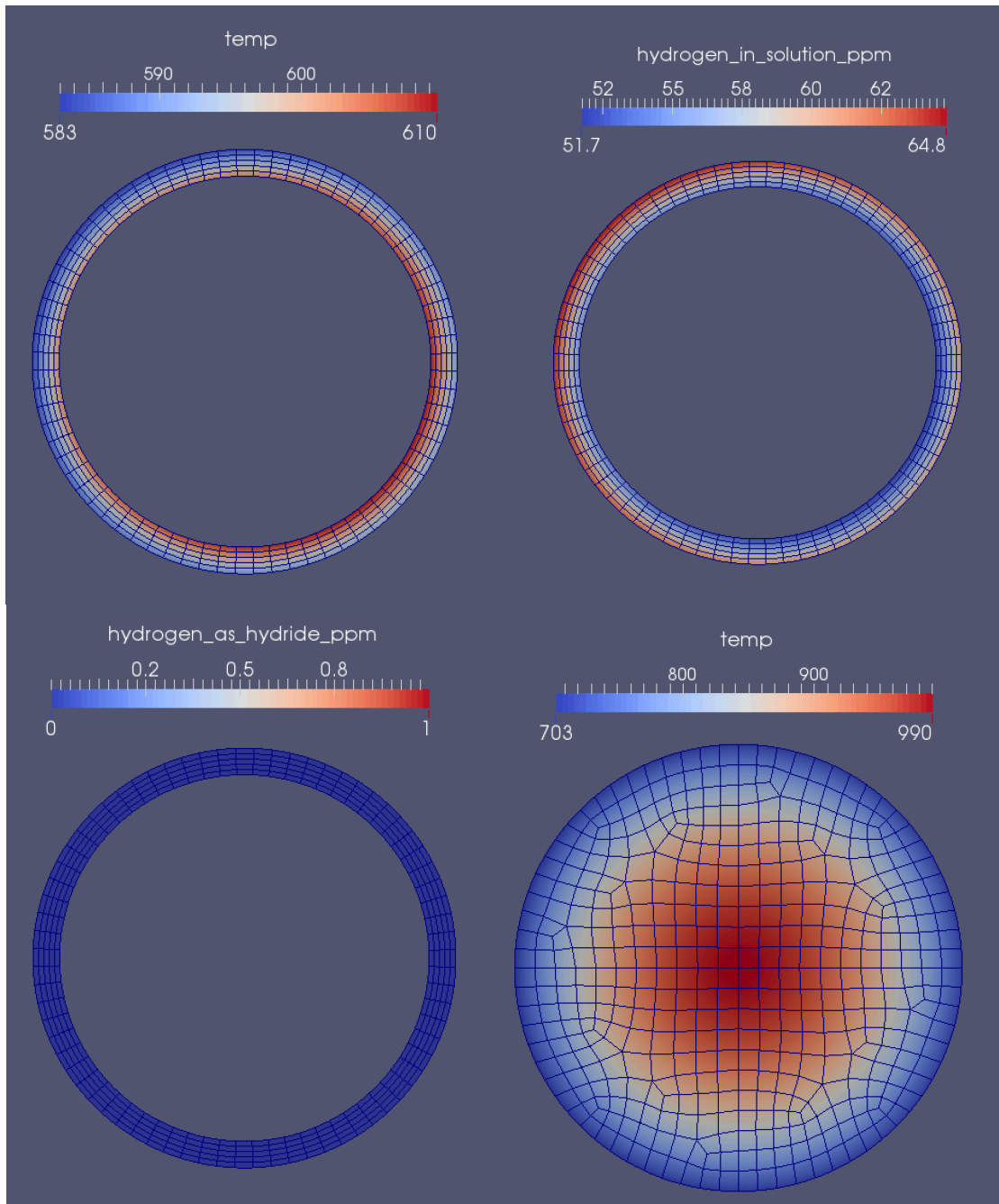


Figure F.19: Rod 11 1.85 m height BISON output with control rod in assembly at 11E6 seconds Top Left: Cladding temperature distribution Top Right: Cladding Hydrogen Distribution Bottom left: Cladding Hydride Distribution Bottom Right: Fuel Temperature

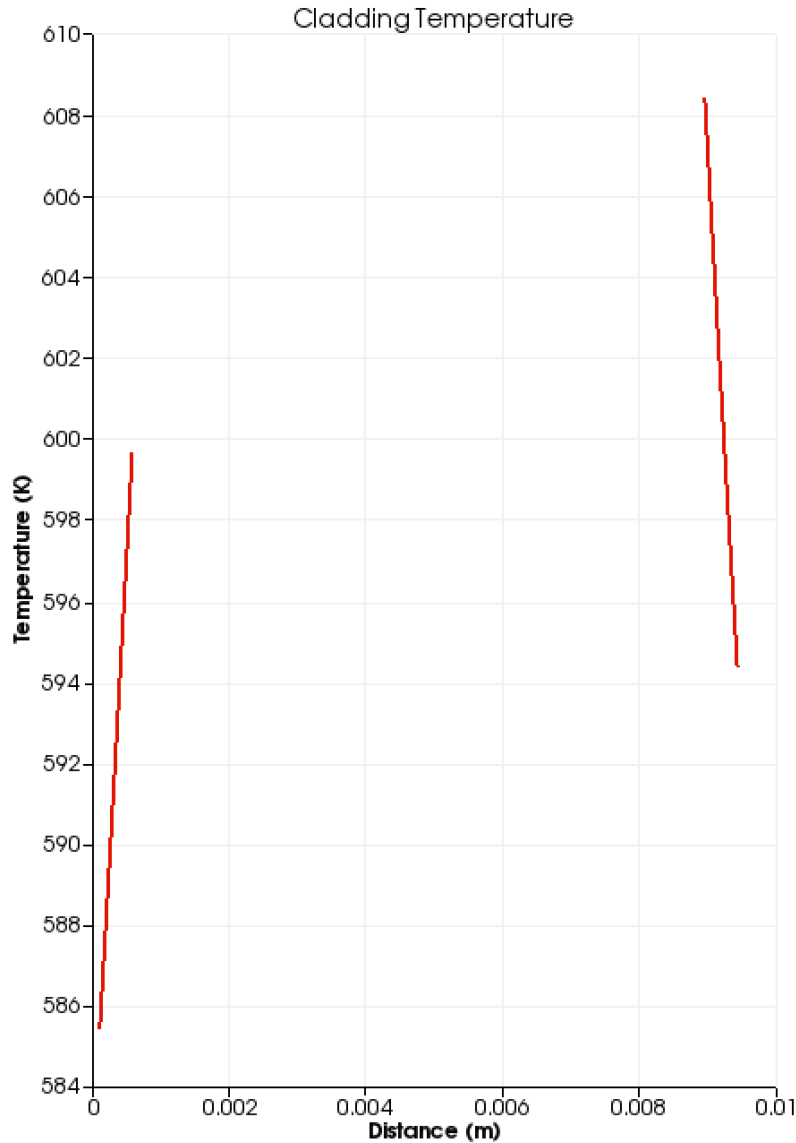


Figure F.20: Rod 11 axial height 1.85-1.90 m end of simulation BISON Cladding Temperature Distribution Control Rod Case

### F.5. Spalled Oxide

A spalled oxide event occurs when a portion of the oxide layer breaks off from the outside of the cladding. When this occurs a large cold region is created because the new surface is directly in contact with the coolant. This promotes more heat transfer and subsequently a large local temperature gradient. It has been observed that a hydride blister forms in the location of the spalled oxide.

This was simulated using a different thermal conductivity in a cladding section (top left). This equivalent thermoconductivity represents the missing oxide layer that spalled. The simulation used a uniform power distribution of 25kW/m for the pellet section and does not specify a boundary condition for outer cladding temperature as the previous cases did. This freedom allows the cladding to apply heat transfer based only on the different thermal conductivities. An initial concentration of hydrogen in solid solution of 100 wt.

ppm was used in order to simulate closer to the onset of precipitation. The effective thermal conductivity was calculated by using the following series of thermal resistances.

$$\frac{\ln\left(\frac{r_3}{r_1}\right)}{2\pi * k_{equi}} = \frac{\ln\left(\frac{r_2}{r_1}\right)}{2\pi * k_1} + \frac{\ln\left(\frac{r_3}{r_2}\right)}{2\pi * k_2} \quad \text{F-5}$$

$$\frac{\ln\left(\frac{r_3}{r_1}\right)}{2\pi * k_{equi}} = \frac{\ln\left(\frac{r_2}{r_1}\right)}{2\pi * k_1} + \frac{\ln\left(\frac{r_3}{r_2}\right)}{2\pi * k_2} \quad \text{F-6}$$

$$k_{equiv} = \frac{\ln\left(\frac{r_3}{r_1}\right)}{\frac{\ln\left(\frac{r_2}{r_1}\right)}{k_1} + \frac{\ln\left(\frac{r_3}{r_2}\right)}{k_2}} \quad \text{F-7}$$

The inner cladding radius is 4.16 mm, the outer cladding radius is 4.76 mm and assuming an oxide thickness of 100  $\mu\text{m}$  the follow equivalent thermal conductivity is assumed.

$$k_{equi} = \frac{\ln\left(\frac{4.77}{4.16}\right)}{\frac{\ln\left(\frac{4.76}{4.16}\right)}{16} + \frac{\ln\left(\frac{4.77}{4.76}\right)}{1.6}} = 14.0 \frac{W}{mK} \quad \text{F-8}$$

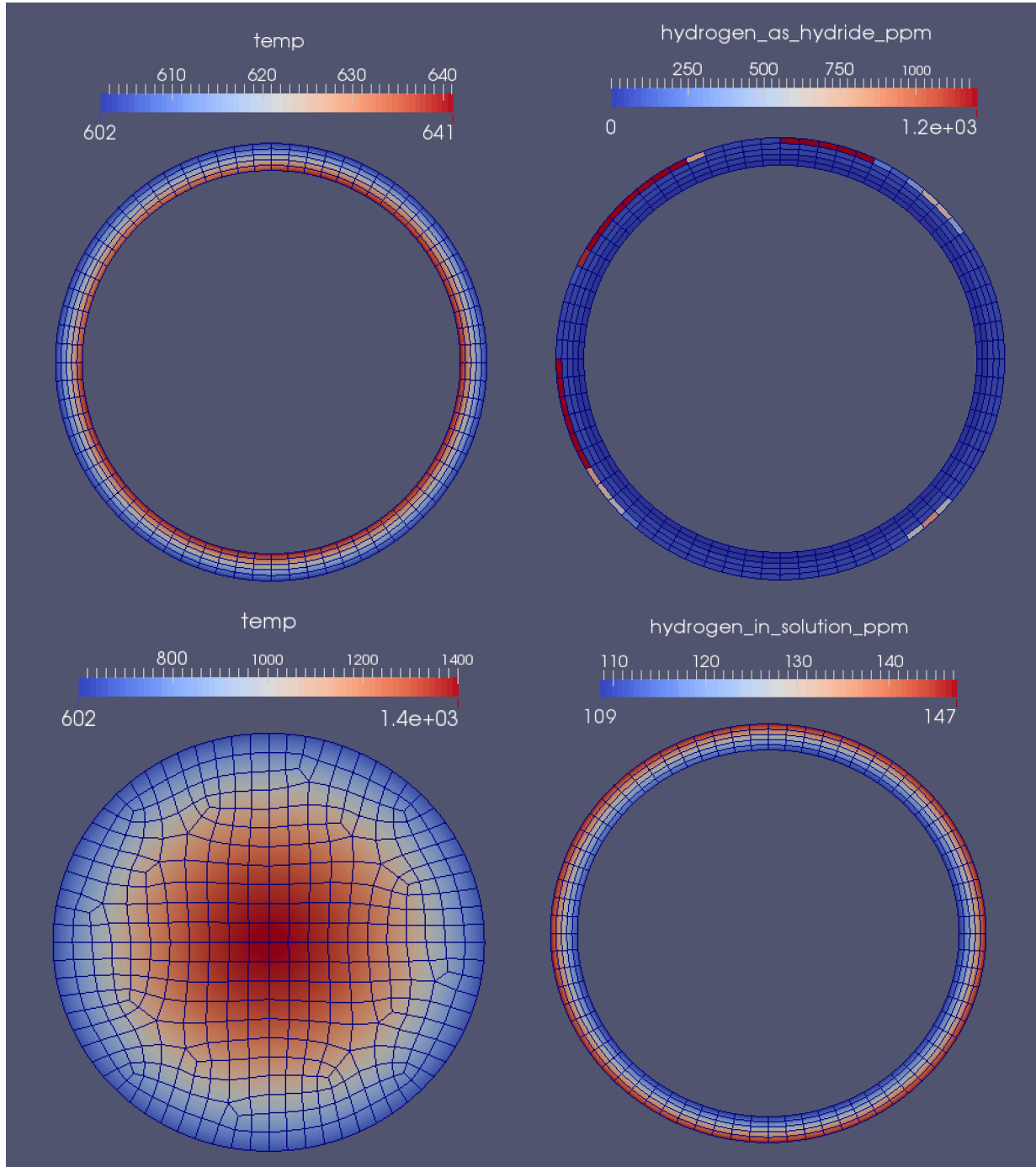


Figure F.21: Top Left (a): Hydrogen as hydride distribution after 2.5 years, top right (b): fuel pellet temperature distribution, bottom left (c): hydrogen in solid solution distribution, bottom right (d): cladding temperature distribution

In Figure F.18b, the fuel temperature distribution is described. Figure F.18d describes the cladding temperature distribution. It should be noted that there is a slight difference in temperature when plotted from the top left to the bottom right. This difference is depicted in Figure F.19. This temperature gradient causes the hydrogen distribution too slightly skew towards the cold region in the top left as shown in Figure F.18c. Figure F.18a is the hydride distribution. It is expected that the hydride form in the top left to produce the hydride blister mentioned earlier.

This is because the criteria for precipitation has been met. The concentration exceeds the TSSp in the coldest region as seen in the equation below meaning precipitation occurs.

$$TSSp_{spalled\ oxide} = 138745.0 \exp\left(-\frac{4145.72}{602}\right) = 142\ wt.\ ppm \quad F-9$$

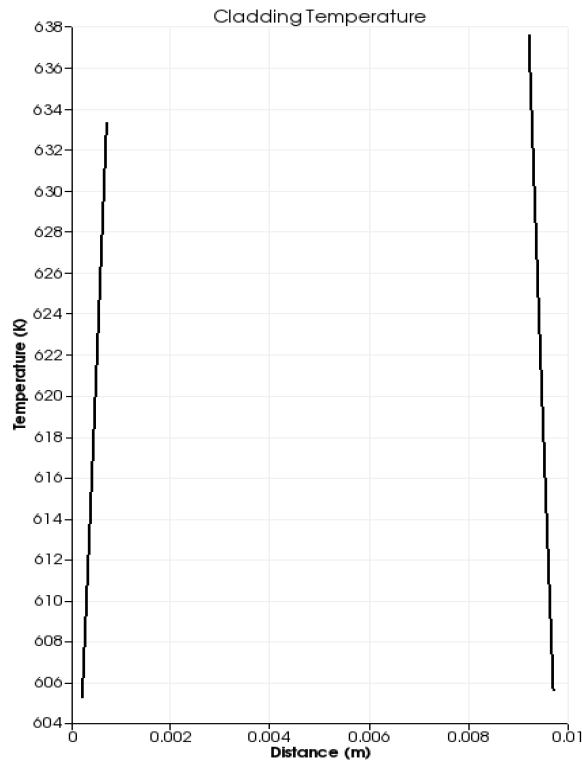


Figure F.22: Cladding temperature distribution for the spalled oxide event.

## G. Conclusions

Of high importance in fuel performance is the degradation of the zirconium cladding. In the high temperature environment of a reactor, the zirconium in the cladding tends to corrode, and in the process hydrogen is released. Some of this hydrogen is absorbed by the cladding in a highly inhomogeneous manner. The distribution of the absorbed hydrogen is extremely sensitive to temperature and stress concentration gradients. The absorbed hydrogen tends to concentrate near lower temperatures. This hydrogen absorption and hydride formation can cause cladding failure. This project was designed to improve the hydrogen distribution prediction capabilities of the BISON code. The project was split into two primary sections, first was the use of a high fidelity multi-physics coupling to accurately predict temperature gradients as a function of  $r$ ,  $\theta$ , and  $z$ , and the second was to use experimental data to create an analytical hydrogen precipitation model.

The thermal hydraulics code CTF was successfully coupled to the DeCART neutronics code. This coupled system was verified by testing and validated by comparison to FRAPCON data. The hydrogen diffusion and precipitation experiments successfully calculated the heat of transport and precipitation rate constant values to be used within the hydrogen model in Bison. These values can only be determined experimentally.

These values were successfully implemented in precipitation, diffusion and dissolution kernels that were implemented in the BISON code. The coupled output was fed into BISON models and the hydrogen and hydride distributions behaved as expected. Simulations were conducted in the radial, axial and azimuthal directions to showcase the full capabilities of the hydrogen model.

Based on obtained results in this project, the formation of the rim can be explained by a competition between diffusion and precipitation, localized at the coldest parts of the cladding, where the TSSp is the lowest. The existence of hydrides needs to take into account the axial transfer of hydrogen from the top of the cladding, where the oxidation is the highest, to the bottom part of the cladding, where the TSSp is the lowest. The rim thickness is explained by the precipitation kinetics. The fact that hydrogen needs time to precipitates creates a small amount of hydrogen in super saturation that diffuses into the cladding. However, this effect is small and implies a very high concentration (full hydride) close to the outer edge of the cladding. In section D.2, a limitation was applied to the amount of hydrogen in precipitated hydrides. This leads to a much more reliable thickness for the rim (~100 microns) after 4 years. However, even if this limitation has qualitative explanations, the quantitative limitation is only based on rough estimation from previous observation.

The results of this project indicate the ability of the coupled multi-physics codes to accurately predict temperature, hydrogen, and hydride distributions. The distribution of hydrides the BISON output was validated by the TSSp and TSSd simple calculations.

## H. Publications

This DOE project spanned three years and included the participation of 7 students, both graduate and undergraduate including: Olivier Courty, Kevin Cass, Ian Davis, Michael Mankosa, Daniel Nunez, Christopher Piotrowski, and Tristalee Williams. The following lists the publications that were generated during this project:

1. Davis, Ian. High-Fidelity Multi-Physics Coupling For Prediction of Anisotropic Power and Temperature Distribution in Fuel Rod: Impact on Hydride Distribution. Masters Thesis in Nuclear Engineering, The Pennsylvania State University, 2013.
2. Courty, Olivier. Hydrogen Distribution in Zircaloy under a Temperature Gradient: Modeling, Simulation and Experiment. Masters Thesis in Nuclear Engineering, The Pennsylvania State University, 2013.
3. Piotrowski, Christopher. Azimuthal Hydrogen Concentration Factor using the BISON Fuel Performance Code. Masters Thesis in Nuclear Engineering, The Pennsylvania State University. In preparation.
4. Courty, Olivier, A.Motta, J.Hales. Modeling Hydrogen Re-Distribution in Zircaloy under a Temperature Gradient. TMS Conference Presentation. San Antonio, Texas. 2013.
5. Davis, Ian; Courty, Olivier; Avramova, Maria; Ivanov, Kostadin; Motta, Arthur. High-Fidelity Multi-Physics Coupling for Prediction of Anisotropic Power and Temperature Distributions in Fuel Rod: Impact on Hydride Distribution. NURETH-15 Conference Proceedings. May 2013.

6. Courty, Olivier. Hydrogen Distribution In Zircaloy Under A Temperature Gradient: Modeling, Simulation And Experiment. 2013. MSc thesis in Nuclear Engineering, The Pennsylvania State University.
7. Ian Davis, Olivier Courty, Maria Avramova, Arthur Motta, Kostadin Ivanov. NURETH-15 Conference Proceedings. High-Fidelity Multi-Physics Coupling for Prediction of Anisotropic Power and Temperature Distributions in Fuel Rod: Impact on Hydride Distribution. May 2013
8. Olivier Courty, Arthur Motta, Christopher Piotrowski. Measurement of the kinetics of precipitation in Zircaloy-4. Submitted to Journal of nuclear materials, October 2014.
9. Courty, Olivier; Motta, Arthur; Hales, Jason (INL). 3-Dimensional simulation of hydrogen diffusion and precipitation in Zircaloy-4 fuel cladding. Journal of Nuclear Materials. Volume 452. (2014) Pages 311-320.
10. Ian Davis, Olivier Courty, Maria Avramova, Kostadin Ivanov, Arthur Motta, "Simulation of the redistribution of hydrogen in a nuclear fuel cladding based on a coupling between neutronics, thermohydraulics and fuel performance code" Nuclear Technology, to be submitted, 2014.
11. Williams, Tristalee; Davis, Ian. Comparison and Benchmarking of BISON against FRAPCON cases with PWR, UO<sub>2</sub> Fuel and Zircaloy-4 Cladding Criteria. Toshiba Westinghouse scholar project. 2012. The Pennsylvania State University.
12. Cass, Kevin. Analysis of BISON's Capability to Model Hydrogen and Hydride Distribution. Toshiba Westinghouse Project. 2013 The Pennsylvania State University.
13. Nunez, Daniel. Measurement of Hydrogen Redistribution under a Temperature Gradient in Zircaloy-4. Toshiba Westinghouse scholar project. 2012. The Pennsylvania State University.
14. Piotrowski, Christopher; Mankosa, Michael. Anisotropic Azimuthal Power and Temperature Distribution Impact on Hydride Distribution. Abstract Accepted for American Nuclear Society Winter Meeting, November 2014.

## I. References

- [1] J. D. Hales, S. R. Novascone, G. Pastore, D. M. Perez, B. W. Spencer, R. L. Williamson. BISON Theory Manual: p. 5. Idaho National Laboratory. June 2014.
- [2] Williams, T. and I.J. Davis. *Comparison and Benchmarking of BISON against FRAPCON cases with PWR, UO<sub>2</sub> Fuel and Zircaloy-4 Cladding Criteria*. 2012. The Pennsylvania State University.
- [3] Geelhood, K.J., W.G. Luscher, and C.E. Beyer. *FRAPCON-3.4: Integral Assessment*. 2011. Pacific Northwest National Laboratory.
- [4] Bison Workshop Manual. Idaho National Lab. Fuels Modeling and Simulation Department. June 2014.
- [5] Kochunas, B., Hursin, M., Downar, T., DeCART-v2.05 Theory Manual, 2009, University of Michigan.
- [6] Davis, Ian. *High-Fidelity Multi-Physics Coupling For Prediction of Anisotropic Power and Temperature Distribution in Fuel Rod: Impact on Hydride Distribution*. 2013. The Pennsylvania State University
- [7] Hamilton, S., Clarno, K., Philip, B., Berrill, M., Sampath, R., Allu, S., *Integrated Radiation Transport and Nuclear Fuel Performance for Assembly-Level Simulations*, in *PHYSOR 2012* 2012: Knoxville, TN.

- [8] *SIMULATE-3: Advanced Three-Dimensional Two-Group Reactor Analysis Code*, 2009, Studsvik.
- [9] IAEA, *Waterside Corrosion of Zirconium Alloys in Nuclear Power Plants*, 1998, International Atomic Energy Agency: Vienna. IAEA TECDOC-966
- [10] Garzarolli, F., et al. *Review of Corrosion and Dimensional Behavior of Zircaloy under Reactor Water Conditions*. 1979. ASTM STP 681, p.91.
- [11] Sawatzky, A., *The heat of transport of hydrogen in zirconium alloys*. Journal of nuclear Materials, 1963. 9(3): p. 364.
- [12] Kearns, J.J., *Diffusion Coefficient of Hydrogen in Alpha Zirconium, Zircaloy-2 and Zircaloy-4*. J. Nuclear Materials, 1972. 43: p. 330-338.
- [13] Prigogine, D.K.a.I., *Modern Thermodynamics* 1998: John Wiley & Sons.
- [14] Daum, R.S., "Hydride Induced Embrittlement of Zircaloy-4 Under Plane Strain Tension Testing," PhD Thesis in Materials Science, Penn State University, 2007
- [15] Smith, G., *Evaluation and Demonstration of Methods for Improved Fuel Utilization*, in ET/34013-15, CND-4321994, DOE.
- [16] McMinn, A., E.C. Darby, and J.S. Schofield. *The terminal solid solubility of hydrogen in zirconium alloys*. in *12th Int. Symp. on Zr in the Nuclear Industry*. 2000. Toronto, CA: ASTM.
- [17] Shewmon, *Redistribution of second phase during annealing in temperature gradient*. Transactions of the Metallurgical Society of AIME, 1958. 212: p. 642-647.
- [18] Marino, G.P., *Hydrogen Supercharging in Zircaloy*. Materials Science and Engineering, 1971. 7(1971): p. 335-341.
- [19] Marino, G.P., *HYDIZ: A 2-dimensional computer program for migration of interstitial solutes of finite solubility in a thermal gradient (LWBR Development Program)*, in *AEC Research and Development Report - WAPD-TM-1157* 1974.
- [20] Bruce F. Kammenzind, D.G.F., H. Richard Peters and Walter J. Duffin, *Hydrogen Pickup and Redistribution in Alpha-Annealed Zircaloy-4*. Zirconium in the Nuclear Industry: 11th International Symposium, 1996. ASTM STP 1295: p. 338-370.
- [21] Williamson, R., S.H. Novascone, J.; , and B. Spencer, *BISON Workshop*, I.N. Laboratory, Editor 2012.
- [22] Kearns, *Diffusion coefficient of hydrogen in alpha Zr, Zircaloy-2 and Zircaloy-4*. Journal of nuclear Materials, 1971. 43(1972): p. 330-338.
- [23] McMinn, A., Darby, E.C., Schofield, J.S., *The Terminal Solid Solubility of Hydrogen in Zirconium Alloys*. Zirconium in the Nuclear Industry: Twelfth International Symposium, 2000. ASTM STP 1354: p. 173-195.
- [24] Derek Gaston, J.H., *MOOSE Workshop*, 2012, Idaho National Laboratory: MIT.
- [25] Chris Newman, G.H., Derek Gaston, *Three dimensional coupled simulation of thermodynamics, heat and oxygen diffusion in UO<sub>2</sub> nuclear fuel rods*. Journal of nuclear Materials, 2009. 392: p. 6-15.



- [26] Zienkiewicz, O.C., R.L. Taylor, and J.Z. Zhu, *The finite element method: its basis and fundamentals* 2005.
- [27] Menibus, A.H.d., "Formation de blisters d'hydrures et effet sur la rupture de gaines en Zircaloy-4 en conditions d'accident d'injection de reactivite," Doctorat Thesis in Sciences et Genie des Materiaux, Ecole Nationale Supérieure des mines de Paris, 2012
- [28] Sugisaki, M., K. Hashizume, and Y. Hatano, *Estimation of hydrogen redistribution in zircaloy cladding of spent fuel under thermal conditions of dry storage and evaluation of its influence on mechanical properties of the cladding*, in *Effects of Radiation and Environmental Factors on the Durability of Materials in Spent Fuel Storage and Disposal*, , IAEA-TECDOC-1316, IAEA, Editor 2002, IAEA: Vienna, Austria. p. 63-78.
- [29] Morozumi, S., et al., *Effects of the alloying elements and cold work on the redistribution of hydrogen in Zirconium under a temperature gradient*. Journal of Nuclear Materials, 1969. 33: p. 261-270.
- [30] Hashizume, K., Hayakawa, M., Koganemaru, M., Sugisaki, M., *Temperature dependence of heat of transport of hydrogen in zirconium*. Defect and Diffusion Forum, 1993. 95-98: p. 323-328.
- [31] Markowitz, J., *The thermal diffusion of hydrogen in alpha-delta Zircaloy-2*. Transactions of the Metallurgical Society of AIME, 1961. 221(819-823).
- [32] Sawatzky, A. and E. Vogt, *Mathematics of the Thermal Diffusion of Hydrogen*. Transactions of the Metallurgical society of AIME, 1963. 227(4): p. 917-928.
- [33] Hong, H.S., S.J. Kim, and K.S. Lee, *Thermotransport of hydrogen in Zircaloy-4 and modified Zircaloy-4*. Journal of Nuclear Materials, 1998. 257: p. 15-20.
- [34] Kammenzind, B.F., *Hydrogen pickup and redistribution in alpha-annealed Zircaloy-4*. Zirconium in the Nuclear Industry: Eleventh International Symposium, ASTM STP 1295, 1996: p. 338-370.
- [35] Surface Igniter, LLC. Available <<http://www.surfaceigniter.com/>>
- [36] Kammenzind, B.F., et al. *Hydrogen Pickup and Redistribution in Alpha-Annealed Zr-4*. in *Zirconium in the Nuclear Industry: 11th International Symposium*. 1996.
- [37] Douglass, D.L., *The Metallurgy of Zirconium* 1971, Vienna: International Atomic Energy Agency Supplement.
- [38] *Analysis of Zirconium Alloys*, 1999, Luvak, Inc.: Boston, MA.
- [39] Zanellato, O., et al., *Synchrotron diffraction study of dissolution and precipitation kinetics of hydrides in Zircaloy-4*. Journal of Nuclear Materials, 2012. 420: p. 537-547.
- [40] Cullity, B.D., *Elements of X-ray Diffraction*. Second Edition ed 1978: Addison-Wesley Publishing Company, Inc.
- [41] *The Powder Diffraction File*, 2006, International Center for Diffraction Data.
- [42] U.S.DOE, *The Advanced Photon Source, A National Synchrotron Radiation Research Facility at Argonne National Laboratory*, 1999.
- [43] Haeffner, D.R., J.D. Almer, and U. Lienert, *The use of high energy X-rays from the Advanced Photon Source to study stresses in materials*. Materials Science and Engineering: A, 2005. 399(1-2): p. 120-127.

- [44] Larson, A.C. and R.B.V. Dreele, *General Structure Analysis System (GSAS)*, 2000, Los Alamos National Laboratory.
- [45] Colas, K., "Fundamental experiments on hydride reorientation in Zircaloy," PhD Thesis in Mechanical and Nuclear Engineering, Pennsylvania State University, 2012
- [46] Courty, Olivier. Hydrogen Distribution In Zircaloy Under A Temperature Gradient: Modeling, Simulation And Experiment. 2013. MSc thesis in Nuclear Engineering, The Pennsylvania State University.
- [47] Ian Davis, Olivier Courty, Maria Avramova, Arthur Motta, Kostadin Ivanov. NURETH-15 Conference Proceedings. High-Fidelity Multi-Physics Coupling for Prediction of Anisotropic Power and Temperature Distributions in Fuel Rod: Impact on Hydride Distribution. May 2013
- [48] Olivier Courty, Arthur Motta, Christopher Piotrowski. Measurement of the kinetics of precipitation in Zircaloy-4. Submitted to Journal of nuclear materials, October 2014.
- [49] Olivier Courty, Arthur Motta, Jason Hales, Modeling and simulation of hydrogen behavior in Zircaloy-4 fuel cladding, Journal of Nuclear Materials, 454 (2014) 311
- [50] Ian Davis, Olivier Courty, Maria Avramova, Kostadin Ivanov, Arthur Motta, "Simulation of the redistribution of hydrogen in a nuclear fuel cladding based on a coupling between neutronics, thermohydraulics and fuel performance code" Nuclear Technology, to be submitted, 2014.